Doctoral Thesis

Numerical models to describe fracture and plasticity in wood and their application to optimize laminated timber products

submitted in satisfaction of the requirements for the degree of
Doctor of Science in Civil Engineering
of the TU Wien, Faculty of Civil Engineering

Dissertation

Numerische Modelle für die Beschreibung von Bruch- und Plastizitätsversagen von Holz und deren Verwendung zur Optimierung von geschichteten Holzprodukten

ausgeführt zum Zwecke der Erlangung des akademischen Grades eines
Doktors der technischen Wissenschaften
eingereicht an der Technischen Universität Wien, Fakultät für Bauingenieurwesen

von

Dipl.-Ing. **Sebastian Pech**, BSc
Matr.Nr.: 1126795

Betreuer: Univ.Prof. Dipl.-Ing. Dr.techn. **Josef Füssl** &
             Dipl.-Ing. Dr.techn. **Markus Lukacevic**
             Institut für Mechanik der Werkstoffe und Strukturen
             Technische Universität Wien
             Karlsplatz 13/202, 1040 Wien, Österreich
Gutachter: Univ.Prof. Dipl.-Ing. Dr.techn. **Rudolf Heuer**
             Institut für Hochbau, Baudynamik und Gebäudetechnik
             Technische Universität Wien
             Karlsplatz 13/208, 1040 Wien, Österreich
Gutachter: Prof. **John A. Nairn**, PhD
             Department of Wood Science and Engineering
             Oregon State University
             112 Richardson Hall, Corvallis, OR 97331-5751, USA

Wien, im Mai 2022

Acknowledgements

Kurzfassung

Holz ist ein natürlich gewachsenes Material. Es ist inhomogen, zeigt ein orthotropes Verhalten im *clear-wood* Material und enthält Wuchsunregelmäßigkeiten und Äste, die zu erheblichen Abweichungen im Holzfaserverlauf führen. Plastizität und Bruch sind durch die Mikrostruktur stark richtungsabhängig und durch Mikrorisse und Effekte wie *fiber bridging* beeinflusst. Diese Mechanismen in einer nummerischen Simulation abzubilden ist anspruchsvoll. Daher beruhen derzeitige Bemessungsregeln in erster Linie auf empirischen Studien, die im Hinblick auf ihre mechanische Genauigkeit unzureichend sind. In dieser Arbeit werden Ansätze zur Modellierung des komplexen mechanischen Verhaltens von Holz vorgestellt und es wird gezeigt, wie eine fundierte mechanische Modellierung Optimierung von laminierten Holzprodukten erlaubt und zu ressourceneffizienteren Konstruktionen führt.

Üblicherweise werden Holzbretter nach visuellen Indikatoren wie Astmerkmalen oder Fehlern, und einfachen mechanischen Tests sortiert. Eine optimale Nutzung der Bretter z.B. in Brettschichtholzträgern wird erreicht, indem Bretter höherer Güteklassen in den äußeren, stark beanspruchten Schichten angeordnet werden. Dies ist eine einfache und zeitsparende Lösung. Eine optimale Nutzung ist aber nicht möglich, da bei der Sortierung die Morphologie und die mechanischen Eigenschaften der Bretter stark homogenisiert werden. Umgehen der Sortierung ist durch mechanisch fundierte Homogenisierungsstrategien möglich. Mechanische Simulationen ermöglichen die Beurteilung der Auswirkung von Ästen und Fehlern, im Hinblick auf den tatsächlichen Spannungszustand eines Bretts in einem Brettschichtholzträger. In Verbindung mit globalen Optimierungstechniken können Fragen wie „Welche Anordnung von Holzbrettern in Brettschichtholzträgern minimiert die maximale Durchbiegung des schlechtesten Trägers?" beantwortet werden.

Um die Bedeutung von Ästen und Fehlstellen richtig einschätzen zu können, müssen Plastizitätseffekte und Bruchvorgänge berücksichtigt werden. Plastizität in Holz wurde bereits erfolgreich mit mehrflächigen Versagenskriterien beschrieben. Auf Grundlage zahlreicher Simulationen verschiedener Strukturen zeigt diese Arbeit, dass der üblicherweise verwendete Algorithmus, um Spannungszuständen in den gültigen Bereich zurückzubringen, unter Konvergenzproblemen leidet. Anhand von drei ausgewählten elastoplastischen Dehnungszuständen, werden die Probleme analysiert und Verbesserungen vorgeschlagen. Das verbesserte Modell ist robust und kann für eine Vielzahl von Problemen verwendet werden. Der Anstieg der gesamten Berechnungszeit ist gering, da größere Lastinkremente möglich sind.

Neben der Plastizität ist das Abbilden von Bruchversagen essenziell. Die Simulation von Bruchvorgängen ist eine schwierige Aufgabe und das ansteigende wissenschaftliche Interesse in dem Gebiet bestärkt die Wichtigkeit. Ein Simulationsframework für Holz muss mit den oben genannten mechanischen Eigenschaften umgehen können, Lösungen in einer vertretbaren Rechenzeit finden und netzunabhängige Ergebnisse liefern. Bei Holz ist insbesondere die Modellierung komplexer Rissverläufe in der Nähe von Ästen eine Herausforderung. Daher wird in dieser Arbeit die *phase field method for fracture* angewandt, die Rissverzweigung, -vereinigung und -abknickung in dreidimensionalen Modellen unterstützt. Vorgestellt wird ein *phase field* Modell für die makroskopische Skala für orthotrope, nicht spröde Materialien mit bevorzugten Bruchebenen und mehreren Versagensmechanismen. Dieses Modell basiert auf der *unified phase field* Theorie und verwendet einen hybriden Ansatz mit einer traktionsfreien Rissrandbedingung zur Modellierung diffuser Risse. Das Modell kann das Zick-Zack-Bruchmuster reproduzieren, das in Holz aufgrund des Einflusses der Interfaceflächen zwischen den Holzfasern und der Holzmatrix auftritt und die signifikanten Änderungen der Rissorientierung in der Nähe von Ästen modellieren. Darüber hinaus stimmen sowohl die Reaktionskurve als auch die Risstopologie der simulierten Modelle mit den Ergebnissen experimenteller Untersuchungen überein. Das Modell kann auch die Rissentwicklung für komplexe dreidimensionale Modelle abbilden. Dadurch kann es in Zukunft für die Ableitung von Homogenisierungsmodellen, die auch Bruchprozesse berücksichtigen, verwendet werden.

Abstract

Wood is a naturally grown material. It is inhomogeneous, shows an orthotropic behavior of the clear-wood material and contains growth irregularities and knots, which lead to significant deviations in the wood fiber courses. Due to its microstructure, plasticity and fracture are highly direction-dependent and influenced by micro-cracking and fiber bridging phenomena. Describing all of these effects in numerical models is a major challenge. Therefore, current design rules are primarily based on empirical studies, which are insufficient in terms of proper mechanical description accuracy. Thus, this work presents approaches for modeling the complex mechanical behavior of wood and shows how proper mechanical modeling could improve laminated timber products to lead to more resource-efficient designs.

Commonly, wooden boards are graded according to visual indicators like knot characteristics or defects and simple mechanical tests. Optimal usage of the graded boards e.g., in glued laminated timber beams is achieved by placing boards of higher grades in the outer, highly stressed layers. While this is a simple and time-efficient solution, it is impossible to achieve optimal usage, as, during wood grading, the board's morphology and mechanical properties are rigorously homogenized. Skipping the grading process using homogenization strategies based on mechanical modeling and simulations allows assessing the influence of knots and defects based on expected stress states a board is subjected to in a glued laminated timber beam. Mechanical simulations, combined with global optimization techniques, can be used to answer questions like "Which arrangement of a sample of wooden boards in glued laminated timber beams minimizes the maximum deflection of the weakest beam?".

For a proper assessment of the significance of knots and defects, plasticity effects and fracture processes must be considered. For plasticity, multi-surface failure criteria have been successfully used to describe wood. Based on numerous simulations of different structural systems, this work shows that the commonly used algorithm for returning stress states to the feasible domain suffers from convergence issues. On three selected stress and strain states, the issues are analyzed, and improvements are proposed. The advanced model is more robust than the original one and can be used for a wide range of problems. The increase in the overall computational time is minor as the improved model allows for larger load increments.

Besides plasticity, there is fracture. Simulating fracture processes is generally a challenging task, and increasing scientific activity in this area underlines the importance. A viable simulation framework for wood needs to be able to handle the aforementioned mechanical characteristics, find solutions in a feasible computation time and must produce mesh-independent results. In wood, particularly the complex crack paths in the vicinity of knots pose a challenge. Therefore, this work applies the phase field method for fracture as it implicitly supports crack branching, merging and kinking in three-dimensional models. A multi-phase field model for the macroscopic scale of orthotropic, non-brittle materials with favorable fracture planes and multiple failure mechanisms is proposed. It is based on the unified phase field theory and utilizes a hybrid approach with a traction-free crack boundary condition for geometrically modeling diffusive cracks. The model can reproduce the commonly found zig-zag fracture pattern which occurs in wood due to the influence of the interface between the wood fibers and the wood matrix and can model the significant changes in the crack orientation close to knots. Furthermore, both the response graph and the crack topology of the tested wood specimen match the results of experimental studies. The model can also depict the crack evolution of complex three-dimensional specimens, allowing future usage for deriving homogenization models for wooden boards that consider fracture processes.

Contents

Introduction

Motivation and Outline

Wood is one of the most traditional building materials and has been used for construction for centuries. Despite modern building materials, wood can regain market shares in the construction industry and has been booming in recent years. One of the main factors for this uprise is that wood, compared to other building materials like steel or concrete, does not contribute to the increase in carbon dioxide emissions. Considering the whole lifecycle, from the tree to the possible recycling of timber construction elements, wood removes more carbon dioxide from our atmosphere than it adds. Thus, usage as a building material provides an opportunity to tackle the climate crisis.

Apart from these beneficial factors, it is also an excellent building material if used appropriately. During growth, wood is optimized to withstand the harsh conditions a tree is exposed to. This leads to a micro- and macrostructure, which is lightweight and has excellent load-bearing capacity. Projects like the *HoHo* in Vienna, a 24 storage, 84 m high, timber and concrete hybrid high-rise building, highlight how well timber constructions can perform. However, compared to other common building materials, the knowledge about the complex mechanical behavior of wood is limited. In order to be competitive with materials like steel and concrete, this knowledge is definitely necessary. Otherwise, a resource and economically efficient usage is not possible.

Wood is an inhomogeneous material showing an orthotropic behavior of the clear-wood material, growth irregularities and knots, which result in significant fiber deviations. Plasticity and fracture are highly direction-dependent and influenced by many phenomena like micro-cracking or fiber bridging. As simulating all those processes is a challenging task, current design rules are mainly based on empirical studies, which are insufficient in terms of proper mechanical description accuracy. Therefore, this work presents approaches for properly describing the complex mechanical behavior of wood through numerical simulations and optimizing the steps required to ensure its resources efficient usage. Figure 1 depicts the overall concept, which is elaborated in the following sections.

(a) Laser scanning

(b) Reconstruction of knot morphology and fiber deviations

(c) Finite element model (**Publications 2–4**)

(d) Surrogate model or effective material properties (**Publication 1**)

(e) Application to wood and wood products (**Publication 1**)
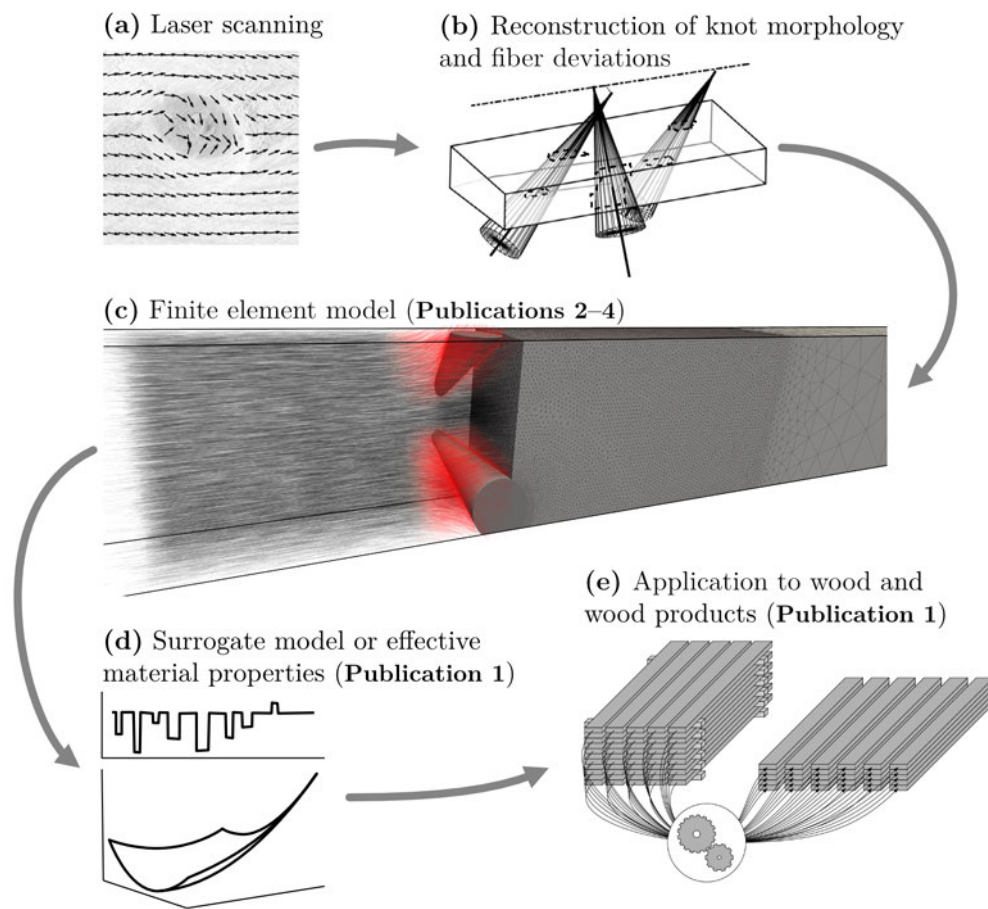
Fig. 1: Conceptional overview of the approaches taken in this thesis for performing numerical simulations and optimization of wood and wood products

Material Model for Wood

When performing numerical simulation, it is necessary to balance the level of considered details and the model's overall size. While computational performance has vastly increased in recent decades, simulating e.g., a large GLT beam by modeling the microstructure of wood is still not feasible. Therefore, homogenization steps are performed, which bring small-scale properties to larger scales.

Length scales of wood

Figure 2 shows the length scales considered for modeling the mechanical behavior of wood. The following is a summary of Hofstetter et al. [62], Lukacevic et al. [83], and Smith et al. [127]. The stem cross-section of wood shows alternating early- and latewood layers arranged in concentric, so-called annual rings. The typical size of an annual ring is 2 mm to 4 mm. Wood cells (tracheids) are hollow tubes oriented in the stem direction with diameters of 20 μm to 500 μm and lengths of 2 mm to 10 mm. They form both early- and latewood. The cell wall consists of multiple layers which differ in thickness, dosage, and arrangement of their constituents. It is made from cellulose microfibrils with diameters of about 50 nm to 200 nm which vary in orientation. A non-cellulosic matrix of hemicelluloses, lignin and inorganic compounds embeds the fibers. The S3 layer forms the inside of the cell wall. Adjacent is the S2 layer, which makes up about 80 % to 90 % of the volume of the entire cell wall. This layer is mainly responsible for the structural stiffness and strength in the cells' longitudinal direction and increases in thickness from early- to latewood. The

outer cell wall consists of the S1 layer and the primary (P) cell wall, which is formed first in the cell growth process. The middle lamella (ML) connects the wood cells.
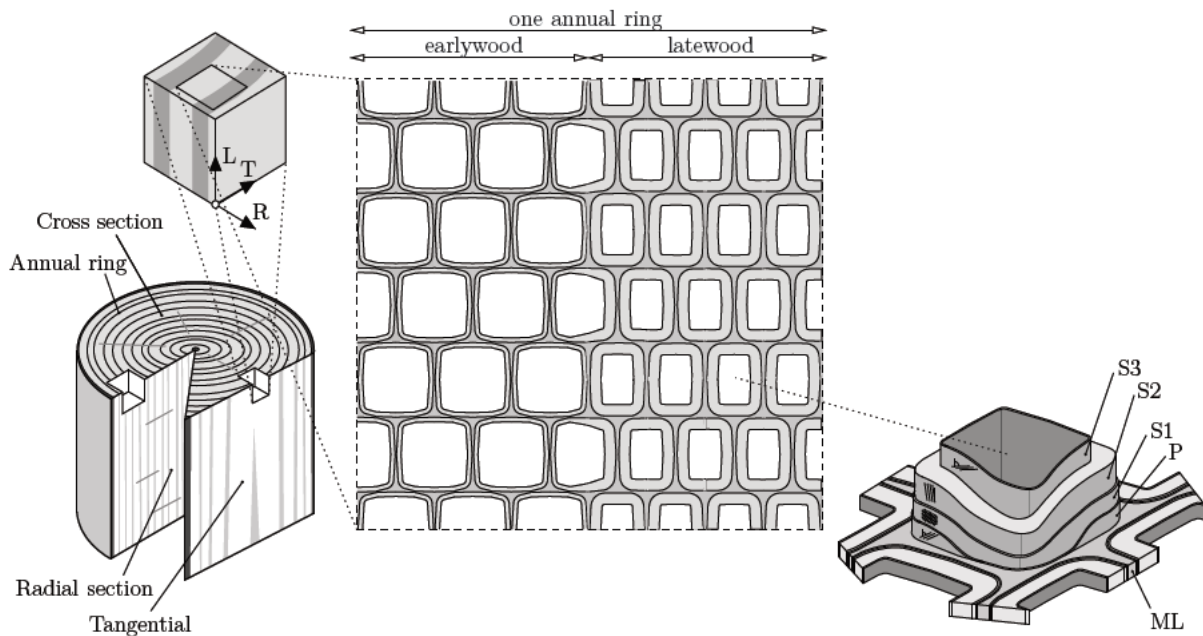
Fig. 2: Section of a log with the coordinate system, the honeycomb-like structure and a schematic illustration of the layered cell wall [83].

Linear elastic properties

In this work, wood is modeled on the macroscopic level by considering an orthotropic behavior influenced by the underlying microstructure. Wood fibers produced simultaneously during tree growth are situated on a so-called growth surface. Those surfaces are located concentrically around the pith and give structure to the material. Thus, a cylindrical coordinate system is used to describe the local material directions, where the longitudinal direction (L) points into the fiber direction, the radial direction (R) is normal to the growth surface and the tangential direction (T) is the vector perpendicular to both L and R.

The mechanical properties of wood are usually specified relative to the fiber coordinate systems. Determination of linear elastic properties can be approached in various ways depending on available information. By using a micromechanical model, the stiffness tensor is computed considering nanoscale constituents and microscale properties, such as clear-wood density, moisture content, microfibril angle and volume fractions of hemicelluloses, cellulose, lignin and water [62, 63, 82]. This allows adjustment of the constitutive behavior depending on the wood species and water saturation. Elastic properties obtained from a micromechanical model or nominal values from the literature can further be improved by assisting experimental studies. Measuring the axial resonance frequency of e.g., a single wooden board employing dynamic excitation allows scaling the elastic properties in a model such that the calculated resonance frequencies match the experimentally obtained ones [65]. Similarly, such a tuning process can be done by matching a computed load-deflection graph to a measured one.

A micromechanical model can also be used to estimate the stiffness of the knots. Knots have a higher density and microfibril angle than clear-wood. However, Lukacevic et al. [84] discussed that knots almost always show cracks perpendicular to the grain direction, which strongly influences the elastic behavior. Hence, the stiffness tends to be overestimated by the micromechanical model and considering half of the clear-wood stiffness for knots gives results in good agreement with experimental observations.

Reconstruction of fiber courses

For precise simulation of wooden boards, knowledge of the spatial variation of fiber directions, i.e., the LRT-coordinate systems at every position within the board, is necessary. This is done in a two-step manner: First, the board's geometrical features, i.e., the pith location and knots, are identified. Subsequently, spatial fiber courses can be determined based on the obtained features. Kandler et al. [69] proposed an algorithmic approach for reconstruction of the pith location and knot geometry of a wooden board based on laser scanning information and photographs of the board. For wooden boards, fiber orientations can be obtained by laser scanning the board's surfaces (Figure 1 (a)). The phenomenon enabling this method is the so-called tracheid effect, which describes light propagation on a wooden surface. Major material axis are identified by monitoring the deformation of the laser dot, which spreads further in directions parallel to the fiber [99, 156]. Based on those fiber angle measurements, out-of-plane fiber angles are determined, allowing the identification of knot areas. The pith location is reconstructed by fitting concentric circles to annual rings at both board ends. Subsequently, knots, represented as rotationally symmetrical cones, are placed inside the board such that they match identified knot areas on different board faces when originating from the found pith location (Figure 1 (b)).

The spatial information about the fiber courses is deduced from the geometrically reconstructed board by picturing the wood fibers as streamlines flowing around an obstacle (the knot). The fiber direction in the LT-plane can be computed using the so-called *Rankine* oval, which describes the fluid flow around an elliptical object [84], allowing the definition of the LRT-coordinate system at each location within the wooden board. Figure 1 (c) shows the precomputed spatial fiber courses (L-vector) in the left half of the beam. The stronger the fiber deviates from the beam's axis, the redder it appears. This fluid flow-based approach is used in Publication 3 to compute the fiber courses in the wooden board with a single knot.

Bending stiffness profiles

Similar to a micromechanical model, bending stiffness profiles homogenize information about the influence of spatial fiber courses and knot geometries on the board's elastic stiffness. A single value at each position along the longitudinal axis of a wooden board characterizes the effects of the underlying structure. This step is the transition from Figure 1 (c) to (d) and enables the simulation of large-scale structures. For computing a profile of a single board, the approach outlined in Lukacevic et al. [84] is followed. Starting from the detailed spatial fiber deviation model, the longitudinal strains on each of the two wide surfaces of a board are computed in a linear finite element simulation. Next, a less complex beam model is tuned by least squares regression. The linear distribution of longitudinal strains of the beam model approximates the longitudinal strains of the finite element model. For a given load and board dimensions, this allows the determination of the bending modulus of elasticity along the beam's axis. The final stiffness profile is obtained by computing a moving average with the desired resolution (window size) along the beam. This approach significantly reduces the computation effort as now, instead of a computationally costly, detailed simulation, a simple beam model can be used. However, this model is unsuitable for precise stress and strain fields assessment, as this information is no longer contained.

Publication 1 utilizes bending stiffness profiles for modeling the constitutive behavior of GLT beams. Herein, each lamella is described by a stiffness profile. Using stiffness profiles instead of single, homogenized stiffness values from strength grading, allows for optimizing GLT beams by rearranging low stiffness regions to areas of the beam with lesser influence on the load-carrying capacity.

Failure surfaces

An approach for homogenizing plasticity and fracture failure modes on the wood cell level is proposed in Lukacevic et al. [83]. The wood cell structure essentially defines the occurrence of plastic effects and the development of failure modes. Thus, a wood cell pattern (honeycomb structure in Figure 2) is modeled

employing the unit cell method, where periodic boundary conditions are applied to a representative part of a repeating pattern. The multiple cell wall layers are homogenized into a single cell wall material with the middle lamella separately accounted for. The resulting unit cells for early- and latewood are subjected to different deformation states from a six-dimensional search space comprising three normal and three shear deformation components. Analyzing the occurring failure stresses and mechanisms allows fitting multiple Tsai-Wu failure surfaces [133] in stress space for each failure mechanism and further identification of crack face orientations for the annual ring scale. The identified multi-surface failure criterion can be applied by discretely modeling alternating layers of homogenized early- and latewood.

Based on the derived Tsai-Wu failure surfaces for early- and latewood, the next homogenization step from the annual year ring scale to homogenized clear-wood can be done similarly. In Lukacevic et al. [85], first, a unit cell comprising multiple alternating layers of late- and earlywood is modeled. Subsequently, this unit cell is subjected to various deformation states resulting in tensile, compressive and shear load combinations. Analyzing the resulting failure stresses and modes leads to a new multi-surface Tsai-Wu criterion for the clear-wood level, applicable to larger-scale structures, where modeling on the annual year ring level is not feasible.

The found failure surfaces are used in Publication 2, where a commonly used multi-surface return-mapping algorithm for ideal plasticity is discussed. The work shows that the applied return-mapping approach fails for some stress configurations. Introducing new solver techniques makes finding feasible stress states possible.

Fracture mechanics models using the phase field method for fracture

Precise failure determination of engineering structures and components is crucial for their application and optimization. There, fracture is the most common cause of failure. With the broad establishment of the finite element method, new methods for simulating fracture emerged. Modeling follows two approaches: Discontinuous crack models that consider displacement jumps explicitly and softening behavior through traction-separation laws and continuous crack models where displacement jumps are smeared over damaged elements and softening is considered with a stress-strain law [25]. For both, the main challenge is providing mesh-independent numerical results. In the field of continuous crack models, the phase field method for fracture proves to be applicable to a wide variety of problems. Mesh-independence, a sound physical foundation based on *Griffiths'* theory of fracture, easy implementation into standard finite element tools, consideration of the material strength and toughness through the unified phase field theory and support for complex fracture phenomena like branching and merging are key advantages of the theory. However, the computational cost is very high due to the small mesh size required. Publication 3 gives a detailed introduction to the general method and its extension to model cohesive behavior with the unified phase field theory. For wood fracture, especially the capability to model very complex crack patterns in a three-dimensional setting is essential.

Optimization strategies and surrogate models

Optimization is a broad term, and mathematically, this entire manuscript deals with minimization techniques. Gradient-based optimization is used for deriving a surrogate model in Publication 1, solving the return-mapping problem in Publication 2 and finding solutions to the bound-constrained phase field problem in Publications 3 and 4. Metaheuristic schemes are applied for global optimization of glued laminated timber (GLT) beams in Publication 1. In an engineering application-centered sense, optimization is vital for improving structures and components regarding a multitude of goals like reducing resource usage or improving the structural performance of a component. Resource efficiency allows utilizing the

environmentally friendly nature of wood and enables competitiveness in the construction industry. As shown in Figure 1, an intermediate step is required from the detailed finite element model to the actual application to large-scale structures. So optimization links Publications 2 to 4 with Publication 1.

Research Objectives and Outline of the Thesis

Publication 1 deals with the global optimization of GLT beams. The problem statement at hand is as follows: "Given a set of wooden boards with varying longitudinal stiffness, how can those boards be optimally distributed and arranged over a target amount of beams?". Initially, this very general problem description is analyzed in detail and narrowed to allow a proper, exact formulation of the search space and the objective function for this combinatorial optimization task. Additionally, the steps involved in evaluating the objective function, mainly performing a two-dimensional finite element simulation of the GTL beam, are closely investigated. The huge size of the search space, together with a computationally costly finite element simulation, lead to the conclusion that a metamodel (or surrogate) is required to simplify the objective function and that metaheuristic algorithms, like genetic algorithms, local search or iterated local search, are needed to find an optimum. Therefore, given a wide range of possible choices of numerical methods and parameters, a study is conducted, resulting in recommendations for algorithms depending on the given circumstances. The capabilities of the proposed procedures were tested against conventional methods of assembling inhomogeneous GLT beams.

Publication 2 concerns the implementation and improvement of a multisurface return-mapping algorithm for modeling plastic failure of wooden structures and components. The work opens with a review of commonly applied methods and shows flaws and various addition to improving robustness. Subsequently, a multistage approach is proposed, where each stage increases the likelihood of finding feasible stress states within the bounds of the multisurface criterion. This new algorithmic scheme is validated using multiple elasto-plastic strain states, for which previously no solutions could be found. To further show how the proposed method influences finding feasible stress states, the effects of the multistage procedure are visualized for each stage of the approach, highlighting the differences to conventional methods.

Publication 3 is dedicated to fracture mechanics simulations of wood by using the phase field method for fracture. As the originally proposed phase field method does not allow for orthotropic, quasi-brittle materials with favorable fracture planes, the work investigates possible changes and improvements to this formulation to enable the simulation of wood. Initially, the complex mechanical processes involved in wood fracture are discussed, partly motivating the choice of the phase field method for fracture, namely that cracks of arbitrary complexity can be modeled. With the recently active research on the phase field method for fracture, a study has been conducted concerning various alterations, which are reviewed and evaluated on how well they can be used to simulate wood fracture. Subsequently, a novel hybrid approach for considering crack driving forces independent of the degradation of the constitutive behavior is proposed, which allows modeling orthotropic, quasi-brittle materials with favorable fracture planes. The algorithm is qualitatively assessed on a simple single edge notched plate with varying wood fiber orientations. Obtained cracks are compared to commonly found patterns in wood tests, showing that the hybrid approach is superior to the variationally coupled one. Finally, a more complex example of a wooden board with a single knot and spatially varying wood fiber orientations is studied.

Publication 4 deals with the validation of the previously developed hybrid phase field model for orthotropic, quasi-brittle materials with favorable fracture planes, using results from four different

experimental studies from literature. Due to the larger model dimensions, an additional improvement of the initially proposed solver is discussed, which allows appropriately adapting the size of the load increment in regions of strong nonlinearities. First, the primary unknown quantity, a scale factor accounting for favorable fracture directions, is determined by simulating an end notched beam, where the experimentally found crack strongly depends on the micro- and macrostructure of wood. Subsequently, the tensile strength and the fracture energy release rate are obtained for all studied specimens. The model's capabilities are assessed on how well the load-deflection response graph and the ultimate crack pattern can be reproduced.

Contributions by the author

This thesis consists of four publications in peer-reviewed scientific journals. Publications 3 and 4 are currently under review. The author's contributions to the publications are as follows:

- **Publication 1**, *Metamodel assisted optimization of glued laminated timber beams by using meta-heuristic algorithms*: The author developed the proposed algorithms, performed all simulations and prepared most of the manuscript.

- **Publication 2**, *A robust multisurface return-mapping algorithm and its implementation in Abaqus*: The author greatly contributed to the development of the proposed algorithm, performed all simulations and prepared most of the manuscript.

- **Publication 3**, *A hybrid multi-phase field model to describe cohesive failure in orthotropic materials, assessed by modeling failure mechanisms in wood*: The author developed the proposed algorithm, performed all simulations and prepared most of the manuscript.

- **Publication 4**, *Validation of a hybrid multi-phase field model for cohesive failure in orthotropic materials on experimental studies*: The author developed the proposed algorithm, performed all simulations and prepared most of the manuscript.

Publication 1

Metamodel assisted optimization of glued laminated timber beams by using metaheuristic algorithms

Abstract

An efficient use of the raw material in GLT beams is commonly achieved by inserting lamellas of lower quality in less stressed areas, usually in the middle of a beam. But, this rather simple method leaves room for improvement. In particular, the morphology of a board and its location in the beam setup is significant, since only this information and the actual loading situation allows a proper evaluation of weaknesses. Therefore, a new optimization method was developed, able to take mechanical property distributions as well as the occurring stress states within each wooden board into account.

Subsequent to an automatic knot reconstruction and determination of effective local stiffness distributions of all boards, the beams are analyzed using a finite element (FE) model. This information is further exploited to find optimal beam setups out of a sample of boards. However, as the complexity of this optimization task quickly increases with the number of boards, metaheuristic optimization algorithms were developed. Additionally, the evaluation of the computationally expensive FE model is bypassed by a metamodel, capable of approximating the desired performance parameter of any beam. Comparing the various optimization approaches to common GLT beam production methods, maximum deflection can be reduced by 15 % to 20 %.

1.1 Introduction

Throughout the previous years, wood consequently gained importance in fields of civil engineering where usually mainly steel and concrete constructions were used. Especially buildings like the *HoHo* in Vienna, a 24 storage wooden high-rise building, demonstrate the capabilities of wood as a construction material. Besides its remarkable qualities in this concern, wood is a naturally grown resource and, thus, contributes to lowering carbon dioxide (CO_2) emissions in comparison to steel- or concrete production. Therefore, under the assumption of sustainable forestry, focusing on using wood as a building material can help to slow down global warming.

However, wood exhibits a quite complex mechanical behavior, which is difficult to constitute in a mechanical model. Therefore, existing design rules are often based on empirical findings, which, especially in terms of mechanical description accuracy, are unsatisfactory. A common approach for optimizing the load-bearing behavior of GLT beams, with respect to an efficient use of the raw material, is producing combined GLT beams [1]. Based on a previously performed visual grading [37] and a strength classification [2], stronger boards are used for the highly stressed outer layers of the GLT beam, whereas weaker boards are used to fill the less stressed inner layers. This strategy, however, leaves room for improvement and particularly the following limitations have to be considered:

- Currently, the classification methodology considers the spatial variability of mechanical properties within wooden boards to a limited degree. However, knots and the resulting fiber deviations lead to strong localized effects and spatial fluctuations of stiffness and strength.

- By using beam theory and assuming a homogeneous distribution of mechanical properties along wooden boards, the actual structural behavior of the beam cannot be represented very accurately.

- The strength class is determined without considering the actual resulting stresses on the lamella in the final structure. Thus, certain classification criteria might lead to a reduction of the strength class of a lamella, although their impact within the final beam is neglectable.

Therefore, the grading process and the design process of GLT beams should be combined in order to better utilize timber boards.

The method proposed in this paper utilizes the data acquired during the machine strength grading process to model the mechanical behavior of each timber board. Thus, the mechanical properties of each board are determined individually and not defined through a given class, hence spatial stiffness fluctuations are considered. Moreover, a 2D FE computation is performed to determine strain and stress of each individual wooden board within the GLT beam assembly. This method provides a basis for a more elaborate optimization of the load-bearing behavior of GLT beams. Figure 1.1 depicts the process from unordered stacked wooden boards to optimally constructed GLT beams.

As will be outlined in Section 1.2.3 this optimization task is quite difficult due to the vast amount of combinations of wooden boards and the computationally costly FE model. Recent research on problems of similar complexity [73, 91, 141, 154] showed that a combination of a dimension reduction of the original model and the application of metaheuristic algorithms (MAs) yields viable solutions for such optimization task. Especially Coelho et al. [28] address the issue of coping with the high computational effort involved in an FE calculation through substitution with a regression model, also referred to as a metamodel.

Our previous work's focus was on developing material models for wood and wooden structures. In this paper, the focus is laid on using the results of this recent research in a practical example. Emphasis are on the formulation of the optimization problem and the implementation and assessment of the applied optimization methods. Finally, variations in the problem definition are discussed and the actual improvement compared to commonly used methods for the construction of GLT beams is determined.
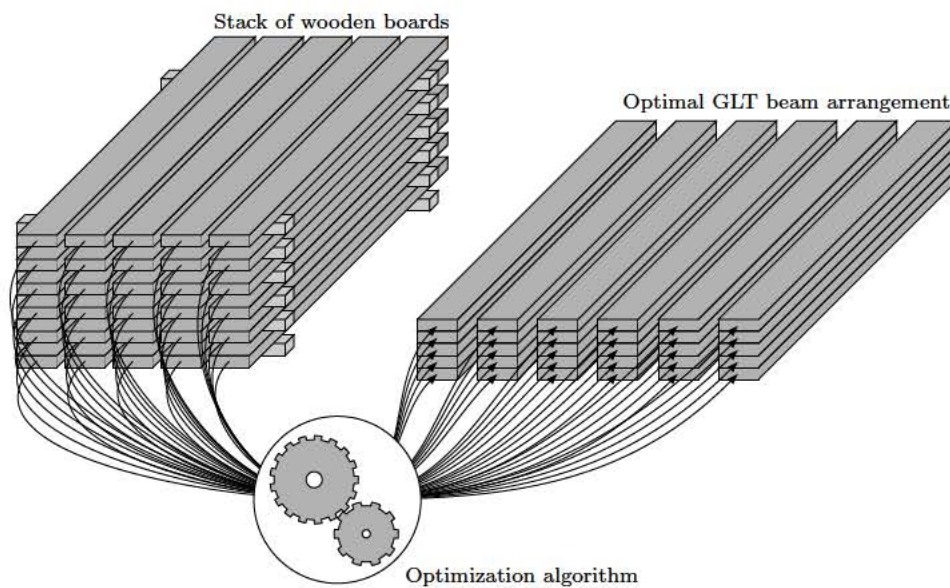
Fig. 1.1: Problem illustration from an unordered stack of wooden boards to optimally assembled beams. Finding an optimization algorithm to do this represents the general objective of this paper.

1.1.1 Material model for timber boards

For a sound mechanical model of GLT, the mechanical behavior of the "basic components", the individual timber boards, has to be determined. Numerous approaches incorporate extensive experimental investigations [41, 46] to predict the mechanical properties of timber boards in GLT beams based on morphological parameters, so-called indicating properties, such as the visible knot area. In recent years, however, numerical approaches became more and more popular for predicting the effective mechanical properties of timber boards [55, 59, 82]. These approaches require detailed knowledge of the knot morphology to identify the stiffness properties of individual timber boards.

The discussed data acquisition approach relies on laser scan data, which is obtained during the grading process of individual wooden boards. The underlying utilized effect is the so-called tracheid-effect, which describes the light propagation on a wooden surface. Due to the orthotropic fiber structure of wood, a concentrated light source, e.g. a laser beam, spreads differently parallel to the fiber than perpendicular [99, 156]. Thus, a laser dot deforms to an elliptical spot and reveals the major material axis.

Based on the measured fiber angles, two different approaches are pursued at IMWS[1] to obtain the localized stiffness tensors:

- Directly using the wood fiber angles [68], which is similar to the approaches by Oscarsson et al. [102], Petersson [108] and Olsson et al. [101], and

- reconstructing the knot morphology to perform a 3D linear elastic FE analysis [69, 70].

The direct procedure presented in [68], where the wood fiber angles are directly used to obtain longitudinal stiffness distributions by transforming the clear wood stiffness tensor, additionally uses an empirical model to determine the dive-angle [68, 100, 125]. The stiffness tensor is obtained in each measurement point from a micromechanical model based on a multi-scale homogenization procedure [62]. Homogenizing the values over each cross section results in a so-called stiffness profile for each board, describing the variation of the local modulus of elasticity E in the longitudinal direction x, hence $E \equiv E(x)$. By using these

---

[1]Institute for Mechanics of Materials and Structures, TU Wien

stiffness profiles in combination with a linear 2D FE model, an accurate mechanical model for predicting the effective stiffness of GLT beams was developed by Kandler et al. [68]. For this paper, stiffness profiles based on the second method are employed, as this method gives more accurate results through considering 3D fiber orientations.

1.2 Methods

In the following, the discussed calculation and optimization approaches are verified and supported by the practical example shown in Figure 1.2. Thereby, the total number of lamellas n_l, the number of beams n_b and the number of lamellas per beam $n_{b,l}$ are set to $n_l = 50$, $n_b = 5$ and $n_{b,l} = 10$. The lamella data used in this test sample comprises the lamellas 59 to 109 (except lamella 71 due to missing data in $E(x)$) of the grading class T22 (LS22), from the experiments in [121]. The dimensions and loads according to Figure 1.2 are $a_1 = a_2 = 1.38$ m, $a_3 = 0.63$ m and $F = 5.0$ kN. The lamellas are assumed to have equal cross sectional dimensions of $h_l = 0.033$ m in height and $w = 0.09$ m in width.
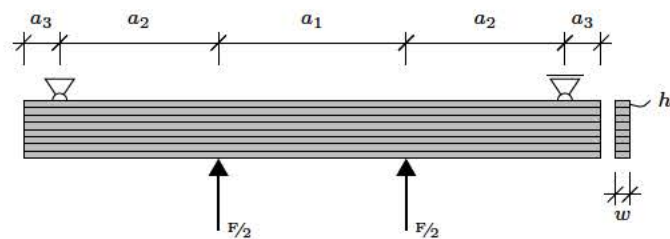
Fig. 1.2: Definition of dimensions for the test setup considered.

1.2.1 Aim of the optimization

As indicated in Figure 1.1, the problems investigated throughout this paper are of combinatorial nature. The goal is to improve the structural behavior of a set of beams, further referred to as beam setup, only by means of reordering the lamellas within the beams.

In this context, numerous different optimization tasks for GLT beams can be formulated:

- Find the optimal arrangement of n_l lamellas within n_b beams, where every beam consists of $n_{b,l}$ lamellas and $n_l > n_b n_{b,l}$.

- Find the optimal arrangement of n_l lamellas within n_b beams, where every beam consists of $n_{b,l}$ lamellas and $n_l = n_b n_{b,l}$.

- Find the optimal arrangement of n_l lamellas within one beam.

In this context, optimal arrangement means that the deflection of a beam is reduced to a minimum. This allows a specification of the optimization for a single beam, namely to minimize the deflection of the given beam. However, optimizing a beam setup is not as self-evident. Mainly two approaches seem to be meaningful:

- Reducing the mean deflection or

- reducing the maximum deflection

of the entire beam setup.

For some cases it can be useful to optimize the mean deflection. However, as those solutions consist of superior beams compensating for inferior ones, this method cannot be applied when this compensation is not granted within an actual construction the beams are used in. Therefore, in this paper it is assumed that the beams will be used separately and the main objective is to use the given timber boards as optimal as possible, under the given restriction of a targeted beam setup.

1.2.2 Mathematical formulation

Based on the problem description given in Section 1.2.1, independent of the optimization algorithm, a mathematical formulation of the stated problem can be given as follows: Let $\pi : L \to L$ be a permutation of the set of lamellas L and $g : l \mapsto l^*$ be a function which defines the orientation of a lamella l. Then $\pi^* = g \circ \pi$ returns a permutation of L with explicitly defined orientations. Let Φ be a map $\Phi : \pi^* \to B$ which maps the lamella permutation from lamella space into beam space B. Find a π^* which minimizes the objective function f.

Throughout this paper f is assumed to perform operations based on the function $q_{\max}$ which calculates the maximum deflection of a given beam b_i. As stated the objective of this combinatorial optimization (CO) problem is to generate a beam setup, where the value of $q_{\max}$ is as small as possible for every beam b_i contained in the solution. Therefore, f can be specialized for $q_{\max}$ as

$$f(\pi^*) = \max \left\{ q_{\max}(b_i) | b_i \in \Phi(\pi^*) \right\}. \tag{1.1}$$

As will be discussed in subsequent sections, a vector or list is suitable for representing a lamella order for a beam setup. The vector describing the lamella arrangement, with prescribed orientations, for a beam b_i will further be denoted by L_i^*. Thus Φ can be expressed in terms of L_i^* as

$$\Phi(\pi^*) = \left\{ L_i^* | \ i \in \{1, \ldots, n_b\} \right\}. \tag{1.2}$$

1.2.3 Analysis of the problem's complexity

1.2.3.1 Complexity of the combinatorial optimization task

Considering the most general case for the problem described in Section 1.2.1, where $n_l \geq n_b \, n_{b,l}$, the number of possible combinations for placing $n_b \, n_{b,l}$ lamellas out of n_l lamellas in n_b beams, considering a inhomogeneous stiffness distribution in longitudinal direction, as proposed in Section 1.1.1, is defined as

$$\frac{2^{n_b \, n_{b,l}} \, n_l!}{n_b! \, (n_l - n_b \, n_{b,l})!}. \tag{1.3}$$

For the example stated in Section 1.2.1 the number of distinct combinations is $\approx 2.8536 \times 10^{77}$. For a rough estimate of the computation time it is reasonable to consider the evaluation of the objective function only. The number of different beams contained in the search space of the optimization problem is given by:

$$\frac{2^{n_{b,l}} n_l!}{((n_b - 1) \, n_{b,l})!} \tag{1.4}$$

For the stated example this results in $\approx 3.817 \times 10^{19}$ different beams. Referring to the benchmark tests for the FE model described in Section 1.2.3.3, the average evaluation time of one beam is $292.3 \, \mathrm{ms}$. Therefore, the computation time for evaluating all combinations would be about 3.54×10^{11} years. This makes it practically impossible to determine the optimal result based on pure enumerative algorithms,

which requires the usage of optimization techniques able to deliver near optimal results without analyzing the entire search space.

1.2.3.2 Solvability by means of deterministic algorithms

In order to gain a general insight into the optimization task, a problem, based on the practical example, with reduced complexity is investigated. A possible approach towards reducing the complexity is neglecting the variability of the longitudinal stiffness profile $E(x)$ and instead considering each lamella with a constant stiffness $E(x) = E$. For this simplified case, maximizing the bending stiffness equals minimizing the maximum displacement. Furthermore, as $E_i(x) = E_i$, the orientation of the lamellas becomes irrelevant, hence $\pi^* \equiv \pi$ and $L_i \equiv L_i^*$. The bending stiffness of a single beam is defined as

$$EI_b(b_i) = \sum_{l \in L_i \equiv b_i} E_l\, I_l + E_l\, A_l\, z_{l,i}^2, \tag{1.5}$$

where A_l denotes the area of the cross section, I_l the second moment of area of the cross section and $z_{l,i}$ the distance of lamella l to the center of mass of beam b_i. In the present example, both A_l and I_l are not only constant within each lamella, but equal for all lamellas, i.e. $A_l = A$ and $I_l = I$. While the dimensions, cross sectional area A, and stiffness values E_l are given, $z_{l,i}$ can be varied by reordering the lamellas.

The objective function for the entire beam setup, in analogy to Equation (1.1), is defined as

$$f(\pi) = \min\left\{ EI_b(b_i) | b_i \in \Phi(\pi) \right\}. \tag{1.6}$$

As can be seen from Equation (1.5), for maximizing Equation (1.6) by reordering the lamellas, the term $E_l\, A_l\, z_{l,i}^2$ needs to be maximized. In other words, the higher E_l the larger $z_{l,i}$ should be. Based on this simplification, subsequently various approaches for using a deterministic algorithm, besides evaluating the entire solution space, are verified.

Assumption 1 *The desired arrangement, which maximizes Equation* (1.6)*, can be generated solely based on the lamellas' stiffnesses, without considering the beam they are used in.*

This assumption would allow finding a solution in a worst case within $n_{b,l}^2$ steps, which are needed to compare all lamellas with each other. Considering the alternative objective of optimizing the mean value of all beams' bending stiffnesses defined by Equation (1.5), the objective function can be defined as

$$f(\pi) = \max\left\{ \frac{\sum_{b_i \in \Phi(\pi)} EI_b(b_i)}{n_b} \right\} \,\widehat{=}\, \max\left\{ \sum_{b_i \in \Phi(\pi)} EI_b(b_i) \right\}. \tag{1.7}$$

Equation (1.7) can be transformed by substituting $EI_b(b_i)$ with Equation (1.5) to

$$f(\pi) = \max\left\{ \sum_{b_i \in \Phi(\pi)} \sum_{l \in L_i \equiv b_i} E_l\, I_l + E_l\, A_l\, z_{l,i}^2 \right\}. \tag{1.8}$$

$E_l\, I_l$ and A_l are independent of b_i, i.e., they will assume the same values regardless of how the lamellas are arranged in the beam setup. Thus, they can be factorized, which yields

$$f(\pi) = \max\left\{ \underbrace{\sum_{l \in L} E_l\, I_l}_{\text{constant by means of } \pi} + \underbrace{A_l}_{\text{constant}} \underbrace{\sum_{b_i \in \Phi(\pi)} \sum_{l \in L_i \equiv b_i} E_l\, z_{l,i}^2}_{\text{subject to the optimization}} \right\}. \tag{1.9}$$

The constant terms of Equation (1.9) can be neglected for the optimization problem, which leaves the last term as only term subject to the optimization. The desired permutation π which satisfies the demand is clearly achieved by ordering the lamellas in such a way that the stiffness increases with the distance to the center of mass of the beam.

This solution pattern is capable of finding the best possible solution for Equation (1.7), but fails on Equation (1.6) for unevenly distributed lamella stiffnesses. Assuming the following stiffness values $\boxed{E_1, E_2, E_3, E_4, E_4, E_4, E_5, E_6, E_7}$ for 9 lamellas which shall be distributed over three beams $\boxed{b_1, b_2, b_3}$ where $E_i > E_{(i+1)}$. The algorithm assigns the lamellas based on their stiffness values as follows:

1. Top outer position: $E_1 \to b_1$, $E_2 \to b_2$, $E_3 \to b_3$

2. Bottom outer position: $E_4 \to b_3$, $E_4 \to b_2$, $E_4 \to b_1$

3. Middle position: $E_5 \to b_1$, $E_6 \to b_2$, $E_7 \to b_3$

After Step 1 the beams bending stiffness decreases from b_1 to b_3. Step 2 should regulate the stiffness descent but in this case, as all lamellas have an equal stiffness value E_4, the beam order does not change. Step 3 should regulate the stiffness descent from Step 2, but as there was no descent, once again the order $b_1 > b_2 > b_3$ is favored, although the correct solution to Equation (1.6) is assigning the lamellas the other way around, to compensate Step 2. Therefore, it is not possible to find a solution to Equation (1.6) solely based on the lamellas' stiffness values.

Assumption 2 *As lamellas with high stiffness values should be placed furthest from the center of mass of the beam, the optimal location for each lamella can be defined only based on the lamellas stiffness and the beams with the furthest free positions.*

Assumption 2 is based on assumption 1 but the algorithm is capable to overcome the disadvantages of prescribing the order in which the lamellas are distributed over the beams. During the construction of the solution pattern the algorithm evaluates Equation (1.5) for the placed lamellas for each beam to decide which needs the current lamella the most.

To assure that every lamella is used at its most efficient position they are placed in an descending order by their stiffness value, starting from the outer layers of the beams. This restriction also follows assumption 2, as the most efficient way of placing the lamellas (without further knowledge of the beam they will be located in) is the proposed order. Assuming the following stiffness values $\boxed{2\,E_1, E_1, E_1, E_1, E_2, E_2}$ for 6 lamellas which shall be distributed over two beams $\boxed{b_1, b_2}$ where $E_i > E_{(i+1)}$, the algorithm assigns the lamellas based on their stiffness values as follows:

1. Top outer position: $2\,E_1 \to b_1$, $E_1 \to b_2$

2. Bottom outer position: $E_1 \to b_2$, $E_1 \to b_1$

3. Middle position: $E_2 \to b_2$, $E_2 \to b_1$

After Step 1 the beams bending stiffness decreases from beam b_1 to b_2. Based on the order after the first Step b_2 gets E_1. As the bending stiffness of b_2 now equals the bending stiffness of b_1 and b_1 offers a more efficient position, E_1 is assigned to b_1. This results in the order $b_1 > b_2$. The last Step is based on the same reasoning as Step 2, therefore the final order is $b_1 > b_2$.

Let the distance of the outer lamellas to the center of mass of the beam be 1. By evaluating Equation (1.5) for $I_l = 1$ and $A_l = 1$, the beam bending stiffnesses can be expressed by

$$EI_{b,1} = \underbrace{2\,E_1 + 2\,E_1}_{l_1} + \underbrace{E_1 + E_1}_{l_4} + \underbrace{E_2}_{l_6} = 6\,E_1 + E_2 \ \text{ and} \tag{1.10}$$

$$EI_{b,2} = \underbrace{E_1 + E_1}_{l_2} + \underbrace{E_1 + E_1}_{l_3} + \underbrace{E_2}_{l_5} = 4\,E_1 + E_2. \tag{1.11}$$

However, the solution, which fulfills Equation (1.6), is obtained by assigning all lamellas with a stiffness value of E_1 to beam b_2 and the remaining ones to b_1, which leads to

$$EI_{b,1} = \underbrace{2\,E_1 + 2\,E_1}_{l_1} + \underbrace{E_2 + E_2}_{l_5} + \underbrace{E_2}_{l_6} = 4\,E_1 + 3\,E_2 \quad \text{and} \tag{1.12}$$

$$EI_{b,2} = \underbrace{E_1 + E_1}_{l_2} + \underbrace{E_1 + E_1}_{l_3} + \underbrace{E_1}_{l_4} = 5\,E_1. \tag{1.13}$$

Both Equation (1.12) and Equation (1.13) give results that are bigger than the one given by eq. (1.11). This confirms that the solution provided by Assumption 2 cannot be used to find a solution which reliably maximizes Equation (1.6).

This observation further leads to the following conclusion: In order to find an optimal solution to Equation (1.6), the algorithm must be able to place lamellas at locations where they are not at their full potential and it is not possible to place lamellas purely based on the knowledge of the effects of the previously placed ones. Thus, it is likely that even this simplified problem cannot be solved by means of a deterministic algorithm without enumerating a large share of the search space, which would lead to long computation times and, therefore, as already stated in 1.2.3.1, optimization techniques are needed, which can deliver near optimal results without having knowledge of the entire search space.

1.2.3.3 Computational effort of the objective function

As stated in Sections 1.1.1 and 1.2.1, for the actual problem it is necessary to consider that the lamella's stiffness varies in longitudinal direction, which is described by the stiffness profile $E(x)$. Analytical beam theory based models like the one used for the simplified problem in Section 1.2.3.2 cannot be used in context of the inhomogeneous distribution along the longitudinal axis. Therefore, the deflection needs to be calculated by using an FE model.

The FE grid is constructed from 2D plane stress elements based on quadratic shape functions. The element height is defined in such a way that each lamella consists of two elements in height. The largest element length is 25 mm. The bond between the layers is assumed to be perfect.

As stated in Kandler et al. [68], a transversal isotropic material behavior is assumed. Further, only changes in the longitudinal stiffness profile $E(x)$ are considered, the Poisson's ratios ν_{21} and ν_{23} and the shear modulus G_{12} are assumed to be constant for all lamellas. Thus, the stiffness tensor for each lamella reads:

$$\mathbf{C} = \begin{bmatrix} \dfrac{E_1^2}{-E_2\,\nu_{21}^2 + E_1} & \dfrac{E_1\,E_2\,\nu_{21}}{-E_2\,\nu_{21}^2 + E_1} & 0 \\[2ex] \dfrac{E_1\,E_2\,\nu_{21}}{-E_2\,\nu_{21}^2 + E_1} & \dfrac{E_1\,E_2}{-E_2\,\nu_{21}^2 + E_1} & 0 \\[2ex] 0 & 0 & G_{12} \end{bmatrix} \tag{1.14}$$

The values are obtained from the micromechanical model described by Hofstetter et al. [62], which is also employed in Kandler et al. [68]. The main parameters for the micromechanical model are mass density and moisture content. The mass density is known for each lamella and, at the time of evaluation, the moisture content was 12 %.

As the evaluation of the objective function, particularly the calculation of the deflection using the FE model, is crucial for the computation time of the optimization process, the FE model itself is optimized as follows:

1. All finite elements have equal dimension.

2. Each finite element lies in only one lamella, i.e. it does not overlap or cross lamella boundaries.

3. Considering 1 and 2, it is possible to evaluate the element stiffness matrices for each finite element within every lamella once, before the actual optimization algorithm is run. The global stiffness matrix can be assembled by matching the global mesh coordinates with the local mesh coordinates within the lamellas.

4. The outer distances a_3 shown in Figure 1.2 are not taken into account as they have no impact on the load-bearing behavior of the beam.

Due to the vast impact of the objective function's computation time on the computation time needed for the overall optimization progress, a benchmark test of the described FE model is performed. The evaluation of the objective function involves the following steps:

1. Assembly of the mesh based on the lamella order L_i^*,

2. assembly of the global stiffness matrix **K** and

3. solving the system equilibrium $\mathbf{K}\,\vec{q} = \vec{p}$.

To eliminate random effects due to background processes, the times needed for each step are recorded for 1000 different beams. The results of those tests are displayed in Table 1.1. All computations were performed on a 2015 MacBook Pro with a 3.1 GHz Dual-Core Intel i7 CPU and 16 GB RAM.

Tab. 1.1: Resulting average, standard deviation and share on the computation time of the benchmark tests of 1000 different beams. Step 1 refers to the mesh assembly, step 2 to the assembly of the global stiffness matrix and step 3 to solving the system equilibrium equation.

	Computation time		
	Avg. [ms]	Share on Σ [%]	Std. dev. [ms]
Step 1	0.8	0.3	0.3
Step 2	80.9	27.7	56.4
Step 3	210.6	72.0	38.1
Σ	292.3	100.0	72.8

1.2.4 Metamodel

As shown in Sections 1.2.1 and 1.2.3.3, the computational effort for evaluating the FE model is too high to be used efficiently within the optimization procedure. Coelho et al. [28] suggest approximating the FE model with a regression model, further referred to as metamodel. This metamodel is derived based on a least squares regression [98, p. 245] for approximating the deflections obtained from the FE model. Compared to alternatives like support vector regression, artificial neural networks or nearest neighbor methods, this method is quite simplistic, however, it is sufficient for the stated problem and allows a quick initial training phase and a short evaluation time.

The regression is performed on 5000 beams generated based on the described example from Section 1.2.1. For validation, a test set of another 500 unknown beams is generated. To achieve well distributed lamella permutations both sets are created by the pseudo random beam generation algorithm introduced in Section 1.2.5.4.

1.2.4.1 Internal representation of beams

To implement the metamodel, a numeric representation of a beam is needed. As the geometry and the load of the beams are constant, the only varying component is the global stiffness matrix, respectively the changes induced by moving lamellas with varying stiffness profiles $E(x)$. Therefore, a beam can be represented by sampling the $E(x)$ profiles with a given resolution and using the result in a vector assembled as follows:

$$\vec{B}_i = (\underbrace{E_{i,1,1}, E_{i,1,2}, \ldots, E_{i,1,N_x}}_{\text{Lamella 1}}, \underbrace{E_{i,2,1}, E_{i,2,2}, \ldots, E_{i,2,N_x}}_{\text{Lamella 2}}, \ldots, \underbrace{E_{i,n_{b,l},1}, E_{i,n_{b,l},2}, \ldots, E_{i,n_{b,l},N_x}}_{\text{Lamella } n_{b,l}})^{\mathsf{T}}, \quad (1.15)$$

where $E_{i,j,k}$ is the value of the sampled $E(x)$ function for the lamella at position j in vector L_i^*. $E_{i,j,k}$ is calculated by computing the moving average with a window size of $\frac{l_b}{(N_x-1)}$ where l_b denotes the beam length. Respectively for the first and the last sample the window size is $\frac{l_b}{2\,(N_x-1)}$. N_x denotes the number of samples generated based on the resolution.

1.2.4.2 Implementation of the regression algorithm

The basic idea behind the implementation is that the FE model calculations can be approximated solely based on the vector $\vec{B}_i$. The resulting approximate deflection $\tilde{q}_{\max}$ is calculated by performing an inner product on the vector $\vec{B}_i$ and a weighting vector $\vec{w}$:

$$\tilde{q}_{\max} = \vec{B}_i\,\vec{w} \tag{1.16}$$

The regression is performed based on two variations of $\vec{B}_i$:

1. *The inverse of every entry in $\vec{B}_i$.* This is insofar arguable as a higher modulus of elasticity reduces the deflection. Thus, the index originally representing the k-th sampled element, in the lamella at location j in beam i is used as follows

$$\vec{B}_{i,j,k}^{(1)} = \frac{1}{E_{i,j,k}}. \tag{1.17}$$

2. *In addition to the variation in 1, weighting every element $E_{i,j,k}$ by $\frac{E_{i,j,k}}{\bar{B}_i}$, where $\bar{B}_i$ is the average of all values in $\vec{B}_i$.* This weighting intends to simulate the effect that stiffer regions tend to attract stresses. Thus, the index originally representing the k-th sampled element in the lamella at location j in beam i is used as

$$\vec{B}_{i,j,k}^{(2)} = \frac{1}{E_{i,j,k}}\,\frac{\bar{B}_i}{E_{i,j,k}}. \tag{1.18}$$

To obtain the unknown values of the weights $\vec{w}$, a least squares approach [98, p. 245] is used:

$$\text{Minimize: } L_m = \frac{1}{n}\sum_{i=1}^{n}\frac{1}{2}\left(q_{\max,i} - \vec{B}_i^{(m)}\,\vec{w}\right)^2 + \frac{\alpha}{2}\underbrace{\sum_{j=1}^{N_x\,n_{b,l}}\left([w_j]^-\right)^2}_{\text{Constraint } \forall w_j | w_j \geq 0}, \tag{1.19}$$

where n is the number of beams in the training set, w_j is the j-th element in the weighting vector $\vec{w}$, α is the scaling factor for the non-smooth penalty function and the notation $[\bullet]^-$ is defined as $\max\{0, -\bullet\}$ [98, p. 507]. The non-smooth penalty function constrains w_j to positive values. The constraint assures that

$\vec{B}_i^{(m)} \vec{w}$ stays positive, i.e. the deflection returned by the metamodel is nonnegative. Nevertheless, the eager learner is also tested for $\alpha = 0$.

The actual values for $\vec{w}$ are obtained by performing a numerical optimization by using the limited-memory-BFGS (L-BFGS) algorithm [98, p. 177]. The gradient function used for L-BFGS is computed by using stochastic gradient descent (SGD) [19] on a random number of beams from the set used for the regression. The usage of SGD reduces the number of calls to the gradient function by calculating the gradient based on a portion of the training set. Furthermore, the added stochastic effect reduces the chance that the optimization gets stuck at a local minimum.

As stated above, the metamodel is optimized based on the two different variations of $\vec{B}_i$. Additionally, for each variation the constraint α is either respected or ignored (i.e. $\alpha > 0$, $\alpha = 0$). Therefore, in total, four different parameter combinations, as shown in Table 1.2, are tested.

Tab. 1.2: Parameter combinations for the eager learner

	SGD size[a]	α	w_0[b]	Var. of $\vec{B}_i$	Resolution[c]
1			10^{-3}	1	
2		0.0	10^{-3}	2	
3	50		10^{-12}	1	50
4		1.0	10^{-12}	2	

[a] The number of samples for which the gradient is calculated.
[b] w_0 is initially populated with random numbers equally distributed between 0 and 1 and is scaled by the given factor.
[c] The resolution is given in number of segments in longitudinal direction per lamella.

The performance of the algorithm is tested with the verification set of 500 unknown beams and compared with the deflection obtained by the FE model. The quality of the approximation is determined by the so-called coefficient of determination [34, p. 484] denoted by R^2. The coefficient of determination measures the precision of a linear regression model of explaining variation in the input data.

As can be seen from the results in Figure 1.3, parameter sets 1 and 3 (using no further weighting of $E_{i,j,k}$) perform better on the test set. Furthermore, by deactivating the non-smooth penalty function, it is possible to improve the correlation.

Especially for genetic algorithms (GAs) the absolute value of the deflection is not crucial, as solutions are compared against each other. Rather, it is more important that the approximation is able to correctly predict whether one beam is better than another one. Thus, the performance is further rated by comparing the results of a tournament selection, using a tournament size of $t = 6$. The selection process is repeated 20000 times to reduce the stochastic effects involved in the selection method. The quality of the approximation is quantified by the correlation coefficient [34, p. 209] of the density functions, resulting from the FE model and the learning algorithm.

Similar to the first method, parameter combination 1 outperforms the others with a correlation coefficient of 0.84, compared to 0.46 for combination 2, 0.62 for combination 3 and 0.46 for combination 4. Furthermore, even though the learning algorithm is entirely unfamiliar with the test set, the selection based on the approximate model matches the one based on the FE model well. Subsequently the metamodel will only be used with parameter combination 1.
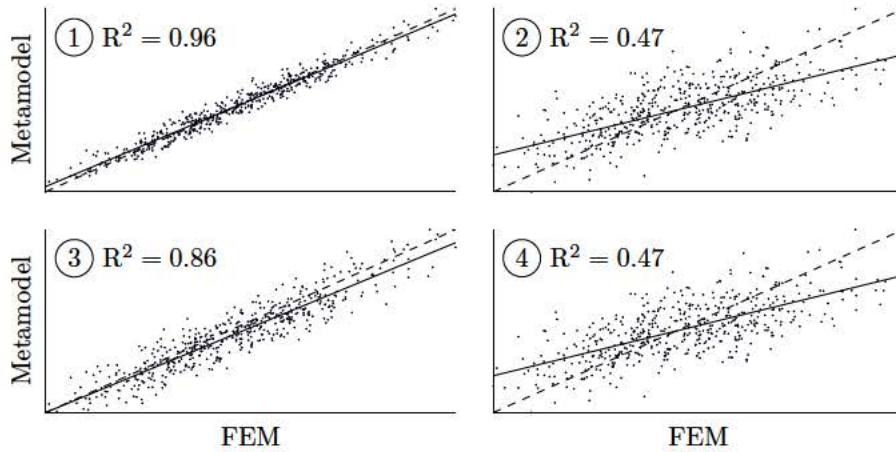
Fig. 1.3: Approximated deflection of the test set for parameter combinations 1 to 4, compared with the deflection obtained by the FE model

1.2.5 Optimization methods

1.2.5.1 General considerations regarding the implementation

Based on the following insights to the problem's complexity from Sections 1.2.3.1 to 1.2.3.3

- "The problem cannot be solved by a simple, deterministic algorithm.",

- "The search space is too large to be evaluated in its entirety." and

- "The evaluation of the objective function is computationally expensive."

the class of applicable algorithms is narrowed down to random search methods. In this paper, a subclass, namely MAs is implemented. Especially for the task of a CO problem local search (LS), iterated local search (ILS) and GAs can be applied [17, 51].

In order to use the map Φ, introduced in Section 1.2.2, in context of the mentioned algorithms, it is further specialized for two different mappings, which define L_i^* and thus allow the formulation of Φ. From the mentioned MAs, LS and ILS are independent of the linking type, chosen for Φ, which becomes evident in Sections 1.2.5.2 and 1.2.5.3. GAs on the other hand are considered to be sensitive to the definition of Φ, due to the processes involved during crossover. This is expressed in the so-called building block hypothesis described by Holland et al. [64] and Goldberg [53]. The building block hypothesis states that a chromosome's fitness value is vastly influenced by short subsequences of the chromosome. Therefore L_i^* is once defined regarding the building block hypothesis as

$$L_i^* = \left\{ \pi^*(k) | k \in \{i + j\, n_b\}_{j=0}^{n_{b,l}-1} \right\}, \tag{1.20}$$

and alternatively without considering building blocks as

$$L_i^* = \left\{ \pi^*(k) | k \in \{n_{b,l}\,(i-1) + j\}_{j=1}^{n_{b,l}} \right\}. \tag{1.21}$$

Equation (1.20) assures that important positions within the beams contained in the solution, i.e. the outer layers (compare Section 1.2.3.2), are grouped within the chromosome. Subsequently the mapping based on Equation (1.20) will be referred to as chromosome type A and the mapping based on Equation (1.21) as chromosome type B. LS and ILS will solely be based on type B, however herein the term chromosome is substituted with the term list as they are synonymous within the given context.
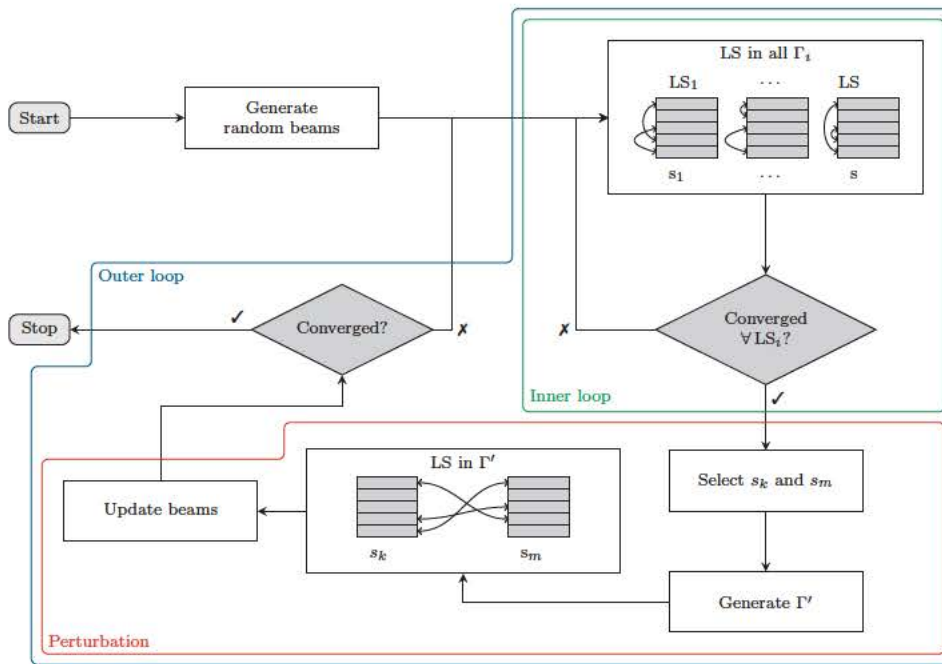
Fig. 1.4: Overview of the implemented ILS algorithm.

1.2.5.2 Implementation of local search

The used LS algorithm is implemented in accordance to Lourenço et al. [80] as follows: Let s denote the currently best known solution to Equation (1.1). The neighborhood Γ, LS operates on, is generated around s such that the solutions contained in Γ have a high resemblance to s. This is achieved by performing every possible swap of two lamellas and flipping every lamella in s. The number of alterations of s for generating Γ, i.e. the cardinality of Γ, is $|\Gamma| = \frac{(n_l - 1)\, n_l}{2} + n_l$.

As the evaluation of the computationally expensive objective function is not possible for the entire neighborhood the implementation is further adapted: In order to reduce the number of calls to the objective function f, the first randomly picked solution $s^* \in \Gamma$ for which $f(s) \geq f(s^*)$ is accepted as new solution to the optimization problem. Additionally, the LS algorithm is endowed with a termination criterion [52, p. 48] which stops the search on newly generated neighborhoods after N_c steps of no improvement.

1.2.5.3 Implementation of iterated local search

As described by Lourenço et al. [80], LS can be enhanced by applying perturbations to generate new not yet visited neighborhoods. A reasonable definition of the neighborhood is as follows: The LS algorithms are bound to one beam only and the perturbation is applied in form of an interchange of lamellas between two distinct beams. This implies that the LS operates on a smaller neighborhood than the one proposed in Section 1.2.5.2. Figure 1.4 shows an overview of the described algorithm.

For the stated problem, n_b different LS computations are employed in an inner loop, where each is defined as follows: Let the objective function for LS_i be defined as

$$f(s_i) = q_{\max}(b_i) \tag{1.22}$$

and let the neighborhood Γ_i around the current solution s_i be generated by performing every possible swap of two lamellas within s_i and flipping every lamella within s_i ($|\Gamma_i| = \frac{(n_{b,l} - 1)\, n_{b,l}}{2} + n_{b,l}$).

Each LS$_i$ run is endowed with a convergence criterion which stops the search on Γ_i after N_c steps of no improvement. This guarantees the optimal layout for each beam, given the corresponding set of lamellas. After all n_b LS computations have converged, the worst solution denoted by s_k and a randomly chosen solution denoted by s_m, $s_m \neq s_k$, are picked. Subsequently, the perturbation is implemented by defining a new LS which searches in the neighborhood $\Gamma' = L_k^* \times L_m^*$ where L_k^* denotes the lamellas used in solution s_k and L_m^* denotes the lamellas used in solution s_m. For the pair $p_i \in \Gamma'$ of lamellas to be swapped between the solutions s_k and s_m two new solutions $s'_{k,i}$ and $s'_{m,i}$ are generated. The corresponding objective function f' is defined as

$$f' : \begin{cases} 0, & \text{if } f(s'_{k,i}) < f(s_k) \text{ and } f(s'_{m,i}) < f(s_k) \\ 1, & \text{if } s'_{k,i} = s_k \text{ and } s'_{m,i} = s_m \\ 2, & \text{otherwise.} \end{cases} \tag{1.23}$$

This leads to the effect that a perturbation is only accepted if the newly generated beams are better than the previously worst beam s_k. Consequently, in case $f' = 0$, the resulting beams $s'^*_{k,i}$ and $s'^*_{m,i}$ replace s_k and s_m, respectively. For this LS procedure, no convergence criterion is needed, as the search stops immediately after finding a pair p_i which satisfies $f' = 0$. However, in case Γ' is exhausted no interchange is performed and another beam s_m is chosen to generate Γ'.

As convergence criterion for ultimately stopping the outer loop, the coefficient of variation c_v is used, which decreases as all beams become similar. Therefore, further LS on Γ' will not lead to any improvement. The criterion can be formulated as $c_v[f(s_i)|i \in \{1, \ldots n_b\}] \leq \epsilon_c$, where $\epsilon_c \in \mathbb{R}$ and $\epsilon_c > 0$.

1.2.5.4 Implementation of genetic algorithms

Within the GA approach the so called fitness function is maximized, hence as $q_{\max}(b_i) \neq 0 \, \forall \, b_i$ the objective function can be reformulated as

$$f(\pi^*) = \min \left\{ \frac{1}{q_{\max}(b_i)} | b_i \in \Phi(\pi^*) \right\}. \tag{1.24}$$

The GA is mainly implemented based on the procedures laid out in Goldberg [53], Reeves [112], Baker [10], Blickle and Thiele [16], Fox and McMahon [47] and Larranaga et al. [77]. Numerous selection, crossover and mutation methods are implemented and validated. Besides the mentioned algorithmic states, two phases, namely the generation of the initial population and the chromosome repair phase, are specialized for the stated problem.

Reeves [113] addresses the situation of different permutations actually representing equal solutions. It was already mentioned in Section 1.2.3.1, that the order in which the beams occur within a chromosome, has no effect on the actual solution. The implemented crossover operations are designed to generate offspring based on two parent chromosomes. Therefore, when combining two equal chromosomes, the generated offspring must be equal as well. However, as a single solution can be represented by multiple chromosomes this is not guaranteed. Thus, subsequent to the mutation a chromosome repair is performed, where the beams contained in the chromosome are sorted such that a given set of beams always appears in the same order.

Multiple sources [112, 114, 131] address the generation of the initial population. The aim is to obtain a diversified initial population, which covers the search space adequately. Otherwise an unsuitable initial population could cause premature convergence or reduce the exploratory capabilities of the GA.

Reeves [114] proposed the principle that every solution within the search space should be reachable by crossover only. This implies that every allele must be at each locus at least once within the population.

Based on this principle, Reeves [114] derived an equation to calculate the probability that every allele is present at every locus based on the population size, the chromosome length and the number of alleles.

This approach apparently works for problems with small number of alleles, but for larger numbers the minimum population size tends to be too large to be usable [114]. Furthermore, the used principle does not hold for CO problems, since herein, the used crossover operations incorporate swapping operations and therefore are able to reach solutions with alleles at positions which were not present in the initial population.

Coelho et al. [28], Reeves [112], and Talbi [131] propose the usage of latin hypercube sampling to generate a pseudo random initial population. However, for CO problems, where the genes cannot be sampled independently, latin hypercube sampling is not applicable as well. Therefore, the method used in this paper is a modified implementation of the so-called algorithm P used for shuffling, introduced by Knuth [72, p. 139]. Herein, the algorithm is modified such that lamellas are evenly distributed over all available positions by rejected randomly picked locations in case the lamella was used an above average amount of times at this position with the assigned orientation.

1.2.5.5 Parameter tuning for genetic algorithms

The large number of different parameters and different operations applicable within GAs makes finding an optimal parameter set a challenging task. De Jong [31] discusses this topic on a general level and compares the usage of static and dynamic parameter setting strategies.

Tab. 1.3: Used parameter values and ranges for the parameter sweeps.

Population size	20–100
Mutation rate	0.0–1.0
Crossover rate	0.0–1.0
Elitism	0–10
Chromosome	Type A or B
Crossover	Partially mapped crossover
	Ordered crossover
	Cycle crossover
Mutation	Swap two lamellas or flip one
	Replace with random beam setup
Selection	Roulette-selection
	Stochastic universal selection
	Tournament selection
	Linear ranking
Initial population	Pure random
	Pseudo random
Stochastic universal selection and roulette selection	
Fitness scaling	1.0–20.0
Tournament selection	
Tournament size	2–10
Linear ranking	
Selection pressure	1.0–2.0

As the fitness landscape of the stated problem does not change during the run, online parameter tuning will not be used. De Jong [31] further proposes so-called parameter sweeps, where every possible value and combination of parameters is tested, in order to find an optimal static parameter setting. The computational effort for these tests for a number of different initial populations is, similar to the problem

discussed in this paper, very large. Therefore, the tuning process is done by using performant racing algorithms [86]. For this purpose, the free software package irace [79] is used. The parameters are bound to the ranges and values shown in Table 1.3. Ranges delimited by integer numbers refer to integer numbers only whereas ranges delimited by real numbers refer to real numbers with a precision of two decimal places.

The parameter sweeps are performed on the example from Section 1.2.1 on a number of 250 and 1000 generations. The maximum number of experiments is set to 5000, where one experiment is one optimization run with a given parameter model.

The best five parameter configurations are shown in Table 1.4. The best parameter configurations are those which on average delivered the best results while maintaining a small innerquartile range for 250 and 1000 generations. The solution quality for the five parameter combinations is shown in Figure 1.5. The best results are achieved by using a completely random initial population, large mutation rates of up to 100 % and solutions waiving elitism. Interestingly, parameter combination 3 uses a mutation rate of 100 % an no elitism, causing mutation on even the best population members in each generation.

Tab. 1.4: Top five parameter combinations for the original problem using the eager learner

	Parameter combination				
	1	2	3	4	5
Population size N_p	79	89	93	94	100
Mutation rate p_m	0.94	0.94	1.00	0.99	0.99
Crossover rate p_c	0.90	0.55	0.97	0.88	0.86
Elitism ϵ_c	1	1	0	0	3
Crossover function f_c	Partially mapped crossover				
Mutation function f_m	Swap or flip				
Selection function f_s	Tournament selection				
Chromosome type	B				
Initial population	Random initial population				
Tournament size t	10	8	9	9	9
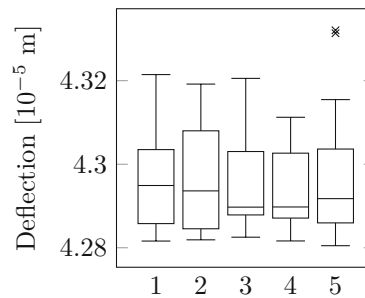
Fig. 1.5: Solution quality for the parameter combinations 1 to 5 from Table 1.4.

1.3 Results and discussion

1.3.1 Optimization runs

In the following LS, ILS and the GAs, adjusted according to the five parameter combinations from Table 1.4, are used for the optimization. The progress of the optimization procedures is shown in Figure 1.6, starting from 100 different initial beam setups for LS and ILS and 50 different initial beam setups for GAs. Due

to the complexity of the objective function, the overhead of the computation time spent on the algorithm is neglectable in relation to the computation time needed for evaluating the objective function. Therefore, in order to provide a basis for comparing the different algorithms, the progress is always plotted in comparison to the number of distinct calls to the metamodel, i.e. the number of distinct beams calculated throughout the optimization.
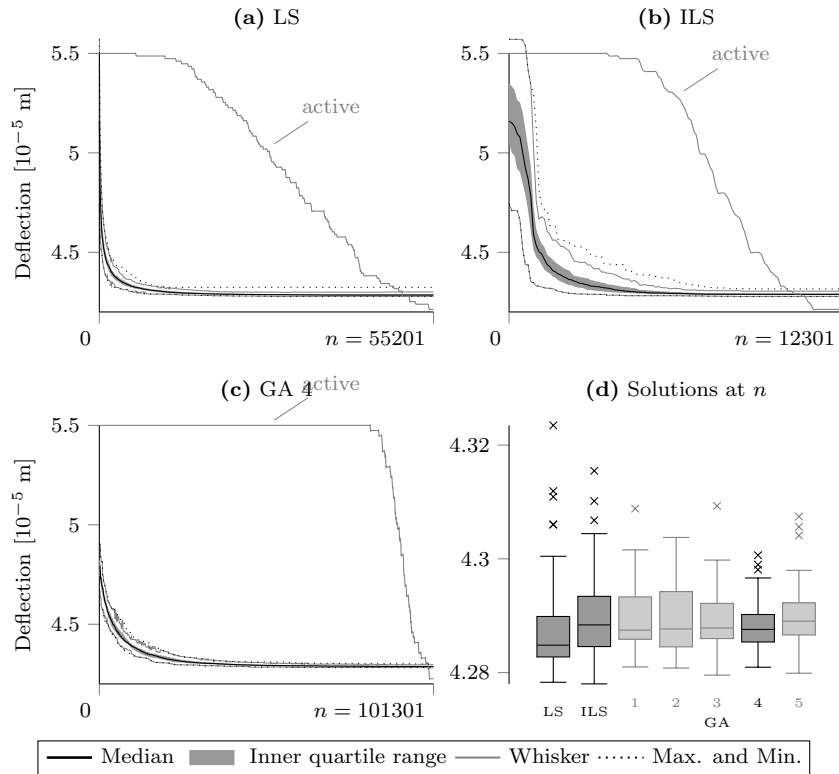
Fig. 1.6: Results of 100 optimization runs for LS and ILS, and 50 optimization runs for GAs, where a shows the LS algorithm, b the ILS algorithm and c the GA parameter combination 4 from Table 1.4. d shows the distribution of the resulting deflection at step n, where n denotes the number of distinct metamodel evaluations. a to c show an additional path label "not converged". This path visualizes the number of active optimization runs, starting with 100 % at 0 and ending with the last run at n.

Table 1.5 shows a summary of the results obtained from the tested MAs. Based on these results, it is possible to draw the following conclusions:

1. The best solutions are reached by LS and ILS, albeit the other algorithms performed similar.

2. When comparing the worst solutions of the test runs, the GAs managed to reach the best results. Despite LS found the best solution, the runs also contained the worst solutions of all discussed algorithms. This is further reflected in the high standard deviation and a wider inner quartile range shown in Figure 1.6d.

3. ILS managed to reach the highest average deflection significantly faster than all other algorithms.

4. The GA using parameter combination 4 outperforms the other GAs, as this combination delivers the lowest standard deviation of all algorithms, the highest best value of all GAs, and performs on average similar to LS. Furthermore, the GA using parameter combination 4 shows the lowest amount of runs which never reach the highest average value. This is also reflected in a narrow data

range shown in Figure 1.6. Causes for that might be that a slightly higher mutation rate and not using elitism provides a broader search field.

Generally, it should be noted that all algorithms deliver results within a range of 1.0 % between the best and the worst result obtained by LS. This emphasizes the usage of MAs for the current task of optimizing the load-bearing behavior of GLT beams.

Tab. 1.5: Solutions of 100 runs of LS and ILS, where $f(\pi^*)$ is used as the objetive function, and 50 runs of GAs, where $1/f(\pi^*)$ is used as objective function.

	LS	ILS	GA 1	GA 2	GA 3	GA 4	GA 5
	Deflection in $[10^{-5}\,\mathrm{m}]$						
Best	**4.278**	**4.278**	4.281	4.281	4.279	4.281	4.280
Worst	**4.324**	4.316	4.309	4.304	4.308	4.301	4.307
Avg.	**4.287**	4.289	**4.290**	**4.290**	4.288	4.288	**4.290**
Std.	0.008	0.007	0.006	0.006	0.006	0.004	0.006
	Step count for reaching the highest avg. value of 4.290						
Earliest	10 001	2824	20 698	33 076	31 593	38 136	30 735
Avg.	18 971	5936	44 564	46 857	59 335	59 943	51 850
%-Never	26.0	38.0	38.0	42.0	30.0	22.0	38.0

The present findings suggest the following two choices of algorithms in order to solve the optimization problem:

- ILS should be used when it is important to find good solutions in a minimal amount of time. Compared to LS, ILS reaches good solutions faster and is likely to be able to escape local minima. However, compared to GAs the algorithm is less robust.

- GAs should be used when it is important that the algorithm delivers good solutions in every run and when computation time is of secondary importance. Apparently, parameter combination 4 delivers the best results among the other GAs. When using algorithms without elitism, it is important to notice that the best solution is not necessarily contained in the last generation.

1.3.2 Quantification of a range of possible improvement

So far, the resulting deflections have only been shown in context of the initial beam setup or the results of the other algorithms. However, this does not allow a quantification of the actual improvement as both, the starting beam setup and the results of the other algorithms depend on how "good" the initial quess was. Therefore, to be able to determine a possible range of improvement, the objective function from Equation (1.1) shall be, instead of being minimized, maximized. Hence, resulting in a π^* containing the beam with the maximum possible deflection.

The optimization is performed by using the GA on the practical example from Section 1.2.1. The optimization process was stopped after 2000 generations resulting in a maximum deflection of 6.166×10^{-5} m which, compared to the results from Section 1.3.1, leads to a range of possible improvement of 30.62 % between the worst and the best solution. Given that this result is based on the Assumption of constructing the worst possible beam, it is practically unlikely to have such a large improvement. Therefore, to assess a more realistic approach for constructing GLT beams, 1000 random beams, constructed from the 50 lamellas subject to the practical example, are calculated using the FE model. On average the resulting beams have a deflection of 5.176×10^{-5} m with a coefficient of variation of 0.035, which results in a possible improvement of 17.35 %.

1.3.3 Determining the effect of combined sets of T14 and T22

The procedure outlined in Section 1.3.2 to construct GLT beams is based upon an entirely random combination of lamellas. However, as described in Section 3.1 it is common practice to optimize the material usage within the construction of GLT beams by combining lamellas of different grading classes into one beam. Therefore, to determine the possible improvement for already optimized GLT beams, an alternative set of lamellas, shown in Table 1.6, is assessed. Herein, lamellas 1–20 are picked from grading class T14 and lamellas 21–50 from grading class T22. When comparing the longitudinal stiffness profiles of both grading classes, it is obvious that the lamellas from T14 have overall lower values for $E(x)$ and a larger amount of knots.

As described in Section 1.3.3, to be able to quantify the performance of the optimization in a more realistic manner 1000 random beams are constructed. In order to consider that combined GLT beams are built with stronger lamellas in the outer layers, the beams are constructed such that the outer two layers on each side consist of lamellas of grading class T22 only. The resulting beams have an average deflection of 5.496×10^{-5} m with a coefficient of variation of 0.04. The maximum deflections obtained from ILS and the GA are 4.580×10^{-5} m and 4.508×10^{-5} m resulting in an improvement of 16.67 % and 17.98 %, respectively.

A visualization of the longitudinal stiffness profile $E(x)$ for every beam contained in this solution is shown in Figure 1.7b. When looking at the highlighted area **A** in the first beam, it is apparent how the optimization algorithm manages to gather "weak" sections close to the beams center of mass. This is consistent with the findings from Section 1.2.3.2.

Figure 1.7b shows the locations of lamellas from grading class T14 in the final solution. Against the initial Assumption, the best solution is not obtained by placing lamellas with lower grades on the inner layers. The actual result is quite contrary as beams 1, 2, and 3 have lamellas from grading class T14 within the outer two layers. Furthermore, beam 1 is almost entirely built from grading class T14, without being the beam with the highest deflection (Table 1.7). These results support the introductory statements in Section 3.1, outlining the downsides of prescribed grading classes, as through rearranging areas containing weaknesses to areas of small stresses, seemingly weak boards can be used optimally.
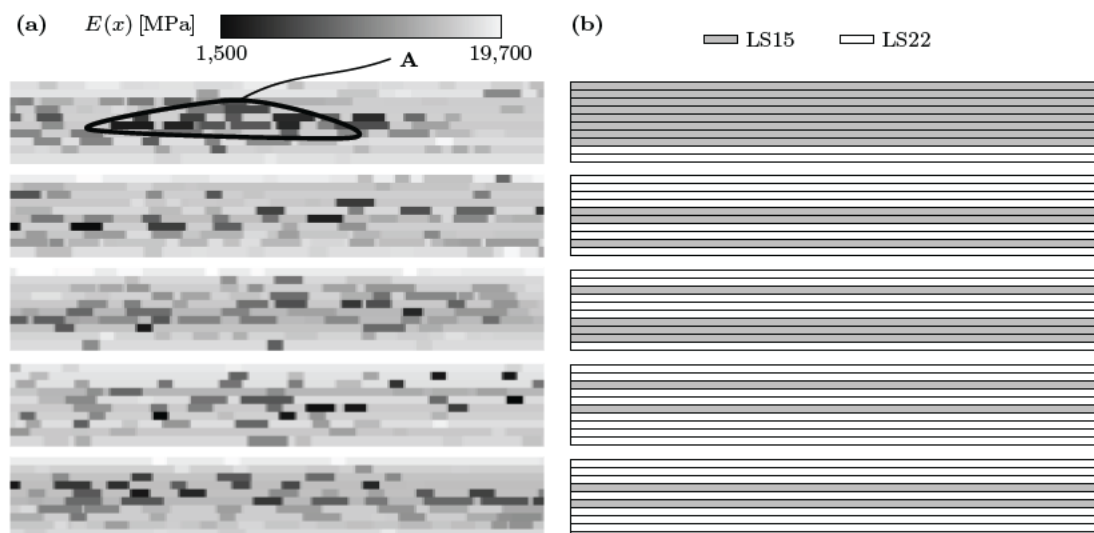
Fig. 1.7: Resulting beam setup from the optimization using a GA. a shows a heatmap of $E(x)$ for every beam contained in the best solution. The area **A** clearly shows how "weak" regions are gathered close to the center of mass. b shows the beams contained in the best solution with highlighted locations of lamellas from grading class T14.

Tab. 1.6: Lamellas used in the optimization problem

ID	GC	Nr.	$E(x)$	ID	GC	Nr.	$E(x)$
01	T14	43		26	T22	85	
02	↓	44		27	↓	86	
03		45		28		87	
04		46		29		88	
05		47		30		89	
06		48		31		90	
07		49		32		91	
08		50		33		92	
09		51		34		93	
10		52		35		94	
11		53		36		95	
12		54		37		96	
13		55		38		97	
14		56		39		98	
15		57		40		99	
16		58		41		100	
17		59		42		101	
18		60		43		102	
19		61		44		103	
20		62		45		104	
21	T22	80		46		105	
22	↓	81		47		106	
23		82		48		107	
24		83		49		108	
25		84		50		109	

$E(x)$ is equally scaled for every lamella.

The column *ID* contains the identification number used in this paper to identify the used lamellas.

The column *Nr.*, combined with the grading class from column *GC*, allow the identification of a lamella in the experiments from Serrano and Enquist [121]. In Serrano and Enquist [121] grading class LS15 matches T14 and LS22 matches T22.

Tab. 1.7: Near optimal beam setup for the optimization problem with combined lamellas from grading classes T14 and T22. Lamellas marked with an asterisk are built into the beam flipped.

	Beams				
	1	2	3	4	5
Top	16*	21	28	32	36*
	14*	33	47	37*	35*
	03	46	05*	18	43
	17	25*	31	23*	13
	20	11*	22*	44*	49*
	01	12*	38*	09*	07
	10	27	08	48	45*
	04	50	06	39	19
	24*	15	02*	30*	29
Bottom	41	26	40	42*	34*
Deflection $[10^{-5}\text{m}]$	4.4753	4.4575	4.5067	4.5076	4.4642

1.3.4 Optimization with removal of weak lamellas

So far, the optimization task was always bound to $n_l = n_b\,n_{b,l}$. As stated in Section 1.2.1 another interesting task is to optimize the arrangement for $n_l > n_b\,n_{b,l}$. This adaption allows the algorithm to remove comparably weak lamellas, which are of no use when building GLT beams. To be able to cope with this task, the described implementations of the MAs need to be adapted. As ILS and GAs prove to perform well for the given task, changes are only made for those two algorithms.

1.3.4.1 Adaption of the genetic algorithm

To allow the algorithm to utilize lamellas that will not be built into a beam, π^* must contain all lamellas. Hence, the initial definition of π^*, given in Section 1.2.2, is applicable for $n_l > n_b\,n_{b,l}$. During crossover, selection, and mutation the GA is unaware of the existence of beams since the chromosome equals π^*. In Section 1.2.5.4, two additional states of the algorithm are mentioned, namely the generation of the initial population and the chromosome repair phase. The initial population is dependent on the generated beams as its locations within the beams are recorded. However, as the parameter sweep from Section 1.2.5.4 clearly favors a pure random initial population, this phase remains as described. The chromosome repair on the other hand depends on the resulting beams and must be able to neglect the order of unused lamellas.

As shown π^* remains as defined, hence the remaining unverified part of Equation (1.1) is Φ. The parameter sweep from Section 1.2.5.4 favored a chromosome representation without considering building block, therefore further only Equation (1.21) will be used. As Equation (1.21) is defined in terms of $n_{b,l}$ and under the assumption that every beam contains an equal number of lamellas, it is possible to generate L_i^* for all b_i independent of n_l. Furthermore, the definition of Φ in Equation (1.2) is made in terms of n_b, hence it also holds for $n_l > n_b\,n_{b,l}$. Additionally, this defines the arrangement of the chromosome, as all lamellas at positions larger than $n_b\,n_{b,l}$ are not assigned to a beam. By implication this means the first $n_b\,n_{b,l}$ places in the chromosome define the resulting beams. These findings leave the need to only adapt the chromosome repair function as follows:

The implementation described in Section 1.2.5.4 performs three steps to repair a chromosome:

1. Use Φ to generate a vector of beams from the chromosome.

2. Sort the vector of beams by the top most lamella in every beam.

3. Reassemble the chromosome based on the sorted vector of beams.

The flaw in context of this workflow is, that during Step 1 the unused lamellas are discarded. Therefore, the unused lamellas need to be considered during the reassembly and furthermore, as stated in Section 1.3.4.1, as well be repaired in form of sorting them. This ensures that during crossover equal parent chromosomes result in equal child chromosomes. Hence, the previous workflow is extended as follows:

4. Sort the unused lamellas.

5. Attach the sorted, unused lamellas to the reassembled incomplete chromosome from Step 3.

1.3.4.2 Adaption of iterated local search

As described in Section 1.2.5.3, ILS optimizes beams on different scopes, namely local to the beam and between two defined beams. As the introduced change of $n_l > n_b\, n_{b,l}$ does not affect $n_{b,l}$, the local optimization procedure is inherited as defined. The extension takes place on the level of the interchange of lamellas between beams, as not only swaps between two beams, but also swaps between one beam and the set of unused lamellas shall be performed. In accordance to the suggested implementation it is viable to assume that the unused lamellas can be treated as a beam-like construct as well. Hence, it is possible to apply the neighborhood definition Γ' from Section 1.2.5.3. However, a swap between a beam and the set of unused lamellas must not be made regarding the same restriction, as the set of unused lamellas does not need to improve. Therefore, the objective function f' in Equation (1.23) must be adapted as

$$f' : \begin{cases} 0, & \text{if } f(s'_{k,i}) < f(s_k) \\ 1, & \text{if } s'_{k,i} = s_k \text{ and } s'_{m,i} = s_m \\ 2, & \text{otherwise} \end{cases} \tag{1.25}$$

This leads to the effect that a perturbation is only accepted if the actual beam, involved in the swap, is better than the previously worst beam. In comparison, the restriction of not worsening beam b_m or solution s_m is omitted as in this case b_m is not part of the actual solution. For interchange of lamellas between actual beams, Equation (1.23) can still be used. The algorithm is endowed with a second convergence criterion, which ensures that after a number of unsuccessful tries of swapping lamellas with the set of currently not used lamellas, the focus is set on optimizing the actual beams.

1.3.4.3 Results of the optimization for sorting out weak lamellas

The optimization is performed using ILS and the GA. Both algorithms are tested on the example described in Section 1.3.3 for $n_b = 4$ and $n_{b,l} = 10$, allowing a number of 10 lamellas to be removed from the final solution.

During the optimization procedure the lamellas 1, 7, 8, 12, 20, 23, 38, 44, 45, 49 are removed by ILS and the lamellas 1, 7, 8, 9, 13, 20, 22, 38, 44, 49 are removed by the GA. Compared to the solution for $n_b = 5$ in Section 1.3.3, mainly lamellas from the inner layers are removed. Figure 1.8 shows the locations where the removed lamellas were built into the beam in the final solution from Section 1.3.3.

Figure 1.8 clearly shows the correlation between putting weak lamellas into the inner layers and the adapted algorithms being able to spot those weak lamellas. This result further substantiates the applicability and flexibility of the used algorithms.
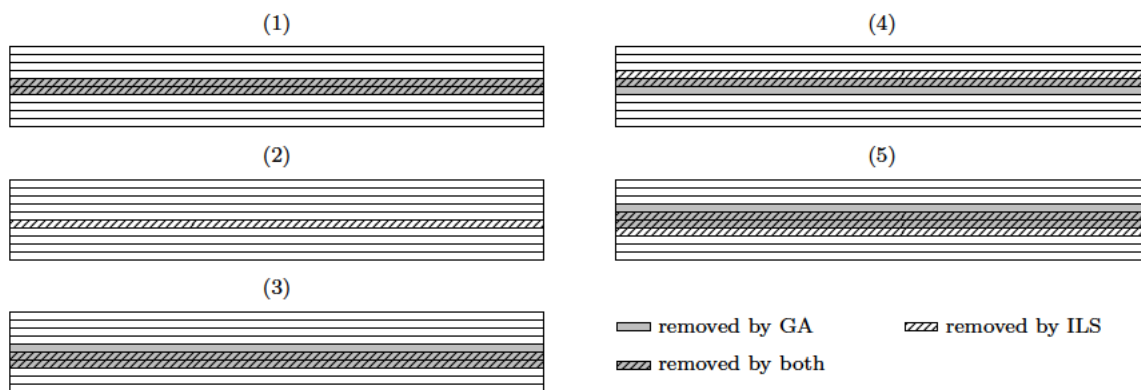
Fig. 1.8: Locations of lamellas removed during the optimization procedure from the beams 1–5 from the near optimal solution in Section 1.3.3.

1.4 Conclusion

In this paper the problem of optimizing the load-bearing behavior of GLT beams is discussed in detail and a mathematical formulation is derived. Based on this formulation three metaheuristic optimization algorithms are implemented and validated. Within the optimization algorithms a metamodel is used to bypass the computationally expensive evaluation of the FE model, used to calculate the beams' deflection. Based on the findings the following conclusions can be drawn:

- The task of reducing the deflection of multiple beams through rearranging the lamellas is not, even for a problem with a constant longitudinal stiffness for each lamella (see Section 1.2.3.1) easily solvable. In order to achieve the objective to minimize the maximum deflection of all beams, lamellas might be placed at ineffective positions, where their potential is not fully exploited. Therefore, to obtain good solutions for the optimization problem, in a reasonable time frame, metaheuristic algorithms are needed.

- The introduced metaheuristic algorithms prove to be applicable for performing combinatorial optimization tasks for GLT beams and are capable to find near optimal solutions to the stated problem. ILS and GA managed to outperform LS as specialist in their domain:

  - ILS is able to find solutions to the stated problem with a minimum amount of objective function evaluations. However, the solution quality strongly depends on the initial solution.

  - GAs found some of the best solutions for the problem, yet needing almost 10 times more evaluations of the objective function than ILS. Nevertheless, they also prove to be very robust, thus delivering very good solutions, independent of the initial population.

- The used metamodel is able to estimate the maximum deflection of a beam, after performing a regression on results from the FE model, very well.

- The range of possible improvement of the load-bearing behavior depends on the quality of the lamellas, i.e. the variability of $E(x)$. This is reasonable, as lamellas from grading class T14 have a larger variability in $E(x)$ and thus the algorithm can construct more diverging solutions. For the discussed examples in Sections 1.3.2 and 1.3.3 the possible improvement, compared to how GLT beams and combined GLT beams are commonly produced, ranges from about 15 % to 20 %.

It is even possible to improve GLT beams assembled under consideration of placing lamellas of higher grading classes in the outer layers of the beam, as during grading the lamella is not classified

with respect to its actual usage. This is shown in Section 1.3.3 as against the initial assumption of placing lamellas of a lower grading class within the inner layers of the beam, they are also used in the beam's outer layers.

1.5 Outlook

Our work clearly has some limitations. Despite this we believe that this research provides a basis for optimization algorithms for GTL beams allowing for further studies on extensions and variations like the following:

- Throughout this paper the structural system of a four-point bending test was examined. The advantage of this system is its simplicity and predictability due to the symmetry of loads and geometry. Nevertheless, the implementation of an FE model allows complex structural systems to be solved as well, like:
  - Continuous beams where the highest stresses appear at multiple locations along the beam's longitudinal axis,
  - constructions with holes or girder notches and
  - spatial structures.

- The optimization schemes used in this paper are currently only capable of dealing with wooden boards of equal length and beams consisting of one lamella per beam layer. In order to further optimize the load-bearing behavior an extension towards allowing multiple boards per layer, connected by finger joints, is conceivable. Here, the location of the finger joints could be subject to the optimization as well, meaning the algorithm would be capable of cutting boards and removing knot groups to further improve the final structural system.

- Beside changes in the definition of the optimization task, the used optimization schemes could be enhanced as follows:
  - Combining metaheuristic algorithms. A common approach is to combine local search algorithms with genetic algorithms. Such combinations are referred to as memetic algorithms [93]. By combination of such algorithms it is possible to take advantage of the special capabilities of each algorithm. Within memetic algorithms the task of maintaining the overall scope of the search space is subject to the genetic algorithm and the refinement of single solutions is subject to the local search.
  - Using advanced versions of genetic algorithms like steady-state genetic algorithms.
  - Implementing parallel genetic algorithms. For example by using the so-called island model [138], to reduce the computation time.

- Improving the metamodel for better predictions of deflections from the FE model and for minimizing the time needed for retraining of the model after a change of input data. Herein methods from the field of machine learning like
  - support vector machines and
  - artificial neural networks

could be applied. Especially artificial neural networks using deep learning prove to be applicable to a variety of different machine learning tasks, including regression.

Publication 2

A robust multisurface return-mapping algorithm and its implementation in Abaqus

Abstract

The simulation of complex material failure processes requires a precise differentiation of the involved failure mechanisms like fracture or plasticity. This is commonly achieved by using a so-called multisurface failure criterion, where each failure surface is related to a certain failure mechanism. In the case of plasticity, failure surfaces define the elastic domain of the material and any stress state outside of this domain is considered non-admissible and must be returned to the boundary of the elastic domain. So-called return-mapping algorithms are often used and well-studied methods for finding such valid stress states. However, their implementation in numerical simulation tools is often not robust and efficient enough for complex problems that involve sophisticated multisurface definitions. In this work, we present a multisurface return-mapping algorithm and its implementation in the finite element software Abaqus. We found that with additional and enhanced iterative solver methods, the classic Newton-Raphson-based implementation of the algorithm can be improved in order to find solutions to otherwise not returnable stress states. The added computational burden is minimal, as more stress states can be returned without reducing the size of the load increments. The paper focuses on the implementation aspects of such problems and offers the reader a thorough guide and the source code for an Abaqus implementation. We applied the algorithm to simulate the highly orthotropic behavior of wood, allowing us to predict plastic failure of various wooden structures and components.

2.1 Introduction

Compared to single failure surface models, multisurface failure criteria allow a more precise description of complex failure processes, characterized by different failure mechanisms. However, robust and efficient implementations of the necessary return-mapping algorithms for multiple plastic failure surfaces in numerical simulation tools are sometimes missing. Thus, in this work we present a robust multisurface return-mapping algorithm and its implementation in the commercial finite element software Abaqus.

One of the materials for which such a multisurface failure criterion is very useful is wood. As the material behavior is highly orthotropic and, thus, failure strongly varies with the load angle with respect to the wood fiber, very complex failure mechanisms can be observed. A proper formulation of such a failure criterion is crucial to ensure the future competitiveness of wood and wood-based materials. As recent years have shown, sustainable building materials are becoming increasingly important and must therefore be researched more extensively.

In comparison to smooth single surface failure criteria, a multisurface criterion defines the admissible region based on multiple intersecting smooth surfaces. This imposes an additional level of complexity to the problem: The intersections are non-smooth and therefore the differentiability is not guaranteed for all stress states. Furthermore, it is often difficult to fulfill the Kuhn-Tucker conditions for all yield functions (see Section 2.2.1). Those conditions impose constraints on the yield function and the slip rate, such that the plastic strain evolves only on the boundary of the elastic domain and in the direction of the applied stress. Therefore, they assure physical validity of the plastic evolution.

This problem has been the subject of numerous research papers in recent decades, which has led to various methods of a general but also domain-specific nature. One of the first, the so-called radial return method, was proposed by Wilkins [140] and served as a basis for subsequent research in that field. Simo and Hughes [123] and Simo et al. [124] introduced a generalization of the radial return method in form of an implicit backward Euler scheme, also including an extension to multiple yield functions. In contrast to their single surface method, however, the implementation of this multisurface criterion is not straightforward and requires an iterative procedure to solve the Kuhn-Tucker conditions. Still, this method is commonly used and has been further developed to improve its robustness, e.g., in Adhikary et al. [4]. Recently, du Bos et al. [39] also applied more general algorithms using artifical neural networks and Akpama et al. [5] applied the so-called ultimate scheme which proves to be robust and efficient for crystal plasticity.

In contrast to the general solution approaches, specific methods as in Clausen et al. [26], Fang et al. [45], Karaoulanis [71], and Meng et al. [87] (the latter work also contains an extensive historic overview of developed algorithms) are tailored to take into account isotropic material behavior and that the yield function is defined in terms of principal stresses only. Such methods allow the usage of simpler three-dimensional geometric solution approaches and highly efficient algorithms for predicting active yield functions.

As mentioned, the main difficulty arising from using a multisurface criterion is the non-smooth intersection of surfaces. Besides application of an iterative procedure, the methods outlined in [139] and [3] allow eliminating this singularity by fitting a new yield surface. Consequently, the admissible region can be described by a smooth, differentiable yield function.

The focus of this paper is on general return-mapping methods using yield functions following the form of the failure criterion of Tsai and Wu [133]. For wood such a criterium was derived in form of a two-step homogenization method. In [83] the material is at first modeled on the wood cell level, incorporating the strength of cellulose microfibrils and lignin. The constructed cell is then subjected to 800 pseudo random load cases, resulting in a set of failure modes and respective failure stresses. This process is carried out for the two kinds of wood found in coniferous species, namely early- and latewood, which form the generally

known pattern of annual rings. On the annual ring level, as described in [85], the second homogenization procedure is carried out, following the same principle as above. The model consists of multiple layers of early- and latewood having the previously determined properties. Again, 1000 pseudo random load combinations are applied, giving access to ductile and brittle failure modes and subsequently the failure surfaces on the so-called clear-wood level (i.e., wood without knots, defects or fiber deviations), which are used in this work and in our group's research ([49, 50, 78]). A similar model for simulation of spruce was proposed by Schmidt and Kaliske [120], however, no discussion of the algorithm's robustness is provided.

The derived failure surfaces are only used in Section 2.3, leaving the remaining paper in general terms and allowing consideration of arbitrary yield functions. Section 2.2 gives an overview of the return-mapping method by Simo and Hughes [123] and shows the enhancements necessary to make the algorithm more robust. Subsequently, in Section 2.3, three different strain states are examined, for which finding a solution is not possible by means of the method proposed by Simo and Hughes [123]. For each assessed stress state, the cause of failure is discussed and a solution finding method is presented. The paper closes with a discussion of further enhancements and applications of the described algorithm.

2.2 Material and methods

The description of the implemented algorithm starts in Section 2.2.1 with an overview of the return-mapping method by Simo and Hughes [123] and a discussion of common solution approaches for dealing with non-smooth intersections of multiple failure surfaces. Thereafter, in Section 2.2.2, the implementation of a general return-mapping algorithm in Abaqus, as so-called user material subroutine, is presented. The section gives a clear overview of the sequence of operations required for such an algorithm. Details on the subroutine design and the code structure are given in Section 2.2.3, providing the reader with an overview of the codebase to allow for future customization.

2.2.1 General return-mapping algorithm

The implemented return-mapping algorithm is based on an additive decomposition of the total strain into an elastic part and a plastic part. The solution for a single strain increment $\Delta\boldsymbol{\varepsilon}_n = \boldsymbol{\varepsilon}_{n+1} - \boldsymbol{\varepsilon}_n$ is obtained by "freezing" the plastic flow during an iteration step k, such that the trial state is fully determined by the plastic strain $\boldsymbol{\varepsilon}_{n+1}^{p^{(k)}}$, the consistency parameter $\Delta\gamma^{\alpha^{(k)}}$ and the working set of active constraints $\mathcal{J}_{\text{act}}^{(k)} \subseteq \mathcal{J} = \{\alpha \in \{1, 2, \ldots, m\}\}$, where m is the total number of yield functions, leading to

$$\boldsymbol{\sigma}_{n+1}^{(k)} = \mathcal{C} : \left(\boldsymbol{\varepsilon}_{n+1} - \boldsymbol{\varepsilon}_{n+1}^{p^{(k)}}\right) \text{ and} \tag{2.1}$$

$$\boldsymbol{R}_{n+1}^{(k)} = -\boldsymbol{\varepsilon}_{n+1}^{p^{(k)}} + \boldsymbol{\varepsilon}_n^p + \sum_{\alpha \in \mathcal{J}_{\text{act}}^{(k)}} \Delta\gamma^{\alpha^{(k)}} \partial_{\boldsymbol{\sigma}} f_{\alpha, n+1}^{(k)}, \tag{2.2}$$

where $\mathcal{C}$ is the fourth-order stiffness tensor, $\boldsymbol{R}_{n+1}^{(k)}$ is the plastic flow residual and $f_{\alpha, n+1}^{(k)}$ is the yield function corresponding to Surface α evaluated at $\boldsymbol{\sigma}_{n+1}^{(k)}$. f_α must be a smooth function that defines a convex admissible set $\{\boldsymbol{x} \in \mathbb{R} \,|\, f_\alpha(\boldsymbol{x}) \leq 0\}$ (see Section 2.2.2 for the formulation used in this work).

Equations (2.1) and (2.2) are based on the assumption of constant stiffness and associated plasticity, respectively. A feasible solution to the problem minimizes Equation (2.2) given the constraints

$$f_\alpha\left(\boldsymbol{\sigma}_{n+1}^{(k)}\right) < \epsilon_1 \quad \forall\alpha \in \mathcal{J}_{\text{act}}^{(k)} \text{ and} \tag{2.3}$$

$$\Delta\gamma^{\alpha^{(k)}} \geq 0 \quad \forall\alpha \in \mathcal{J}_{\text{act}}^{(k)}, \tag{2.4}$$

where ϵ_1 is positive and close to 0.

With this definition, the resulting stress state on the boundary of the yield function constrained domain and the plastic deformations can be found by iteratively updating the state variables using the Newton-Raphson procedure outlined in [123]. The main difficulty involved in finding a feasible solution is that the final set of active constraints is not known in advance. As opposed to single surface return-mapping, a violation of multiple yield functions for the trial stress state does not automatically imply Equation (2.4) for all yield functions for the returned stress state.

Simo and Hughes [123] outline two approaches for dealing with changes in $\mathcal{J}_{\mathrm{act}}^{(k)}$:

1. Defer checking the consistency parameter constraint (Equation (2.4)) until the Newton-Raphson procedure converges. After convergence, drop the yield functions that violate Equation (2.4) and restart the algorithm with a new set of active constraints. (This method will further be referred to as the *exact* method.)

2. Check the consistency parameter constraint (Equation (2.4)) in every Newton-Raphson iteration. On violation, immediately drop the constraint and restart the iteration with a new set of active constraints. (This method will further be referred to as the *optimized* method.)

In addition, Adhikary et al. [4] describe a third method that is capable of finding solutions to the multisurface problem for active constraint combinations for which approaches (1) and (2) do not converge:

3. Consider $\mathcal{J}_{\mathrm{act}}^{(k)}$ to be a state variable having $2^m - 2$ possible states, which are the number of possible combinations of active constraints, excluding the two cases for all active and all inactive. All constraints active can be excluded, as it is also checked by the initial run of the *exact* method. For each of the possible combinations, perform the *exact* method until a combination of yield functions solves the problem. (This method will further be referred to as the *brute force* method.)

The *exact* method described above only accounts for active constraints becoming inactive. However, for certain initial values, as will be shown in Section 2.3, it is necessary to add some of the deactivated constraints back to the active set. Therefore, the implementation presented in this work additionally *reactivates* the constraints

$$\left\{ \alpha \in \mathcal{J} \setminus \mathcal{J}_{\mathrm{act}}^{(k)} \mid f_\alpha \left(\boldsymbol{\sigma}_{n+1}^{(k)} \right) > 0 \right\}. \tag{2.5}$$

For the *optimized* and the *exact* method the state variables are initialized (i.e., $k = 0$) as follows:

$$\boldsymbol{\varepsilon}_{n+1}^{p^{(0)}} = \boldsymbol{\varepsilon}_n^p \tag{2.6}$$

$$\boldsymbol{\sigma}_{n+1}^{\mathrm{trial}} := \boldsymbol{\sigma}_{n+1}^{(0)} = \mathcal{C} : \left(\boldsymbol{\varepsilon}_{n+1} - \boldsymbol{\varepsilon}_n^p \right) \tag{2.7}$$

$$\mathcal{J}_{\mathrm{act}}^{(0)} = \left\{ \alpha \in \{1, 2, \ldots, m\} \mid f_\alpha \left(\boldsymbol{\sigma}_{n+1}^{\mathrm{trial}} \right) > 0 \right\} \tag{2.8}$$

$$\Delta \gamma^{\alpha^{(k)}} = 0 \tag{2.9}$$

In case of the *brute force* method,

$$\mathcal{J}_{\mathrm{act}}^{(k)} = \pi \left(i \right) \quad \forall k \tag{2.10}$$

with $\pi \left(i \right)$ being the i-th combination of active constraints from $\mathcal{J}$. The order of active constraints is selected such that $\left| \pi \left(i \right) \right| \geq \left| \pi \left(i + 1 \right) \right|$.

2.2.2 Algorithmic implementation of the return-mapping method

The present implementation is based on the quadratic form of the failure criterion of Tsai and Wu [133]

$$f(\boldsymbol{\sigma}) = a_{gh}\sigma_{gh} + b_{ghij}\sigma_{gh}\sigma_{ij} - 1 \le 0, \tag{2.11}$$

with the first and second order partial derivative with respect to the stress field

$$[\partial_{\boldsymbol{\sigma}} f(\boldsymbol{\sigma})]_{gh} = a_{gh} + 2b_{ghij}\sigma_{gh} \quad \text{and} \tag{2.12}$$

$$[\partial_{\boldsymbol{\sigma}\boldsymbol{\sigma}} f(\boldsymbol{\sigma})]_{ghij} = 2b_{ghij}. \tag{2.13}$$

The tensor components are symmetric, i.e., $b_{ghij} = b_{ijgh}$, and, in order for the failure criterion to be closed and convex, constrained by the condition

$$b_{ghgh}b_{ijij} - b_{ghij}^2 \ge 0. \tag{2.14}$$

The values of the components are derived using the two-step homogenization method described at the end of Section 3.1. The surfaces defining the entire failure criterion are divided into two groups: plastic and crack initiation surfaces. The solution method described in Section 2.2.1 is used to handle plastic processes only. Thus, the decision process, outlined in Figure 2.1, is required to handle the distinction between cracking or plastic failure for each integration point of the finite element model. With this work's scope being on the return-mapping part of the algorithm, cracking mechanisms are not discussed. Details on the extension for handling non-plastic behavior are presented in [85].

The distinction of failure processes is based on whether the innermost surface, with respect to the elastic predictor stress, belongs to the group of plastic or crack initiation surfaces. This is determined by substitution of the trial stress state $\boldsymbol{\sigma}_{n+1}^{\text{trial}}$ in the yield function formulation in Equation (2.11) with $\lambda \boldsymbol{\sigma}_{n+1}^{\text{trial}}$ where λ is some scalar value. Subsequently,

$$f_{\alpha}(\lambda \boldsymbol{\sigma}_{n+1}^{\text{trial}}) = 0 \tag{2.15}$$

is solved for λ for all $\alpha \in \mathcal{J}_{\text{act}}^{(0)}$. As the Tsai-Wu criterion is convex and with zero stress being always feasible, the surface with the smallest positive value for λ is the innermost one and indicates the type of failure process. In case of a plastic failure process all crack initiation surfaces are now excluded from the active set of constraints. Otherwise, a crack is initiated (see [85]) or in case that no failure surface is active, a linear elastic step is performed and the resulting stress $\boldsymbol{\sigma}_{n+1}^{\text{trial}}$ and tangent moduli $\mathcal{C}$ are returned to Abaqus.

For the above mentioned case of a plastic failure process, the return-mapping procedure is carried out with the remaining surfaces, applying the three different methods described in Section 2.2.1 in the following sequence, until a solution is found: The *optimized* method (most efficient), the *exact* method and as a safe backup the *brute force* method. As soon as a feasible set of state variables is found, the algorithmic elastoplastic tangent moduli $\frac{d\boldsymbol{\sigma}}{d\boldsymbol{\varepsilon}}$ are computed, following the procedure outlined by Simo and Hughes [123]. This allows for faster convergence of the non-linear finite element problem. As quite often observed e.g., in [118], the multisurface return-mapping algorithm is sensitive to the strain increment size and fails if the trial stresses are too large. Therefore, the procedure uses the adaptive load incrementation scheme implemented in Abaqus (see Section 2.2.3) and forces an increment reduction on failure, meaning that the non-converged increment is repeated with a smaller load increment and therefore also with smaller trial stresses.
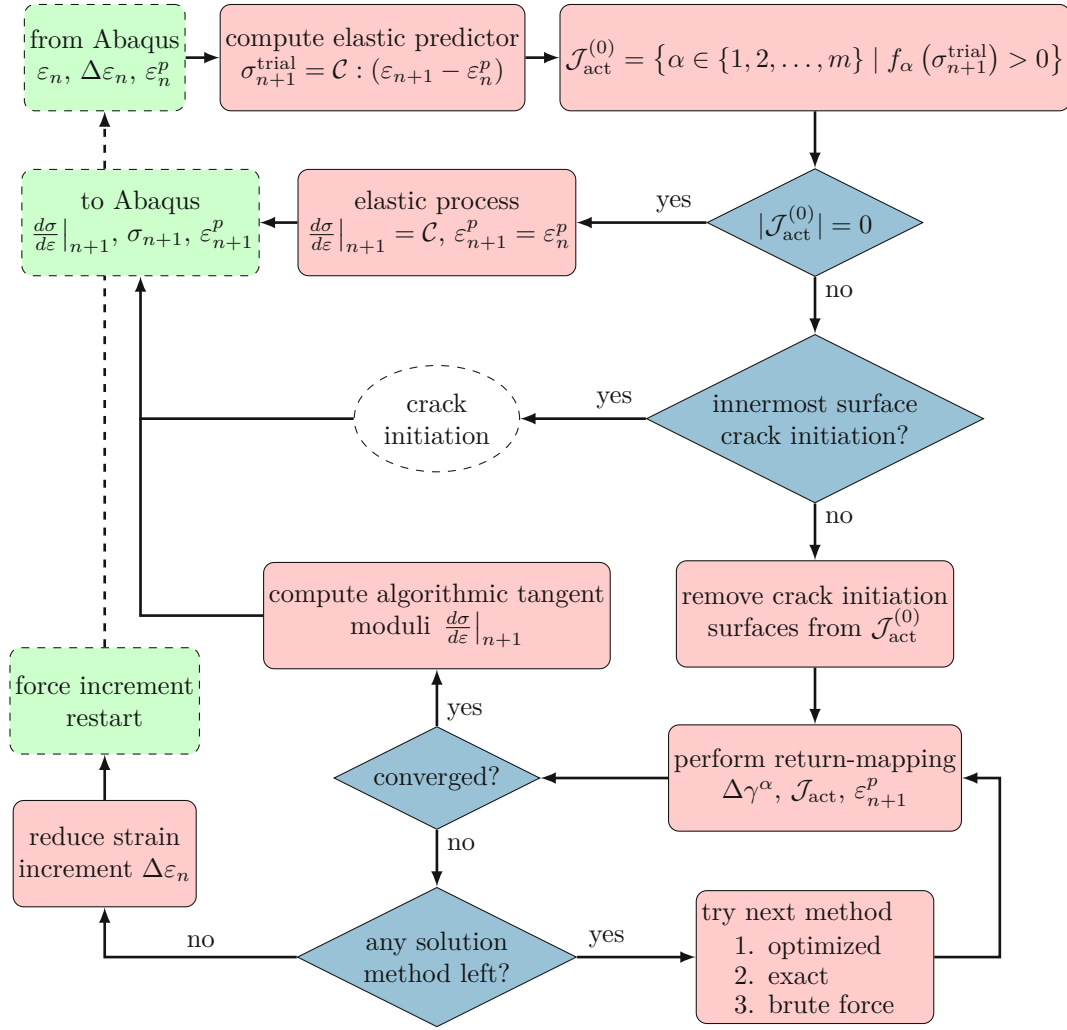
Fig. 2.1: Conceptional level flowchart visualizing the main aspects of the user material subroutine. The crack initiation is not covered in this work.

Another often neglected aspect when implementing multisurface return-mapping algorithms is the linear dependence of the flow vectors. With the solution being constructed by linear combination of six-dimensional vectors (for a three-dimensional problem) inevitably linear dependency of those vectors occurs if more than six surfaces are contained in the active set of constraints. However, as discussed by Adhikary et al. [4], there are also cases where this happens for less than seven vectors. As possible solution they proposed to eliminate the constraints with the smallest

$$d_\alpha = \frac{f_\alpha(\boldsymbol{\sigma})}{|\partial_{\boldsymbol{\sigma}} f_\alpha(\boldsymbol{\sigma})|}, \tag{2.16}$$

in order to keep the surfaces that are "most violated". A small value of d_α means that only a small change in $\boldsymbol{\sigma}$ is required to get back to the boundary of the elastic domain. The denominator occurs in Equation (2.16) to consider the steepness of the gradient in this region. A very steep gradient means that even a small change in $\boldsymbol{\sigma}$ results in a considerably large change in f_α. Thus, yield functions with a steep gradient need smaller changes in $\boldsymbol{\sigma}$ and can be considered "less violated".

Whether a set of flow vectors is considered linearly dependent is computed by performing a singular value decomposition of the active set's vectors. If the smallest singular value is smaller than $1\mathrm{E}{-}5$ times the largest value, the linear system of equations is considered to be singular and the set of flow vectors is linearly dependent. Subsequently, constraints are dropped for a single Newton-Raphson iteration, according to the procedure outlined above, and are added back to the set for evaluation with the newly computed state variables.

2.2.3 General return-mapping implementation in Abaqus

The following section provides a brief overview of the implementation in Abaqus with user subroutines. The code is entirely written in Fortran ≥ 90 and is made available at `https://gitlab.imws.tuwien.ac.at/e202-02/multisurface-plasticity`. The purpose of this section is to give readers an insight into the codebase and provide them with the necessary information to adapt parts of the code. As the presented algorithm consists of nested iterative solvers, the term "outer iteration step" refers to iteration steps done by Abaqus for solving the non-linear displacement problem, whereas "iteration step" refers to the steps done in the return-mapping algorithm.

The main entry point for Abaqus is the user material subroutine (`src/umat.f90`). It is called in each outer iteration step for each integration point and defines the mechanical behavior of the material. Within the subroutine, at first the material properties `PROPS` (provided in the input file) and the last increment's state variables `STATEV` are converted into the user defined types shown in Figure 2.2 using the `AbaqusDataInterface` module (`src/AbaqusDataInterface.f90`). This module is the only point for reading from and writing to the Abaqus data arrays `PROPS`, `STATEV` and `UVARM`.
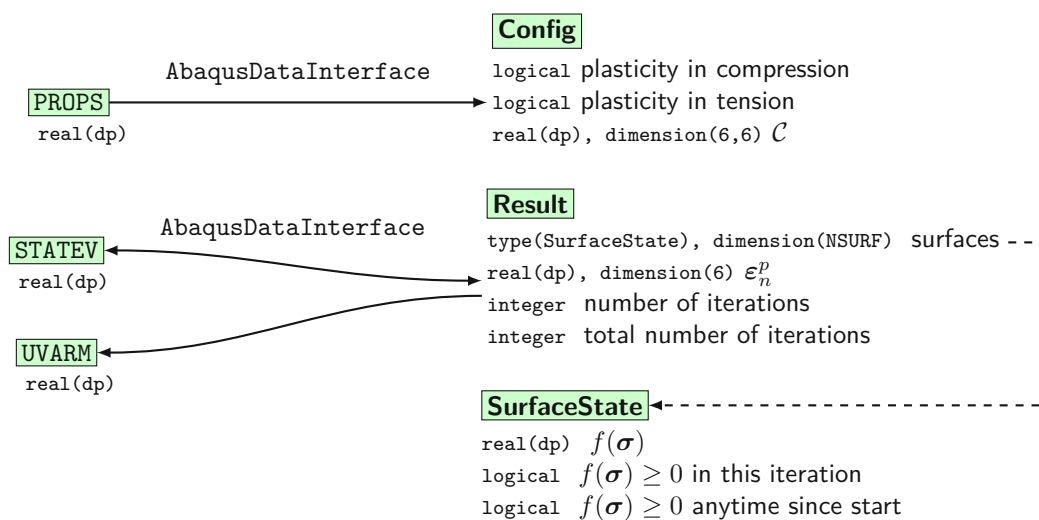
Fig. 2.2: Mapping of Abaqus data arrays to the user defined types. The input and output from and to the data arrays is only performed through the module `AbaqusDataInterface`.

After this initialization step, the actual return-mapping subroutine `returnmapping` is called, starting with the *optimized* method (`src/MultisurfacePlasticity.f90`). The subroutine computes the tangential moduli `DDSDDE`, the resulting stress `STRESS`, the plastic strains `res%plastic_strain` and notifies the user material subroutine of the convergence status. On failure the `returnmapping` subroutine is called with the next available solution finding method, following the procedure outlined in Figure 2.1. If none are left, the user material subroutine takes care of forcing the increment reduction by setting the variable `PNEWDT` accordingly. Finally the `STATEV` array is updated with this increment's state variables.

Most routines and functions used in the main return-mapping algorithm, e.g., deactivating linearly dependent constraints or computing all possible variations of active constraints, are defined in `src/ReturnmappingProcedures.f90`. Every routine associated with the failure criteria, e.g., finding the innermost surface or the actual yield function and its derivatives, is defined in `src/TsaiWu.f90`. The parameters for the Tsai-Wu surfaces are defined in `data/tsaiwu_data.f90`.

For easier adaption of input parameters, basic variables are defined in a separate module named `shared` (`src/shared.f90`). It contains definitions for thresholds, switches for experimental features and the number of surfaces considered. This number must match the surface definition in `data/tsaiwu_data.f90`. The Tsai-Wu data array is structured such that the first `NSURF_plastic` entries are plastic surfaces and the next `NSURF_crack` entries are crack initiation surfaces.

Besides the user material subroutine, a user output routine (`src/uvarm.f90`) is used for adding information about violated constraints to the output file. Depending on the number of user output variables n (defined in the input file), a maximum of n active yield functions is inserted into `UVARM` (e.g., if $n = 3$ and yield functions 2 and 3 are active, then `UVARM` $= (2, 3, 0)$). If multiple constraints are active, the order matches the defining order in the Tsai-Wu data file.

The codebase also includes a set of unit and functional tests that can be executed by compiling and running `test/runtest.f90`. The tests include

- validations of each function and subroutine,

- return-mapping examples and

- a numerical validation of the tangential moduli.

2.3 Numerical examples

In order to show the performance of the proposed algorithm compared to the original multisurface return-mapping algorithm (i.e., the *optimized* method) outlined in Section 2.2.2, three selected initial strain states, listed in Table 2.1, are considered in the following. The strains are given in Voigt notation such that $\bullet = (\bullet_{11}, \bullet_{22}, \bullet_{33}, \bullet_{12}, \bullet_{13}, \bullet_{23})$ and two different orthotropic stiffness tensors, describing a wood-like material, were used:

$$
\mathcal{C}_A = \begin{bmatrix} 13515.4 & 313.2 & 249.4 & 0.0 & 0.0 & 0.0 \\ & 974.6 & 433.5 & 0.0 & 0.0 & 0.0 \\ & & 659.7 & 0.0 & 0.0 & 0.0 \\ & & & 332.3 & 0.0 & 0.0 \\ & \text{sym.} & & & 338.5 & 0.0 \\ & & & & & 50.8 \end{bmatrix} \text{MPa} \quad \text{and} \tag{2.17}
$$

$$
\mathcal{C}_B = \begin{bmatrix} 11884.0 & 2053.3 & 1624.1 & 0.0 & 0.0 & 0.0 \\ & 2577.0 & 1613.9 & 0.0 & 0.0 & 0.0 \\ & & 1472.0 & 0.0 & 0.0 & 0.0 \\ & & & 600.0 & 0.0 & 0.0 \\ & \text{sym.} & & & 650.0 & 0.0 \\ & & & & & 40.0 \end{bmatrix} \text{MPa}. \tag{2.18}
$$

States 1 and 2 were tested using $\mathcal{C}_A$ and State 3 using $\mathcal{C}_B$. In all three cases the Tsai-Wu failure criteria definitions shown in Table 2.2 were used.

Tab. 2.1: Initial values used for the state variables as input to the return-mapping algorithm. All three states lead to no solution when the original (*optimized*) method is applied. The strains are given in Voigt notation in the following order: $\bullet = (\bullet_{11}, \bullet_{22}, \bullet_{33}, \bullet_{12}, \bullet_{13}, \bullet_{23})$.

State 1	ε_n	$-2.041\text{E}{-}3$	$1.780\text{E}{-}3$	$-5.466\text{E}{-}3$	$-6.603\text{E}{-}5$	$1.022\text{E}{-}2$	$2.774\text{E}{-}4$
	$\Delta\varepsilon_n$	$-1.250\text{E}{-}3$	$1.271\text{E}{-}3$	$-7.663\text{E}{-}3$	$-1.118\text{E}{-}4$	$7.654\text{E}{-}3$	$2.877\text{E}{-}4$
	ε_n^p	$-3.385\text{E}{-}4$	$-9.288\text{E}{-}5$	$-2.751\text{E}{-}3$	$-2.002\text{E}{-}5$	$2.339\text{E}{-}3$	$3.609\text{E}{-}5$
State 2	ε_n	0.000	0.000	0.000	0.000	0.000	0.000
	$\Delta\varepsilon_n$	$-1.000\text{E}{-}2$	0.000	0.000	0.000	0.000	0.000
	ε_n^p	0.000	0.000	0.000	0.000	0.000	0.000
State 3	ε_n	$-6.219\text{E}{-}7$	$1.992\text{E}{-}6$	$-1.557\text{E}{-}6$	$-2.060\text{E}{-}7$	$-8.534\text{E}{-}8$	$2.508\text{E}{-}5$
	$\Delta\varepsilon_n$	$2.942\text{E}{-}3$	$1.916\text{E}{-}3$	$-2.983\text{E}{-}3$	$-1.827\text{E}{-}2$	$4.290\text{E}{-}2$	$-7.382\text{E}{-}2$
	ε_n^p	$1.525\text{E}{-}4$	$9.305\text{E}{-}4$	$1.730\text{E}{-}4$	$-9.760\text{E}{-}3$	$2.131\text{E}{-}2$	$-1.854\text{E}{-}2$

Tab. 2.2: Tsai-Wu tensor components of the plastic failure surfaces. The units for $a_{gg,\alpha}$ and $b_{ghij,\alpha}$ are MPa^{-1} and MPa^{-2}, respectively.

Surface f_α	1	2	3	4
$a_{11,\alpha}$	$-3.572\text{E}{-}3$	$-8.756\text{E}{-}3$	$2.932\text{E}{-}4$	$-2.167\text{E}{-}2$
$a_{22,\alpha}$	$4.885\text{E}{-}2$	$-3.995\text{E}{-}2$	$-1.561\text{E}{-}2$	$-9.091\text{E}{-}3$
$a_{33,\alpha}$	$-3.485\text{E}{-}1$	$3.183\text{E}{-}1$	$-1.864\text{E}{-}1$	$-1.071\text{E}{-}1$
$b_{1111,\alpha}$	$1.301\text{E}{-}4$	$2.032\text{E}{-}4$	$1.055\text{E}{-}4$	$8.333\text{E}{-}5$
$b_{2222,\alpha}$	$8.903\text{E}{-}3$	$1.897\text{E}{-}2$	$1.591\text{E}{-}2$	$9.091\text{E}{-}3$
$b_{3333,\alpha}$	$2.993\text{E}{-}3$	$9.660\text{E}{-}6$	$5.172\text{E}{-}3$	$3.571\text{E}{-}2$
$b_{2233,\alpha}$	$2.070\text{E}{-}5$	$-1.978\text{E}{-}6$	$2.352\text{E}{-}4$	0.000
$b_{1212,\alpha}$	$1.235\text{E}{-}2$	$1.235\text{E}{-}2$	$1.235\text{E}{-}2$	$1.235\text{E}{-}2$
$b_{2323,\alpha}$	$2.778\text{E}{-}2$	$2.778\text{E}{-}2$	$2.778\text{E}{-}2$	$2.778\text{E}{-}2$
$b_{3131,\alpha}$	$8.264\text{E}{-}3$	$8.264\text{E}{-}3$	$8.264\text{E}{-}3$	$8.264\text{E}{-}3$

State 1

Figure 2.3 shows an intermediate result of the *optimized* method and the final result of the *exact* method, obtained for the initial values of State 1. The plotted surfaces correspond to $f_\alpha(\boldsymbol{\sigma}) = 0$ (Equation (2.11)) shown in the σ_{11}-σ_{13} plane, with the remaining stress components being fixed for the stress at the end of the increment $\boldsymbol{\sigma}_{n+1}^{(k)}$. Additionally, the trial stress $\boldsymbol{\sigma}_{n+1}^{\text{trial}}$ and the flow vectors $\partial_{\boldsymbol{\sigma}} f_{\alpha,n+1}^{(k)}$ scaled by the consistency parameter $\Delta\gamma^{\alpha^{(k)}}$, colored to match the corresponding yield surface and mapped to the stress space using $\mathcal{C}$, are depicted. In case of convergence, not necessarily validity in terms of the consistency parameter, summation of the trial stress vector and the flow vectors must equal the stress at the end of the increment. Otherwise, the residual from Equation (2.2), also mapped to the stress space, remains.

Figure 2.3a shows an intermediate state of the Newton-Raphson iteration for the *optimized* method. The trial solution in this state contains invalid consistency parameters for Surfaces 3 and 4. In accordance to the algorithmic procedure of the *optimized* method, both surfaces are considered not to be part of the solution as they violate Equation (2.4) and the constraints are removed before proceeding to the next iteration. The negative consistency parameters can qualitatively be observed by the orientation of the flow vectors to their respective yield surface. In case of a negative consistency parameter they point *away* from the yield surface. Looking at Figure 2.3b it is obvious that Surface 4 should not have been removed as it is the actual solution for the given set of initial values.

From the intermediate state in Figure 2.3a the *exact* method continues the Newton-Raphson iteration until convergence. In the converged state, only the consistency parameter corresponding to Surface 3 is negative, thus Surface 4 remains as part of the solution and the return-mapping procedure is restarted
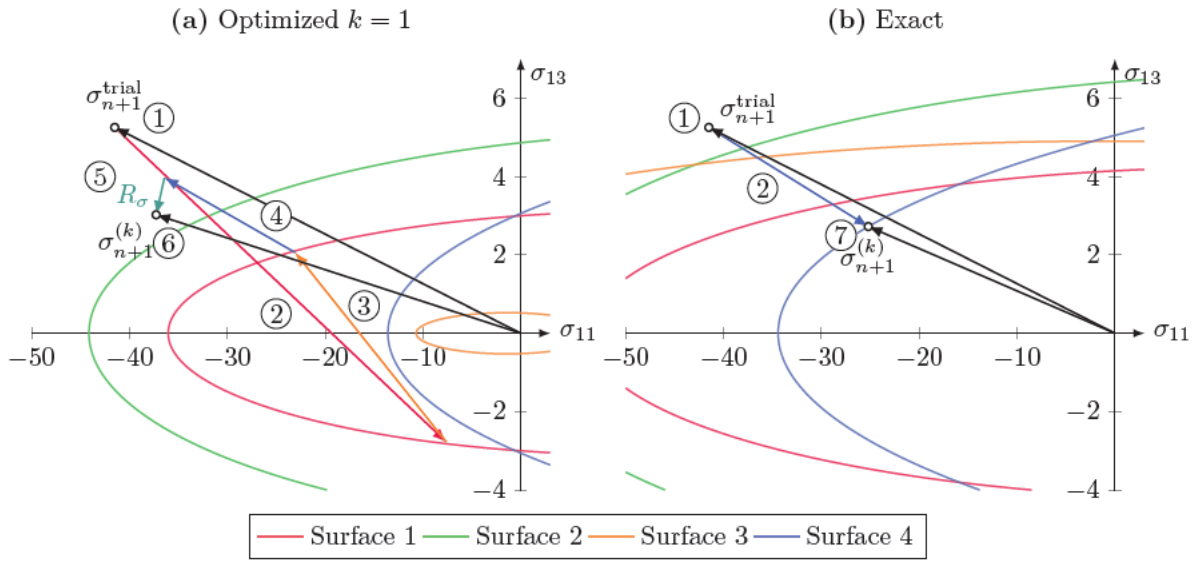
(a) Optimized $k = 1$

(b) Exact

Surface 1 — Surface 2 — Surface 3 — Surface 4

Fig. 2.3: Intermediate result of the *optimized* and final result of the *exact* method for the initial values of State 1. Stresses (in MPa) and surfaces are brought from six-dimensional stress space into a two-dimensional space by projection onto or cutting with the σ_{11}-σ_{13} plane through $\sigma_{n+1}^{(k)}$, respectively. The solution can then be graphically depicted by bringing Equation (2.2) into stress space using the stiffness tensor $\mathcal{C}$ and projecting it onto the σ_{11}-σ_{13}-plane. First, the trial stress vector from the origin to $\boldsymbol{\sigma}_{n+1}^{\text{trial}}$ is added ①. Then, the flow vectors of the active yield function are added, i.e., the summation in Equation (2.2) ②–④. For a converged configuration, the last added flow vector should now end at $\boldsymbol{\sigma}_{n+1}^{(k)}$ ⑦ which must lie on the boundary of the elastic domain. Otherwise, the residual ⑤ remains as difference between the last flow vector ④ and the current stress ⑥. As this state is not converged, stress ⑥ lies outside of the elastic domain. The state shown in (a) leads to exclusion of Surface 4, while (b) shows that Surface 4 is actually the one needed for solving State 1.

now excluding Surface 3. Subsequently, two additional restarts, with adapted sets of active constraints, are needed to arrive at the solution. This is also depicted in Figure 2.4, where the actual steps needed for reaching a converged state are shown. The main difference of the two approaches is observable in the number of iteration steps needed to reach the shown states. For the *optimized* method each shown step represents a single state of the Newton-Raphson iteration i.e., k is equal to the number of iteration steps needed. In the *exact* method, however, each shown step represent an already converged state, thus the residual is never contained and $\boldsymbol{\sigma}_{n+1}^{(k)}$ is always on the boundary of the elastic domain. As outlined above, the problem with the *optimized* method is, that Surface 4 is removed prematurely in Step (a) (shown with a dashed line after removal), while the actual converged state for this configuration (Step (d)) would not lead to a removal.

State 2

Figure 2.5 shows the comparison of the *exact* method without and with reactivating disabled constraints. In Figure 2.5a a converged state is depicted where Surfaces 1, 2 and 4 are part of the trial solution. Obviously, the solution violates the Kuhn-Tucker conditions, as the flow vectors of Surfaces 1 and 2 lead away from the yield surface, i.e., the consistency parameters are negative. Within the *exact* procedure both constraints are removed and the return-mapping algorithm is restarted only including Surfaces 3 and 4.

Without reactivating violated constraints the outlined procedure does not arrive at the correct solution, as Surface 2 remains violated for the converged state resulting from the linear combination of the flow
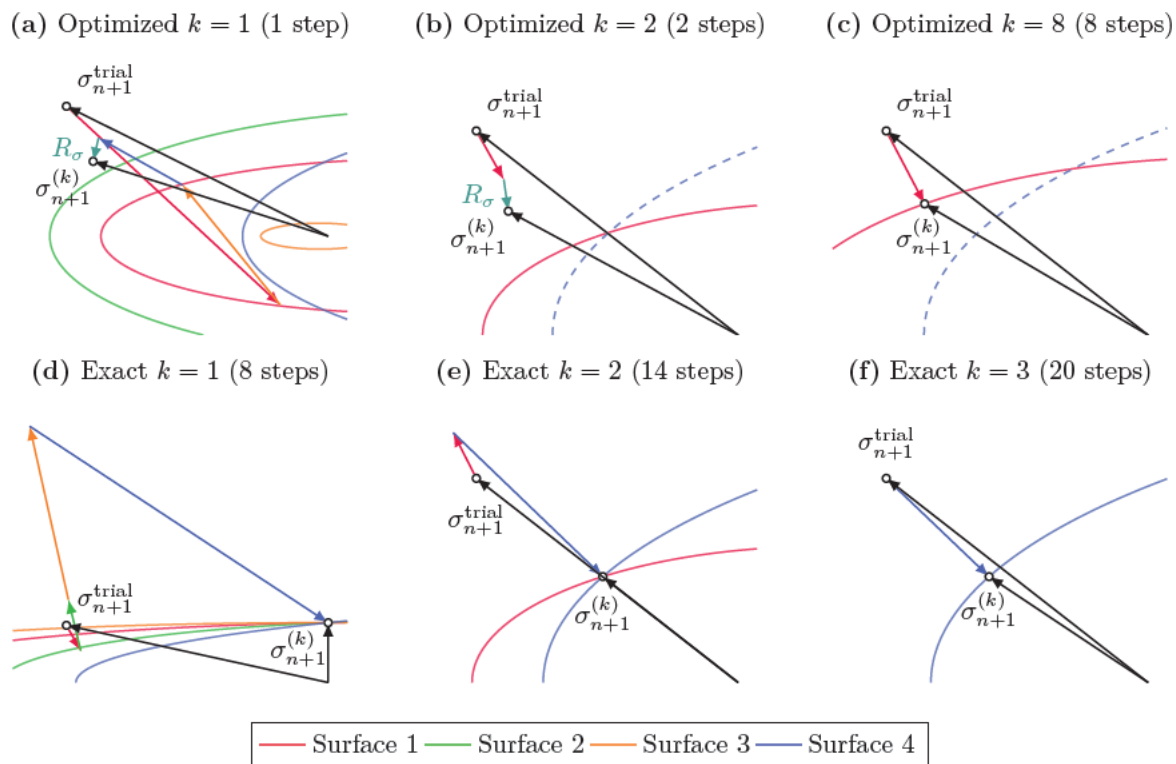
(a) Optimized $k = 1$ (1 step) **(b)** Optimized $k = 2$ (2 steps) **(c)** Optimized $k = 8$ (8 steps)

(d) Exact $k = 1$ (8 steps) **(e)** Exact $k = 2$ (14 steps) **(f)** Exact $k = 3$ (20 steps)

Surface 1 —— Surface 2 —— Surface 3 —— Surface 4

Fig. 2.4: Convergence course for the *optimized* (a–c) and the *exact* method (d–f). The states shown for the *exact* method are already converged results for the given set of active yield functions and the trial stress state $\sigma_{n+1}^{\text{trial}}$. Thus, each step k consists of multiple iteration steps, as shown in the parenthesis, and the residual is never depicted. The axis in the σ_{11}-σ_{13} plane are scaled differently, such that all flow vectors can be displayed. Equal points throughout the figure are $\sigma_{n+1}^{\text{trial}}$ and the origin. Yield surfaces contained in the active set of constraints are shown as solid lines and inactive, but violated yield surfaces as dashed lines. A comparison of (c) and (f) clearly shows that the correct solution for State 1 is only achieved using the *exact* method.

vectors of Surfaces 3 and 4. However, adding Surface 2 back at this state and restarting the return-mapping procedure leads to the feasible solution shown in Figure 2.5b. It should be noted, that the *brute force* method arrives at the same solution, however, performance-wise, adding the constraints back is faster.

State 3

Figure 2.6 shows the comparison of the *exact* method and the *brute force* method. As mentioned, in some special cases, even though surfaces can be reactivated, the *exact* method fails. For the given set of initial values, at some point, the *exact* method enters an infinite loop of the three different states (a), (b) and (c) shown in Figure 2.6. After convergence to state (a), the failure criterion corresponding to Surface 1 is violated and the consistency parameter for the flow vector of Surface 4 is negative. Therefore, following the *exact* method with reactivation of yield functions, constraint 4 is dropped and constraint 1 is reintroduced. The return-mapping is continued until the Newton-Raphson procedure converges to state (b). This trial solution fulfills the criteria for having no violated surface, but has two negative consistency parameters for Surfaces 1 and 2. Thus, they are both dropped upon restarting the return-mapping procedure resulting in Surface 3 being the only one considered for the next iteration. Finally, state (c) is reached which still violates constraints 4 and 2, where the latter does not have a solution for $f_\alpha(\boldsymbol{\sigma}) = 0$ in the σ_{22}-σ_{13} plane, meaning no matter the size of σ_{22} and σ_{13}, given the remaining stresses are fixed for $\sigma_{n+1}^{(k)}$, the constraint is always violated. Hence, constraints 2 and 4 are reintroduced, thus leading back to state (a). Figure 2.6 (d)
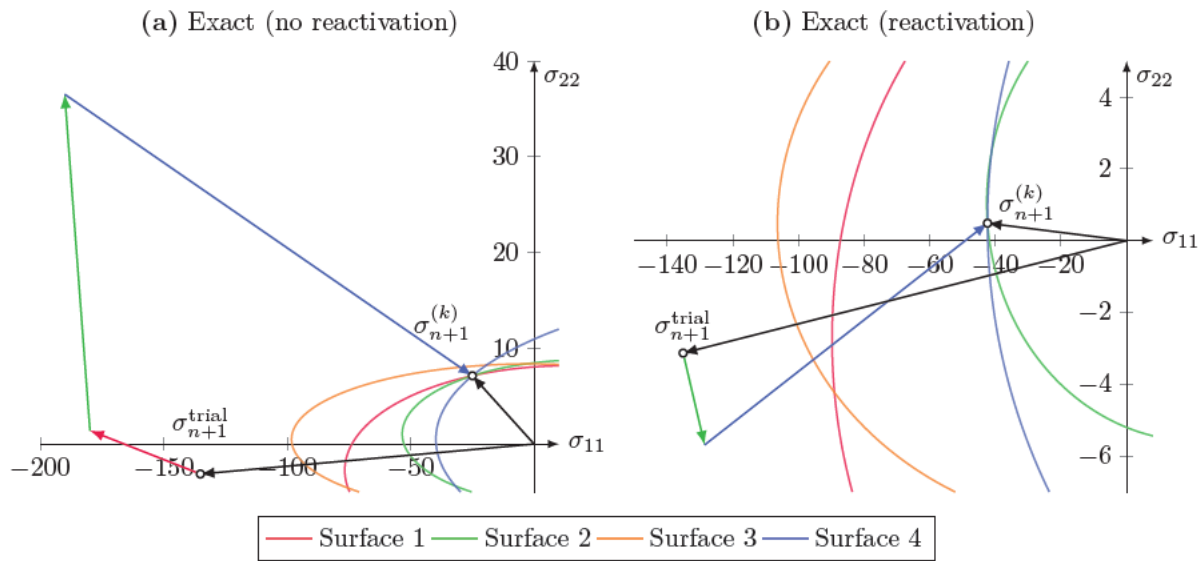
Fig. 2.5: Comparison of the *exact* method without and with reactivating disabled constraints for the initial values of State 2. The plot shows yield surfaces and flow vectors for the stress (in MPa) at the end of the increment $\boldsymbol{\sigma}_{n+1}^{(k)}$ in the σ_{11}-σ_{22} plane.

shows the feasible solution obtained by using the *brute force* method. The solution could only be reached by explicitly prescribing the set of active constraints considering Surfaces 2 and 3 exclusively.

2.4 Conclusions and outlook

A general multisurface return-mapping algorithm is proposed, making use of three different methods to find admissible stress states to arbitrary sets of initial values, which tend to cause problems in conventional implementations. To solve all three selected cases, all implemented methods had to be used, justifying the need for a robust implementation. Numerous real life applications of the implemented Abaqus subroutine showed that the computational burden of having to test three different solution methods is small compared to the overall effort of solving a non-linear finite element problem. Additionally, with increasing simulation time, most of the trial stress states tend to require solutions built from increasing numbers of linear combinations of surfaces. This is a result of stresses *moving* along the yield surface, until other yield functions at intersections are activated. The larger the number of surfaces and the stronger stresses tend towards intersections, the more often these extended solution methods have to be used.

A remaining issue is that during the return-mapping procedure the crack initiation surfaces are inactive. However, close to intersections of crack initiation and plastic surfaces the failure mechanism can change from plastic deformations to fracture. Therefore, in order to reduce the error, the strain increments should be kept at a reasonably small size. Nevertheless, the extensions to the basic return-mapping procedure significanlty improved the solvability of example calculations we performed and actually reduced the overall computational cost, as fewer reductions of the strain increments are necessary.

Further research should focus on an extension to allow consideration of hardening and proper handling of fracture processes. The first can be implemented rather easily, as the provided user subroutine mostly follows the algorithm proposed in Simo and Hughes [123] which already includes hardening and softening. For the second, with fracture in general and especially for complex materials like wood still being the topic of ongoing research, currently no stable, general and performant solution is available. Nevertheless, for less complex cases, Lukacevic et al. [85] outlines a possible approach.
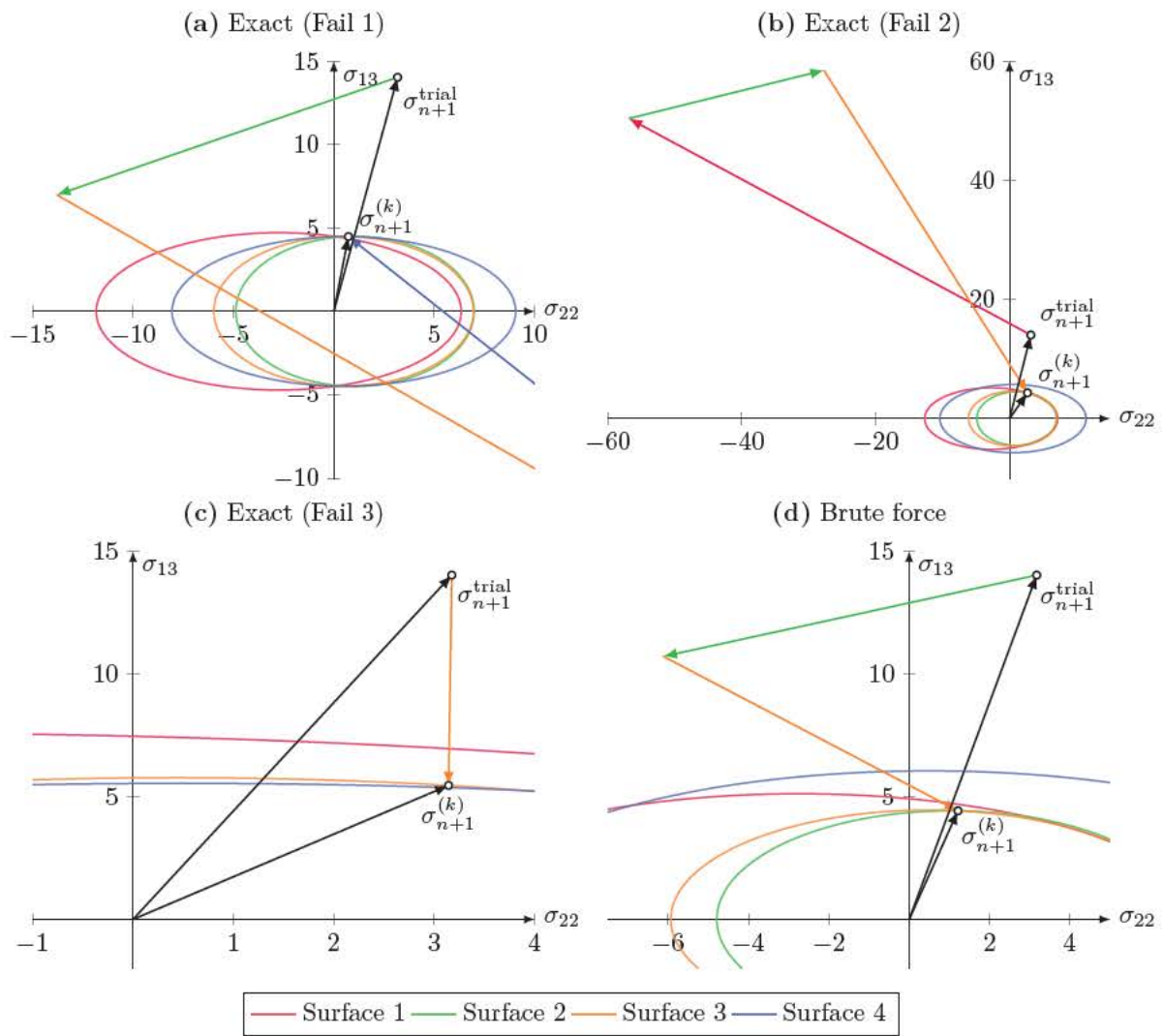
(a) Exact (Fail 1)

(b) Exact (Fail 2)

(c) Exact (Fail 3)

(d) Brute force

Surface 1 — Surface 2 — Surface 3 — Surface 4

Fig. 2.6: Comparison of the *exact* method and the *brute force* method for the initial values of State 3. The plot shows yield surfaces and flow vectors for the stress (in MPa) at the end of the increment $\sigma_{n+1}^{(k)}$ in the σ_{22}-σ_{13} plane.

Acknowledgement

Publication 3

A hybrid multi-phase field model to describe cohesive failure in orthotropic materials, assessed by modeling failure mechanisms in wood

Authors   Sebastian Pech, Markus Lukacevic, Josef Füssl

Under review at *Engineering Fracture Mechanics*

Abstract

Fracture mechanics is crucial for many fields of engineering applications, as precisely predicting failure of structures and parts is required for efficient designs. The simulation of failure processes is, both from a mechanical and a numerical point of view, challenging, especially for inhomogeneous materials, where the microstructure influences crack initiation and propagation and might lead to very complex crack patterns. The phase field method for fracture is a promising approach to encounter such materials, since it is able to describe complex fracture phenomena like crack kinking, branching and coalescence. Moreover, it is a largely mesh independent approach, given that the mesh is homogenous in the area of the crack. However, the original formulation of the phase field method is limited to isotropic materials and does not account for preferable fracture planes defined through the material's microstructure. In this work, the method is expanded to take orthotropic constitutive behavior and preferable directions of crack propagation into account. We show that by using a stress-based split and multiple phase field variables with preferable fracture planes, in combination with a hybrid phase field approach, a general framework can be found for simulating anisotropic, inhomogeneous materials. The stress-based split is based on fictitious crack faces and is, herein, expanded to support anisotropic materials. Furthermore, a novel hybrid approach is used, where the degradation of the sound material is performed based on a smooth traction free crack boundary condition, which proves to be the main driving factor for recovering commonly observed crack patterns. This is shown by means of a detailed analysis of two examples: a wooden single edge notched plate and a wood board with a single knot and complex fiber directions. In both cases, the proposed novel hybrid phase field approach is able to realistically reproduce complex failure modes.

3.1 Introduction

The use of fracture mechanical modeling approaches is crucial in areas of applied engineering. Being able to describe failure processes of structures and components realistically and allows for their optimization with regard to design and material consumption, while ensuring high reliability standards. Simulation of failure processes has been the topic of numerous publications over the recent decades and is, due the complexity of possible material failure mechanisms, still an area that is being researched very intensively.

The foundation of most studies on brittle fracture processes is the work of Griffith and Taylor [54], which describes fracture in terms of a critical fracture energy release rate required for crack propagation. Based on Griffith's work, Irwin [67] introduced the so-called stress intensity factors to characterize stress fields around the crack tip, depending on geometry and load. While those linear elastic fracture mechanics theories can be applied to describe crack propagation of existing cracks, effects like crack kinking, branching, coalescence, initiation and cohesive behavior are not covered. With the broad establishment of finite element methods for problems related to continuum mechanics, also new methods for simulating fracture processes emerged: Approaches based on remeshing and usage of special crack tip elements [12, 122], the node split method [106], cohesive elements and cohesive zones models [11, 110] and XFEM [92]. Those methods allow overcoming some previously mentioned limitations of theories rooted in Griffiths's work, however, each approach comes with its own weaknesses.

One of the most recent and promising method is the so-called phase field method for fracture. This method was initially proposed by Francfort and Marigo [48] and is also rooted in Griffith's theory of brittle fracture, however, formulated by a variational approach, through which the total energy of the system is minimized. The main advantage is that no predefined crack paths are needed and branching as well as coalescence of cracks is naturally included in this approach. However, finding a solution to the proposed framework turned out to be very difficult. Therefore, in Bourdin et al. [20] and Bourdin et al. [21] a regularization method was developed that allows the minimization problem to be solved numerically efficient. By introduction of an auxiliary field $d(x) \in [0, 1]$ – the so-called crack phase field – the crack discontinuity is modeled by including a smooth transition zone from intact ($d = 0$) to cracked ($d = 1$) solid. The width of this transition zone is controlled by a regularization or length scale parameter. As this parameter approaches zero (i.e., recovering the discontinuous transition from solid to crack), the solution gamma-converges to Griffith's theory.

By expressing cracks in form of a field variable, the mentioned complex fracture phenomena like kinking, branching and coalescence, naturally arise from the defining system of differential equations. Thus, the phase field method theoretically allows crack topologies of arbitrary complexity, only limited by the mesh size and mesh structure. This motivates usage of the phase field method for materials with a complex micro- or macrostructure, like concrete, fiber-reinforced composites, polycrystalline structures and wood. In those materials, the micro- and macrostructure strongly affects both the elastic behavior, in the sense of having anisotropic constitutive relationships, and the crack topology, by introduction of favorable fracture planes due to "weak" principal material directions.

3.1.1 Fracture phenomena of wood

For wood, this results in crack topologies driven by both the direction of least resistance, orthogonal to the wood fiber direction, and the maximum principal stress [127]. This causes the often observed zig-zag pattern, where cracks jump from one growth layer to another, representing a combination of Mode-I, Mode-II and Mode-III failure modes. In this way, material specific microstructural features might influence the fracture behavior and crack propagation during and after crack formation in complex materials. In wood, crack growth is mainly triggered by defects in the cell wall material at a microscopic level. This

induces the often observed decrease in macroscopic stiffness, evidently visible in load-deflection plots, i.e., the nonlinear behavior before reaching the peak load. Close to the actual peak load the microscopic cracks localize and the actual macroscopic crack and fracture process zone forms. Failure processes in wood after crack initiation, like cohesive behavior, where studied by Vasic et al. [134] and are also observable in the experimental study of Dourado et al. [38]. Their research concluded with identifying so-called fiber bridging as the main cause of toughening effects at the crack tip.

3.1.2 The phase field method for anisotropic materials

The phase field models proposed by Amor et al. [9] and Miehe et al. [88] contain the assumptions of isotropic constitutive behavior and ideal-brittle fracture. However, in recent years, some approaches to allow for consideration of anisotropic behavior were published: Bleyer and Alessi [15] proposed a method that introduces additional phase field degrees of freedom (DOFs), which are uncoupled in the geometrical terms of the phase field equation and thus allow for different fracture energy release rates and length scale parameters. The actual coupling is introduced on a constitutive level. A different approach for anisotropic fracture is pursued by Clayton and Knap [27], Hakim and Karma [60], and Teichtmeister et al. [132]. Preferable fracture directions are introduced through a second-order tensor – the so-called structural tensor. This tensor scales the gradient of the crack phase field and imposes an orientation on the geometrical terms of the phase field equation. To allow for multiple favorable fracture planes, which are e.g., found in polycrystalline structures, Nguyen et al. [96] combined the multi-phase field model and the structural tensor. In their work, multiple phase variables are linked to their own second-order structural tensor that invalidates crack growth in a particular direction. Effectively, by suppressing one direction, multiple favorable fracture planes, defined by the material's microstructure, can be considered. Multiple fracture planes are also considered by Zhang et al. [155], where instead of using multiple phase field variables, the gradient of the phase field is scaled depending on the phase field crack's normal direction. The extensions of the phase field method mentioned above can also predict crack growth in composite materials. However, the fracture description in composite materials is challenging as it involves the fracture of the matrix and the constituents, their interaction, and interface failure. Bui and Hu [22] and Wu et al. [146] give a comprehensive overview of currently pursued approaches. On the macroscopic Dhas et al. [35] proposed a model for considering delamination limited to single fracture mechanics failure modes. Further developments target simulation on the micro- or mesoscale by explicitly modeling the matrix and the constituents. Msekh et al. [94, 95] show phase field implementations for nanocomposite materials. Failure of fiber reinfoced composite lamina is considered by Espadas-Escalante et al. [43]. Roy et al. [116] and Zhang et al. [152, 153] focus on the special treatment of fiber-matrix debonding, matrix cracking and the interaction of those failure modes. A multi-phase field model considering separate phase fields for the matrix and the inclusion phase is proposed by Singh and Pal [126].

3.1.3 Cohesive behavior in the phase field method

Already the original publication [20], covering the numerical implementation of the model from Francfort and Marigo [48], discusses the role of the length scale parameter. This was further elaborated by Amor et al. [9]. Initially, the length scale parameter was seen as a purely numerical value in the context of the regularization scheme. However, considering it a material parameter is not far-fetched due to the similarities of the phase field method with gradient damage approaches. With this parameter tending towards zero, the solution gamma-converges to Griffith's theory, describing ideal brittle failure. By increasing this parameter, more complex softening behavior can be described, and ductile effects of quasi-brittle material failure can be implemented An alternative approach is proposed by Wu [143] in the

form of the so-called unified phase field method, where the phase field's characteristic functions are tuned to a cohesive zone model with a predefined traction separation constitutive relation. In their work, the length scale parameter is regarded as a numerical value that can be chosen as small as possible, as long as it is sufficiently resolved by the spatial discretization [147]. The ductile behavior can be controlled by including the material's tensile strength in the formulation. This is an advantage in comparison to other phase field models, as the length scale parameter is not linked to material properties and can be chosen following the model's discretization [97]. Cervera et al. [25] and Wu et al. [148] show that the unified phase field theory yields almost identical results as the XFEM approach for quasi-brittle simulations while having the advantage of being able to properly model complex crack paths, crack kinking and crack branching.

3.1.4 Scope of this work

In this paper, a cohesive phase field implementation is presented based on the above-mentioned unified model from Wu [143]. Furthermore, the outlined methods for considering anisotropic behavior are evaluated and their possible combinations and limitations are discussed. Based on the work of Hu et al. [66], a novel hybrid approach [7], employing a crack boundary condition for the degradation part of the phase field equation, is formulated.

The paper is organized as follows: Section 3.2 provides the theoretical background and introduces methods and concepts from recent literature. Additionally, a generalization of the stress split from Steinke and Kaliske [129] for anisotropic materials is given and the hybrid approach, utilizing a crack boundary condition, is described. In Section 3.3 the introduced phase field models are evaluated using two numerical examples with different levels of complexity. First, a simple single edge notch plate with a predefined material direction is looked at. The simulation results serve as a basis for the discussion of the hybrid approach described in this work. Secondly, a more complex realistic model of a wooden board with a single knot is simulated to show the effects of spatially varying principal material directions, resulting from different wood fiber orientations. The paper closes with a short summary of the introduced concepts for applying the phase field model to orthotropic materials showing different complex damage mechanisms, and gives a brief outlook and concluding remarks.

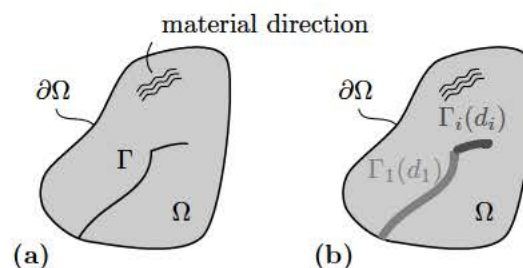## 3.2 Fundamentals and Methods

3.2.1 Fundamentals

Fig. 3.1: (a) sharp and (b) diffuse representation of a crack topology. Within the diffuse representation, the sharp crack Γ in the body Ω is approximated using multiple diffuse crack fields, which depend on the crack phase fields $\boldsymbol{d}$.

To verify the various methods able to take anisotropic and quasi-brittle behavior into account, the unified phase field model from Wu and Nguyen [145] is generalized to include n different phase field variables [15] and a second-order structural tensor $\boldsymbol{A}_i$ [96, 132], where i denotes the i-th phase field. Excluding body forces and surface tractions, the regularized form of the total energy Π of the system, defined on the domain Ω, thus reads:

$$\Pi(\boldsymbol{u}, \boldsymbol{d}) = \int_\Omega \left[\psi^+(\boldsymbol{u}, \boldsymbol{d}) + \psi^-(\boldsymbol{u}) \right] d\Omega + \sum_i^n G_{c,i} \int_\Omega \gamma_i(d_i) d\Omega, \tag{3.1}$$

where $\boldsymbol{u}$ is the displacement field, $\boldsymbol{d}$ the phase field of dimensionality n, $G_{c,i}$ the critical energy release rate of phase field i and γ_i is the regularized crack surface density functional that approximates the sharp crack surface. As the driving force for crack propagation is energy based, a criterion is needed for preventing fracture under pure compressive stress states modes. Thus, the strain energy density is separated into $\psi^+(\boldsymbol{u}, \boldsymbol{d})$ which contributes to fracture and $\psi^-(\boldsymbol{u})$ which does not. Only ψ^+ depends on the crack phase field $\boldsymbol{d}$, in such a way that the so-called degradation function $\omega(d_i)$, which damages the solid Ω, degrades the strain energy density.

Within the unified phase field theory, the crack surface density functional is defined as

$$\gamma_i(d_i) = \frac{1}{c_{0,i}} \left[\frac{1}{l_i} \alpha(d_i) + l_i \nabla d_i \cdot \boldsymbol{A}_i \cdot \nabla d_i \right] \text{ with } c_{0,i} = 4 \int_0^1 \sqrt{\alpha(\zeta)} d\zeta. \tag{3.2}$$

As outlined in Kuhn et al. [76] and Pham et al. [109], the function $\alpha(d_i)$ defines the local part of the dissipated fracture energy and determines the ultimate crack phase field. It satisfies the properties $\alpha(d = 0) = 0$ and $\alpha(d = 1) = 1$ [145]. In order to recover the actual surface measure of the crack set for $l_i \to 0$, the normalization constant $c_{0,i}$ is needed. $\boldsymbol{A}_i$ is the so-called structural tensor, which scales the gradient of the crack phase field to define preferable or invalid crack propagation directions. In a multi-phase field setting, the definition

$$\boldsymbol{A}_i = \boldsymbol{I} + \beta_i \left(\boldsymbol{I} - \boldsymbol{a}_i \otimes \boldsymbol{a}_i \right) \tag{3.3}$$

from Nguyen et al. [96] can be used, which allows assigning material directions $\boldsymbol{a}_i$ and penalty factors β_i for penalizing planes not orthogonal to the material directions for each phase field variable d_i. For $\beta_i = 0$, the standard isotropic formulation of the crack surface density functional is recovered. For increasing values of β_i, the crack surface energy decreases along the material direction $\boldsymbol{a}_i$, whereas the plane orthogonal to $\boldsymbol{a}_i$ remains unaffected. This introduces an anisotropy and invalidates crack propagation along the material direction.

The two functions that mainly influence the fracture process are the degradation function $\omega(d_i)$ and $\alpha(d_i)$. As described by Bleyer and Alessi [15], while multiple phase field variables are geometrically uncoupled (e.g., $\alpha(d_i)$ is defined for each DOF), they are coupled in the constitutive relation (e.g., $\psi^+(\boldsymbol{u}, \boldsymbol{d})$ is defined for all DOFs). A general expression for those two functions is given by Wu [142], in the following way

$$\alpha_i(d_i) = \xi d_i + (1 - \xi) d_i^2 \quad \forall d_i \in [0, 1] \, \xi \in [0, 2] \text{ and} \tag{3.4}$$

$$\omega_i(d_i) = \frac{(1 - d_i)^p}{(1 - d_i)^p + Q(d_i)} \quad p \geq 2 \tag{3.5}$$

$$Q_i(d_i) = a_{1,i} d_i + a_{1,i} a_{2,i} d_i^2 + a_{1,i} a_{2,i} a_{3,i} d_i^3, \tag{3.6}$$

where $a_{1,i}$, $a_{2,i}$ and $a_{3,i}$ are coefficients that can be calibrated to model a certain cohesive behavior related to the i-th phase field.

The general expression for the local part of the dissipated fracture energy resembles the well-known monotonous model. Equation (4.4) can be specialized for the two commonly used models $\alpha(d_i) = d_i$ for $\xi = 1$ (AT-1) and $\alpha(d_i) = d_i^2$ for $\xi = 0$ (AT-2) [8].

As outlined in Miehe et al. [88], the degradation function must satisfy $\omega(d_i = 0) = 1$ and $\omega(d_i = 1) = 0$. Furthermore, as the first derivative of the degradation function with respect to the phase field variable controls the amount of energetic driving force, $\omega'(d_i = 1) = 0$ is needed, in order to eliminate this elastic driving term once full damage is reached [76, 88]. This ultimately stops further crack growth in regions characterized by $d_i = 1$. Steinke and Kaliske [129] discuss the additional soft requirement of $\omega(d_i = 0) \neq 0$, which, if not satisfied, as well leads to the elimination of the elastic driving term. For $d_i = 0$, i.e., the undamaged state, crack growth is hindered, and no phase field evolution can take place. Therefore, such a model requires additional treatment in form of a numerical perturbation of the initial state, such that the energetic driving forces become unequal to zero. One commonly used definition is $\omega(d_i) = (1 - d_i)^2$ [89]. The general expression in Equation (4.5) contains this simple case for $p = 2$, $a_1 = 2$, $a_2 = -1/2$ and $a_3 = 0$.

The remaining part left to be specified from Equation (4.1) is the strain energy density split. In order to properly discuss the various kinds of methods to approach this separation, at first, two commonly applied methods for dealing with coupled equations within the variation framework are discussed.

3.2.2 Isotropic, anisotropic and hybrid formulation

As described by Ambati et al. [7], there are two basic formulations originating from the regularized variational framework [20, 21], the isotropic formulation and the anisotropic formulation [88, 89][1]. The isotropic formulation does not contain the additive decomposition of the strain energy density and, thus, gives a linear relation in $\boldsymbol{u}$, reading

$$\boldsymbol{\sigma}(\boldsymbol{u}, \boldsymbol{d}) = \frac{\partial \psi(\boldsymbol{u}, \boldsymbol{d})}{\partial \boldsymbol{\varepsilon}}. \tag{3.7}$$

The anisotropic formulation

$$\boldsymbol{\sigma}(\boldsymbol{u}, \boldsymbol{d}) = \frac{\partial \psi^+(\boldsymbol{u}, \boldsymbol{d}) + \psi^-(\boldsymbol{u})}{\partial \boldsymbol{\varepsilon}}, \tag{3.8}$$

however, contains the split and is thus non-linear in $\boldsymbol{u}$. This property simplifies the solution process when the so-called staggered approach is used (see Section 3.2.4), as the deformation subproblem can be treated as an uncoupled linear problem.

One obvious downside of the isotropic formulation is that every deformation state is degraded equally, thus unphysical behavior like interpenetration of crack faces or crack growth under pure compressive stress states can occur. Each effect is related to a different aspect of the evolution equations. Crack growth is rooted in the energetic driving force and interpenetration of crack faces in the constitutive relation. The so-called hybrid formulation [7] combines the advantages of both formulations, i.e., the linear behavior of the isotropic formulation and the physical, more appropriate, modeling of the anisotropic one. This is achieved by using the constitutive relation from Equation (3.7) with the additional constraint that for all $\boldsymbol{u}$ with ψ^+ smaller than ψ^- (i.e., the passive energy parts outweighs the crack driving one), the material is treated as undamaged, i.e., $d_i = 0$. For the energetic driving force, the anisotropic formulation is used, leading to the proper crack propagation behavior. As shown in Ambati et al. [7], the hybrid formulation

---

[1]The terms isotropic and anisotropic are not to be interpreted in terms of the local material behavior, but they refer to the decomposition of the strain energy density

manages to produce results qualitatively and quantitatively similar to the anisotropic formulation, with a computation effort close to the isotropic formulation.

3.2.3 Fracture contributing and passive parts

The energy split into a part that drives and is affected by fracture and into a part that is neither affected by nor drives fracture is one key ingredient of the phase field formulation for ensuring a realistic fracture behavior. As outlined in Section 3.2.2, by ignoring this split, i.e., using the isotropic formulation, effects like interpenetration of crack faces or crack growth under pure compressive stress states can occur. This unphysical behavior can be eliminated by properly splitting the energy, such that the energetic driving force and also the damaged part in the constitutive relation is only related to the contributing part ψ^+.

Besides this physical motivation, there is also a simple conceptional one: The additive decomposition $\psi = \psi^+ + \psi^-$, must retain its validity. In Dijk et al. [36], this is very well explained based on the two common methods for splitting the strain energy density: the spectral decomposition by Miehe et al. [88] and the volumetric-deviatoric decomposition by Amor et al. [9]. Starting with the well-known formulation of the strain energy density, the fundamental idea is to separate stresses and strains into strictly fracture-contributing and passive parts. Hence, the strain energy density reads

$$\psi = \frac{1}{2}(\boldsymbol{\sigma}^+ + \boldsymbol{\sigma}^-) : (\boldsymbol{\varepsilon}^+ + \boldsymbol{\varepsilon}^-) \tag{3.9}$$

$$= \frac{1}{2}(\underbrace{\boldsymbol{\sigma}^+ : \boldsymbol{\varepsilon}^+}_{\psi^+} + \boldsymbol{\sigma}^+ : \boldsymbol{\varepsilon}^- + \boldsymbol{\sigma}^- : \boldsymbol{\varepsilon}^+ + \underbrace{\boldsymbol{\sigma}^- : \boldsymbol{\varepsilon}^-}_{\psi^-}). \tag{3.10}$$

So, for the additive decomposition to hold, the terms $\boldsymbol{\sigma}^+ : \boldsymbol{\varepsilon}^-$ and $\boldsymbol{\sigma}^- : \boldsymbol{\varepsilon}^+$, consisting of contributing and passive parts, must vanish. However, for non-isotropic materials, those parts are non-zero, thus the spectral and the volumetric-deviatoric decomposition can not be applied.

The phase field formulation consists of two essential parts, one being the formulation of the energetic driving force and the other being the actual constitutive behavior. On those two parts, the above described decomposition has a very different impact. Regarding the first part, Miehe et al. [90] introduced the concept of a dimensionless crack driving function, which is a generalization of the history function [88] and allows replacing the energetic driving force by an arbitrary failure function, like a maximum stress, a maximum strain or a Tsai-Wu [57] criterion. While this opens the phase field formulation to a variety of materials, the restrictions on the constitutive relation remain. However, the current literature finally provides three approaches of a valid strain energy decomposition for non-isotropic materials:

- A proper split for anisotropic materials [36], based on generalizations of decomposition from Miehe et al. [88] and Amor et al. [9], which is not yet validated,

- a stress-based split [66, 129] that is based on a different formulation of Equation (3.9) and

- the hybrid approach described in Section 3.2.2.

The hybrid approach is a simple method to circumvent the validity of the split, as for the constitutive part no split is required. In a sense, the hybrid approach represents a generalized framework for applying arbitrary crack driving functions, as long as an additional constraint ensures that crack faces cannot interpenetrate. The additional constraint formulation from Ambati et al. [7], where for $\psi^- > \psi^+$ contact of the crack faces is assumed, however, might not be suitable for any crack driving function, thus, requiring an alternative formulation of this constraint, suited for ensuring a physical, sound fracture behavior.

A stress-based split represents an alternative approach for separating the strain energy density into a contributing and a passive part. The method, as described by Steinke and Kaliske [129], is based on the idea that only stresses are additively decomposed. So Equation (3.9) changes to

$$\psi = \frac{1}{2}(\boldsymbol{\sigma}^+ + \boldsymbol{\sigma}^-) : (\boldsymbol{\varepsilon}) = \frac{1}{2}(\underbrace{\boldsymbol{\sigma}^+ : \boldsymbol{\varepsilon}}_{\psi^+} + \underbrace{\boldsymbol{\sigma}^- : \boldsymbol{\varepsilon}}_{\psi^-}). \tag{3.11}$$

Obviously, this approach is applicable to any constitutive behavior, as there are no terms consisting of both contributing and passive parts. Nevertheless, Steinke and Kaliske [129] specialized the model for isotropic materials, as some observations on the inherent properties of the deformations in presence of a crack, discussed below, require changes in the initial formulation of $\boldsymbol{\sigma}^+$.

The stress based split is performed in a local crack coordinate system, as shown in Figure 4.2. This coordinate system, related to a fictitious crack surface defined by the crack normal vector r and the two in-plane vectors s and t, allows identification of crack driving forces for Mode-I, Mode-II and Mode-III fracture. By representing the stress tensor in the crack coordinate system, the crack driving and passive stresses can be identified:

$$\boldsymbol{\sigma}^+ = \underbrace{\langle \sigma_{rr} \rangle_+ (r \otimes r)}_{\text{Mode-I}} + \underbrace{\boldsymbol{\sigma}_{rt} + \boldsymbol{\sigma}_{tr}}_{\text{Mode-II}} + \underbrace{\boldsymbol{\sigma}_{rs} + \boldsymbol{\sigma}_{sr}}_{\text{Mode-III}} \text{ and} \tag{3.12}$$

$$\boldsymbol{\sigma}^- = \langle \sigma_{rr} \rangle_- (r \otimes r) + \boldsymbol{\sigma}_{tt} + \boldsymbol{\sigma}_{ss} + \boldsymbol{\sigma}_{ts} + \boldsymbol{\sigma}_{st}, \tag{3.13}$$

where $\boldsymbol{\sigma}_{ij} = \sigma_{ij}(i \otimes j)$ and $\sigma_{ij} = \boldsymbol{\sigma} : (i \otimes j)$, which are the contributions to the stress tensor and the stress related to the i and j direction from the crack coordinate system, respectively. Further, Macaulay's notation is used as $\langle \bullet \rangle_+ = (\bullet + | \bullet |)/2$ and $\langle \bullet \rangle_- = (\bullet - | \bullet |)/2$. Zhang et al. [151] follow a similar decomposition approach which allows specifying the fracture energy release rate for each fracture mechanics failure mode. In their work a fiber reinforced composite is considered. The energy is divided by a stress-based decomposition into fiber and matrix dominant damage, where, for the latter, additionally Mode-I and Mode-II fracture is considered. In comparison to the model used in this work, the crack coordinate system is fixed to the local fiber coordinate system, so the effect of different crack face orientations on the crack driving forces cannot be captured.
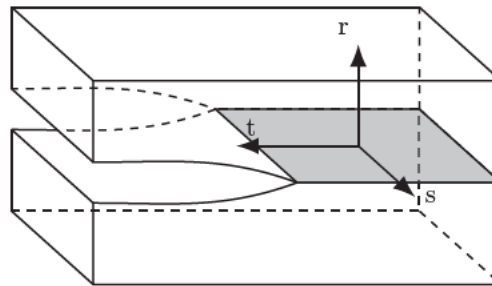

Fig. 3.2: Crack coordinate system of a fictitious crack surface, required to identify Mode-I, Mode-II and Mode-III crack driving forces.

At this point, the decomposition is still applicable to any constitutive law, however, it can lead to physically inconsistent results, as in the fully damaged state the essential crack boundary conditions – no positive normal stress perpendicular to the crack and no shear stresses along a frictionless crack surface [130] – are not recovered for certain strain states. This unphysical behavior can easily be shown by picturing a state of pure crack normal strain (i.e., $\varepsilon_{rr} > 0$ and all other strain components equal to

zero). As a generalization of the isotropic model from Steinke and Kaliske [129], following a linear elastic constitutive law, such a strain state would result in non-zero stress components:

$$\sigma_{rr} = C_{rrrr}\varepsilon_{rr} \text{ and} \tag{3.14}$$

$$\sigma_{ij} = C_{ijrr}\varepsilon_{rr}. \tag{3.15}$$

A fully developed crack state, however, should be stress-free due to this very strain state, as the two crack surfaces should be able to move freely along the crack's normal vector. Additionally, the stresses related to *Poisson's* effect (Equation (3.15)), must be considered in the fracture contributing stresses $\boldsymbol{\sigma}^+$, by expressing them in terms of the crack normal stresses from Equations (3.14) and (3.15) as

$$\sigma_{ij} = \frac{C_{ijrr}}{C_{rrrr}}\sigma_{rr}, \tag{3.16}$$

which leads to the following formulation of the crack contributing and passive stresses:

$$\begin{aligned}
\boldsymbol{\sigma}^+ = \langle\sigma_{rr}\rangle_+ (\boldsymbol{r}\otimes\boldsymbol{r}) + \boldsymbol{\sigma}_{rt} + \boldsymbol{\sigma}_{tr} + \boldsymbol{\sigma}_{rs} + \boldsymbol{\sigma}_{sr} + \frac{\langle\sigma_{rr}\rangle_+}{C_{rrrr}}\big[C_{ssrr}(\boldsymbol{s}\otimes\boldsymbol{s})+ \\
+ C_{ttrr}(\boldsymbol{t}\otimes\boldsymbol{t}) + C_{rtrr}(\boldsymbol{r}\otimes\boldsymbol{t}) + C_{rsrr}(\boldsymbol{r}\otimes\boldsymbol{s}) + C_{trrr}(\boldsymbol{t}\otimes\boldsymbol{r}) + C_{srrr}(\boldsymbol{s}\otimes\boldsymbol{r})+ \\
+ C_{tsrr}(\boldsymbol{t}\otimes\boldsymbol{s}) + C_{strr}(\boldsymbol{s}\otimes\boldsymbol{t})\big]
\end{aligned} \tag{3.17}$$

$$\begin{aligned}
\boldsymbol{\sigma}^- = \langle\sigma_{rr}\rangle_- (\boldsymbol{r}\otimes\boldsymbol{r}) + \boldsymbol{\sigma}_{tt} + \boldsymbol{\sigma}_{ss} + \boldsymbol{\sigma}_{ts} + \boldsymbol{\sigma}_{st} - \frac{\langle\sigma_{rr}\rangle_+}{C_{rrrr}}\big[C_{ssrr}(\boldsymbol{s}\otimes\boldsymbol{s})+ \\
+ C_{ttrr}(\boldsymbol{t}\otimes\boldsymbol{t}) + C_{rtrr}(\boldsymbol{r}\otimes\boldsymbol{t}) + C_{rsrr}(\boldsymbol{r}\otimes\boldsymbol{s}) + C_{trrr}(\boldsymbol{t}\otimes\boldsymbol{r}) + C_{srrr}(\boldsymbol{s}\otimes\boldsymbol{r})+ \\
+ C_{tsrr}(\boldsymbol{t}\otimes\boldsymbol{s}) + C_{strr}(\boldsymbol{s}\otimes\boldsymbol{t})\big]
\end{aligned} \tag{3.18}$$

Equation (4.9) is based on Equation (3.12), which contains crack driving stresses identified using classic fracture mechanics failure modes. In addition, Equation (4.9) also considers the stresses related to *Poisson's* effect, which must vanish for a fully developed phase field. Having this formulation for $\boldsymbol{\sigma}^+$ allows finding $\boldsymbol{\sigma}^-$ from $\boldsymbol{\sigma} = \boldsymbol{\sigma}^+ + \boldsymbol{\sigma}^-$. It can be shown that this generalized formulation of the stress split contains the isotropic formulation proposed by Steinke and Kaliske [129]. In the isotropic case, only the entries $C_{rrrr} = \lambda + 2\mu$, $C_{ssrr} = C_{ttrr} = \lambda$, required for the additional decomposed stresses, are non-zero, leading to the expression

$$\boldsymbol{\sigma}^+ = \langle\sigma_{rr}\rangle_+ (\boldsymbol{r}\otimes\boldsymbol{r}) + \boldsymbol{\sigma}_{rt} + \boldsymbol{\sigma}_{rs} + \boldsymbol{\sigma}_{tr} + \boldsymbol{\sigma}_{ts} + \frac{\lambda}{\lambda + 2\mu}\langle\sigma_{rr}\rangle_+ (\boldsymbol{s}\otimes\boldsymbol{s} + \boldsymbol{t}\otimes\boldsymbol{t}), \tag{3.19}$$

where λ and μ are the two *Lamé* constants. This expression matches the one from Steinke and Kaliske [129].

3.2.3.1 A novel hybrid approach based on a crack boundary condition

Referring to the key requirement defined in Strobl and Seelig [130] that in a fully damaged state, tensile crack normal stresses and shear stresses along a frictionless crack surface should be zero, Hu et al. [66] developed a stress-based decomposition approach based on a smooth traction-free crack boundary condition. This approach is similar to the stress-based split by Steinke and Kaliske [129], however, instead of considering degradation from the perspective of crack driving stresses in Mode-I, Mode-II and Mode-III,

they view degradation as a contact problem. With $\boldsymbol{r}$ as the crack face's normal vector, this results in the following decomposition of the stress tensor:

$$\boldsymbol{\sigma}^+ = \underbrace{\langle\sigma_{rr}\rangle_+ (\boldsymbol{r} \otimes \boldsymbol{r})}_{\text{tensile normal stress}} + \underbrace{\boldsymbol{\sigma} - \sigma_{rr}(\boldsymbol{r} \otimes \boldsymbol{r})}_{\text{tangential stress}} \tag{3.20}$$

$$\boldsymbol{\sigma}^- = \underbrace{\langle\sigma_{rr}\rangle_- (\boldsymbol{r} \otimes \boldsymbol{r})}_{\text{compressive normal stress}} \tag{3.21}$$

The main difference compared to Equations (4.9) and (4.10) is in the treatment of tangential components, which in the case of the crack boundary condition always result in an energetic driving force. This results in an unrealistic overestimation of the driving strain energy density (e.g., $\boldsymbol{\sigma}_{tt}$ and $\boldsymbol{\sigma}_{ss}$ are considered crack driving). Therefore, Hu et al. [66] highlight that this decomposition approach should not be used for crack initiation and crack propagation, but should only serve as a boundary condition, which is activated after the phase field variable reaches a certain threshold.

An alternative approach for dealing with the problem of having unphysical crack driving forces is utilizing the properties of the hybrid approach (Section 3.2.2). As discussed in Section 3.2.3, this method allows arbitrary combinations of energetic driving forces and definitions of the constitutive behavior, given that the solver is based on the staggered approach (see Section 3.2.4). Commonly, the isotropic formulation from Equation (3.7) is used for defining the constitutive behavior, which, however, requires an additional constraint for preventing interpenetration of crack faces. In order to circumvent this additional constraint, we therefore propose using

$$\boldsymbol{\sigma}^+ = \langle\sigma_{rr}\rangle_+ (\boldsymbol{r} \otimes \boldsymbol{r}) + \boldsymbol{\sigma}_{rt} + \boldsymbol{\sigma}_{tr} + \boldsymbol{\sigma}_{rs} + \boldsymbol{\sigma}_{sr} + \boldsymbol{\sigma}_{tt} + \boldsymbol{\sigma}_{ss} + \boldsymbol{\sigma}_{ts} + \boldsymbol{\sigma}_{st} \text{ and} \tag{3.22}$$

$$\boldsymbol{\sigma}^- = \langle\sigma_{rr}\rangle_- (\boldsymbol{r} \otimes \boldsymbol{r}), \tag{3.23}$$

which matches the formulation from Hu et al. [66], for defining the constitutive behavior, where only $\boldsymbol{\sigma}^+$ is degraded. The crack driving part of the coupled system remains based on the orthotropic stress split derived in Section 3.2.3. This additionally bypasses the need for considering the crack boundary condition only after the phase field variable reaches a certain threshold, as the driving parts are now rooted in the classic fracture mechanic failure modes. To conclude, we propose using a stress-based decomposition, where crack driving stresses are identified by fracture mechanics failure modes (Equations (4.9) and (4.10)), in a hybrid-approach, combined with a degradation function, where stresses are degraded, such that the resulting constitutive behavior matches the one of a traction-free crack surface (Equations (4.11) and (4.12)). This allows physical, sound estimation of crack driving forces for orthotropic materials and proper modeling of crack faces.

3.2.3.2 Application of the stress split in a multi-phase field theory

In highly orthotropic materials, fracture is driven based on two principles [127]:

- Cracks following the direction of least resistance, defined by the microstructure of the material.

- Cracks opening perpendicular to the largest principal stress, thus, leading to a maximum reduction of the total energy.

For wood this results in the often observed zig-zag pattern (Figure 4.3), where cracks follow the path of maximum total energy reduction, until reaching a growth ring. At the growth ring, which is essentially a weak interface, the crack direction changes to the direction of least resistance, which for wood is always

parallel to its fiber direction. So cracks are likely to follow the material's structure, i.e., for wood the longitudinal, radial or tangential direction.
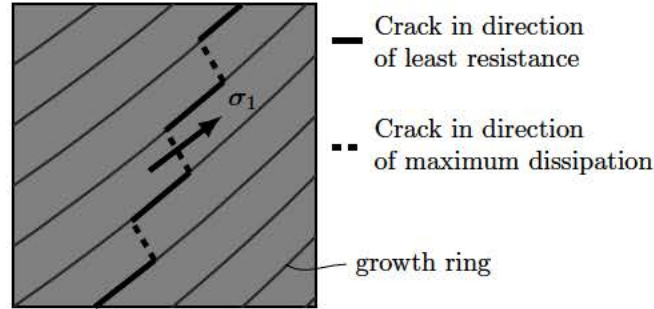

Fig. 3.3: Typical crack pattern observed for wood. A crack switches from following the direction of least resistance along the fiber, to the direction of maximum total energy reduction perpendicular to the largest principal stress. It changes its orientation again, when it hits the next growth ring. [127]

The fundamental part of the stress-based decomposition is the definition of the crack coordinate system. Due to the material characteristics and often observed crack pattern of wood, instead of considering an arbitrary crack face orientation, the identification of three crack coordinate systems defined by r_i, s_i and t_i (see Figure 4.2) is plausible, where r_1 is the longitudinal, r_2 the radial and r_3 the tangential direction. This results in three different crack driving energy terms, where according to the principle of maximum dissipation, the failure mode with the highest energy release determines the main cause of failure.

In order to consider the very different fracture toughness and strength of each of the possible types of cracks (longitudinal, radial, tangential), each material axis is related to only a single phase field variable. This is similar to approaches taken for crystalline materials for considering the influence of cleavage planes [96]. The fracture energy release rate and the strength related to each phase field variable is considered in a mixed-mode manner. However, by selectively excluding certain failure modes in the mixed-mode formulation in Equations (4.9) and (4.10), it can easily be adapted. The proper choice of the respective material parameters and the internal length depends on the combination of failure modes. With the multi-phase field description, only the phase field variable related to driving failure mode is activated for degradation. In comparison to other multi-phase field models, e.g., Bleyer and Alessi [15] and Nguyen et al. [96], this approach results in no coupling of the phase field variables in the constitutive relation, as a single phase field variable is already sufficient to describe the state of a fully developed crack. Thus, the strain energy terms $\psi^+(\boldsymbol{u}, \boldsymbol{d})$ and $\psi^-(\boldsymbol{u}, \boldsymbol{d})$ in Equation (4.1), are replaced by

$$\psi_i^+(\boldsymbol{u}, \boldsymbol{d}) = \omega_i(d_i)\psi_i^+(\boldsymbol{u}) \text{ and } \psi_i^-(\boldsymbol{u}) = \psi_i(\boldsymbol{u}) - \psi_i^+(\boldsymbol{u}), \tag{3.24}$$

respectively, where i is the index of the defining failure mode and ψ_i^+ is defined according to ??.

From a numerical point of view, having no coupling between the phase field DOFs is favorable. However, choosing one driving failure mechanism introduces a strong non-linearity, as the strain energy density function depends on i, for which the total energy is not a continous function. This makes solving the problem very difficult, if not impossible. Therefore, instead of evaluating strong non-linearities (e.g., Heaviside functions or the Macaulay brackets) based on the current state variables, they are computed using the deformation and phase field values of the last converged increment. Given that the increments are sufficiently small, this vastly improves the convergence rate, while leading to similar results. Our tests showed no significant influence on the obtained solutions, except that the algorithm is more robust.

3.2.4 Solver

Solving the posed minimization problem is a challenging task, because of the regularized functionals being non-convex in the state variables [9]. Additionally, irreversibility constraints are necessary to ensure the thermodynamical consistency and fully dissipative nature of crack growth. In this work, the well established staggered approach is applied, solving the displacement field at a constant crack phase field and the crack phase field at a constant displacement field [6].

The algorithmic scheme applied in this work is outlined in the flowchart in Figure 4.4. Similar to what was proposed by Amor et al. [9], the following criteria are used as a convergence measure for the subproblems in iteration n and increment k,

$$\sum_{i\in\text{DOFs}} \frac{|\hat{\boldsymbol{d}}_{n+1,i}^k - \hat{\boldsymbol{d}}_{n,i}^k|}{|\hat{\boldsymbol{d}}_{n+1,i}^k|} \leq \epsilon_d \qquad \sum_{i\in\text{DOFs}} \frac{|\hat{\boldsymbol{u}}_{n+1,i}^k - \hat{\boldsymbol{u}}_{n,i}^k|}{|\hat{\boldsymbol{u}}_{n+1,i}^k|} \leq \epsilon_u \quad \text{with} \quad \epsilon_u < \epsilon_d. \tag{3.25}$$

Here, $\hat{\bullet}$ refers to the discretized representation of the continuous field $\bullet$. Additionally, the L^2-norm of the crack phase field's residual $\hat{\boldsymbol{R}}_{\hat{\boldsymbol{d}},n+1}^k$ must be smaller than or equal to $\epsilon_{R,d}$. Convergence of the overall problem is assured by requiring convergence of the deformation problem and the phase field problem. If the set of state variables resulting from the last phase field step ($\hat{\boldsymbol{d}}_{n+1}^k$ and $\hat{\boldsymbol{u}}_n^k$) result in a converged state for the deformation problem, the newly obtained deformation state $\hat{\boldsymbol{u}}_{n+1}^k$ is ignored (as the phase field subproblem converged for $\hat{\boldsymbol{u}}_n^k$) and $\hat{\boldsymbol{d}}_{n+1}^k$ and $\hat{\boldsymbol{u}}_n^k$ are accepted as a solution. The whole algorithm uses an adaptive time increment stepping scheme, such that a better performance can be achieved by having larger increments in less critical regions (e.g., linear elastic regime) and smaller increments in critical ones (e.g., close to peak load).
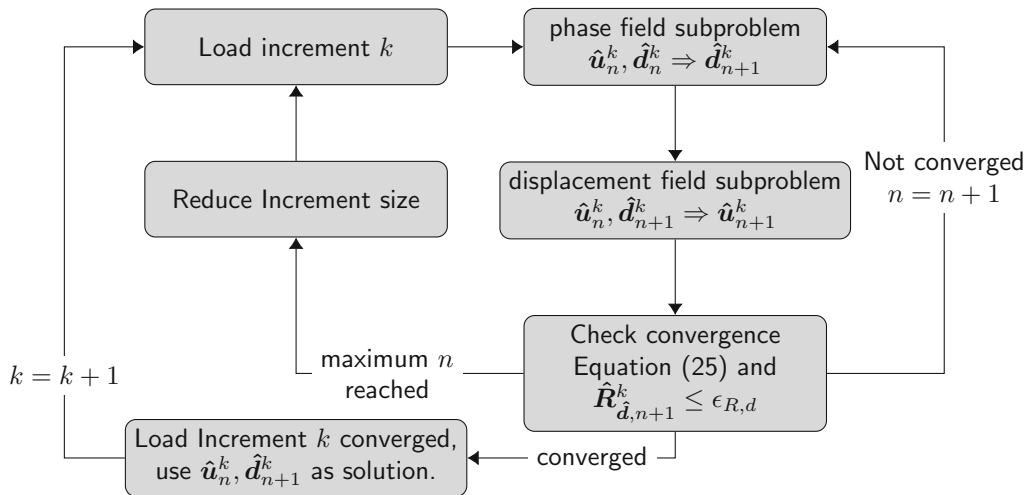

Fig. 3.4: Staggered solution process for a single load increment. Convergence is assured by imposing a limit on the size of the state variable's increment. Additionally, the residual of the phase field subproblem must lie below a threshold. The convergence of the overall problem is given by checking whether the last change in the crack phase field only resulted in a converged state in the displacement field.

As mentioned above, to ensure thermodynamical consistency, an irreversibility constraint on the phase field variable is required. Additionally, it is also necessary to ensure the bound constraint $d(x) \in [0,1]$. De Lorenzis and Gerasimov [32] give a quite comprehensive overview of current approaches. In this work, constraints are applied on the global level using the active set reduced space method [149]. Essentially Dirichlet-type boundary conditions are prescribed on a subset of $\hat{\boldsymbol{d}}$. The method is both qualitatively and

quantitatively similar to the primal-dual active set method from Heister et al. [61] (for a comparison see Section 3.A).

A set is said to be "active" when the inequality constraint is violated. In [149] a box constraint solver is discussed, identifying two sets, a lower bound active set $\mathcal{A}_\phi$ and an upper bound active set $\mathcal{A}_\psi$. The problem is, subsequently, solved on the inactive set

$$\mathcal{I}(\hat{\boldsymbol{d}}_{n+1}^k) = \mathcal{S} \setminus \left(\mathcal{A}_\phi(\hat{\boldsymbol{d}}_{n+1}^k) \cup \mathcal{A}_\psi(\hat{\boldsymbol{d}}_{n+1}^k) \right), \tag{3.26}$$

where $\mathcal{S}$ is the set of all crack phase field DOFs. The DOF values on the active set are fixed to the boundary values using hard Dirichlet-type boundary conditions. Applying this method would allow considering alternative degradation functions for which $\omega'(d_i = 1) \neq 0$, however, in this work no functions of this kind are used. The active sets are computed as follows[2]:

$$\mathcal{A}_\phi(\hat{\boldsymbol{d}}_{n+1}^k) = \left\{ i \in \mathcal{S} | \left(\hat{\boldsymbol{d}}_{n+1}^k \right)_i \leq \left(\hat{\boldsymbol{d}}^{k-1} \right)_i \text{ and } (\hat{\boldsymbol{R}}_{\hat{\boldsymbol{d}},n+1}^k)_i > 0 \right\} \tag{3.27}$$

$$\mathcal{A}_\psi(\hat{\boldsymbol{d}}_{n+1}^k) = \left\{ i \in \mathcal{S} | \left(\hat{\boldsymbol{d}}_{n+1}^k \right)_i \geq 1 \text{ and } (\hat{\boldsymbol{R}}_{\hat{\boldsymbol{d}},n+1}^k)_i < 0 \right\}, \tag{3.28}$$

where the lower bound is the element-wise restriction that the current state variable must be larger than or equal to the state variable from the last converged increment, i.e., $k-1$. These methods also affects the convergence conditions from above, such that the L^2-norm of the residual is only computed on the inactive set. To conclude, we propose using the staggered approach, as it is more robust than the monolithic one, in combination with the active set reduce spaced method, which allows assuring irreversibility without requiring additional terms like penalty functions in the phase field formulation.

The entire code is implemented in Julia [14]. For automatically deriving the element stiffness matrices and residual vectors from the energy formulation, the ForwardDiff-Package [115] is used. Pardiso 6.0 [30, 74, 135] is employed as the sparse linear solver.

3.3 Results and discussion

In the following Section, the stress split described in Section 3.2.3 is assessed based on two different models: A simple notched plate (Figure 3.5) with varying fiber orientation and a more complex example of a wooden board including a knot (Figure 3.12). As the envisioned use of the phase field model described in this work is the application to complex three-dimensional geometries, three-dimensional linear tetrahedral elements are used. Since the hybrid approach strongly alters the phase field formulation, it can be expected to provide different crack topologies, compared to the variationally consistent formulation (i.e., the anisotropic formulation from Section 3.2.2).

For all examples, the material stiffness tensor is defined as $C_{\mathrm{LLLL}} = 9000.016$, $C_{\mathrm{LLRR}} = 269.384$, $C_{\mathrm{LLTT}} = 175.104$, $C_{\mathrm{RRRR}} = 480.096$, $C_{\mathrm{RRTT}} = 118.528$, $C_{\mathrm{TTTT}} = 270.6$, $C_{\mathrm{RTRT}} = 32$, $C_{\mathrm{LRLR}} = 552$, $C_{\mathrm{LTLT}} = 552$, all in MPa. This resembles the elastic properties of so-called clear wood, describing wood areas without defects and knots. Following [84], to the knot in the wooden board example, a stiffness tensor reduced by a factor of 0.5, compared to the clear wood stiffness tensor, is assigned. This reduction takes cracks perpendicular to the grain direction, often observed in knots, into account. The elastic properties are defined in a local cylindrical coordinate system, as is commonly used for describing wood. $\boldsymbol{a}_1$ defines the longitudinal (L) direction, $\boldsymbol{a}_2$ the radial (R) direction and $\boldsymbol{a}_3$ the tangential (T) direction.

---

[2]In their work, Yang et al. [149] compare the current DOF's value with the one from the last converged state by equality. Given that they apply a special operator that cuts off values lower than the lower bound and larger than the upper bound, comparing by lower than or larger than, respectively, leads to the same result. We use those operators instead, to make the comparison to the primal-dual active set algorithm from Heister et al. [61] more clear.

In order to account for the cohesive behavior of wood, the coefficients $a_{1,i}$, $a_{2,i}$ and $a_{3,i}$ in Equation (4.6) are tuned to match a linear softening law. Based on the analytical solution of a one-dimensional bar problem, Wu [142] gives the following definitions:

$$a_{1,i} = \frac{4}{\pi} \frac{l_{ch,i}}{l_i}, \; a_{2,i} = -\frac{1}{2} \text{ and } a_{3,i} = 0, \tag{3.29}$$

for $\xi = 2$ and $p = 2$, in Equations (4.4) and (4.5), respectively. $l_{ch,i}$ defines *Irwin*'s characteristic length, given as $l_{ch,i} = {}^{E_{0,i}G_{c,i}}/f_{t,i}^2$, for the i-th phase field, and l_i is the length scale parameter for the i-th phase field, which is chosen to be larger than the effective element size l_{eff} (third root of the average volume of the finite elements in region of the expected phase field crack).

3.3.1 Single edge notched plate
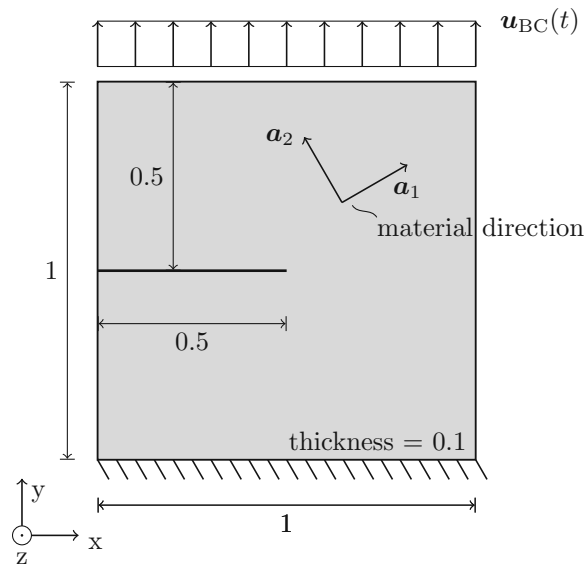
Fig. 3.5: Geometry of the single edge notched plate. In plane, the plate is fixed in all directions at the bottom edge and only out of plane across the entire back surface. The load is applied in form of a prescribed vertical deformation along the upper edge. The fiber direction $\boldsymbol{a}_1$ is changed by setting the fiber angle relative to the horizontal direction. All measurements are in mm.

The notched plate's geometry is depicted in Figure 3.5. In plane, it is supported at the bottom edge and out of plane on the entire back surface. The load is applied in form of a prescribed vertical deformation along the upper edge. For considering the orthotropic behavior, the fiber direction ($\boldsymbol{a}_1$) is changed by setting the fiber angle relative to the horizontal direction, e.g., 0° meaning $\boldsymbol{a}_1$ points into the x-direction and 90° meaning $\boldsymbol{a}_1$ points into the y-direction. The remaining axes are defined such that the tangential direction ($\boldsymbol{a}_3$) always points into the z-direction. The parameters controlling the phase field problem are given in Table 3.1.

Tab. 3.1: Defining parameters for the single edge notch plate problem.

d_i	$\beta_i{}^{\text{a}}$	$G_{c,i}{}^{\text{b}}$	$f_{t,i}{}^{\text{c}}$	l_i/l_{eff}
d_1	5.0	0.05	50.0	4.0
d_2	5.0	0.1	14.42	4.0
d_3	5.0	0.1	7.21	4.0

[a] Structural tensor scale in Equation (4.3)   [b] in Nmm/mm^2 [c] in MPa

In order to reduce the computational effort of such problems, often, the mesh density is increased in regions of a priori known crack paths. As changing the fiber angle is expected to also change the resulting crack topology, the crack paths cannot precisely be known in advance. Therefore, all models are consistently meshed with the same effective element size over the entire specimen's geometry. This greatly reduces the influence of the mesh structure on the resulting crack paths. Initially, seven different element sizes, ranging from a very coarse mesh with 2018 nodes to a very fine one with 144825 nodes, are tested. The finest mesh results from a characteristic element size of 0.005, a value which is also used in other publications, e.g., by Hu et al. [66].

The results of this mesh study are shown in Figure 3.6. For both the hybrid and the consistent approach, the total external energy, normalized to the maximum value of the external energy for the specific model and the studied fiber angle, is plotted over the number of nodes. For all five material directions, with increasing number of nodes, the total external energy shows clear convergence against a value that can already be captured well by the two finest meshes (6 and 7). This is also reflected in the phase field developments in Figure 3.6 (c), where there is no qualitative difference in the crack topology between mesh 6 and 7, however, a significant change in the failure mode in meshes 1 to 5. Therefore, only mesh number 7 was used, for the further simulations. Nevertheless, it should be pointed out that also mesh number 6, though quite coarse compared to common mesh sizes used in literature, could already be used, which would allow a major reduction of the computational effort. The simulations of the most refined meshes with 868950 DOFs were carried out using 2 *AMD EPYC 7402*. On average, solutions were found after 60 h (wall time). The speedup through parallelization is significant, recent work shows that further improvement is possible through semi-implicit methods [81] and BFGS iteration schemes [144]. Both vastly reduce the number of required iterations.

The generally low mesh sensitivity, as also pointed out by Yang et al. [150], is related to the usage of the unified phase field theory from Wu [142], as the regularization parameter is actually considered in the phase field formulation for calibration of the coefficients $a_{1,i}$, $a_{2,i}$ and $a_{3,i}$ in Equation (4.7), which compensates the size effect resulting from a larger crack phase field.
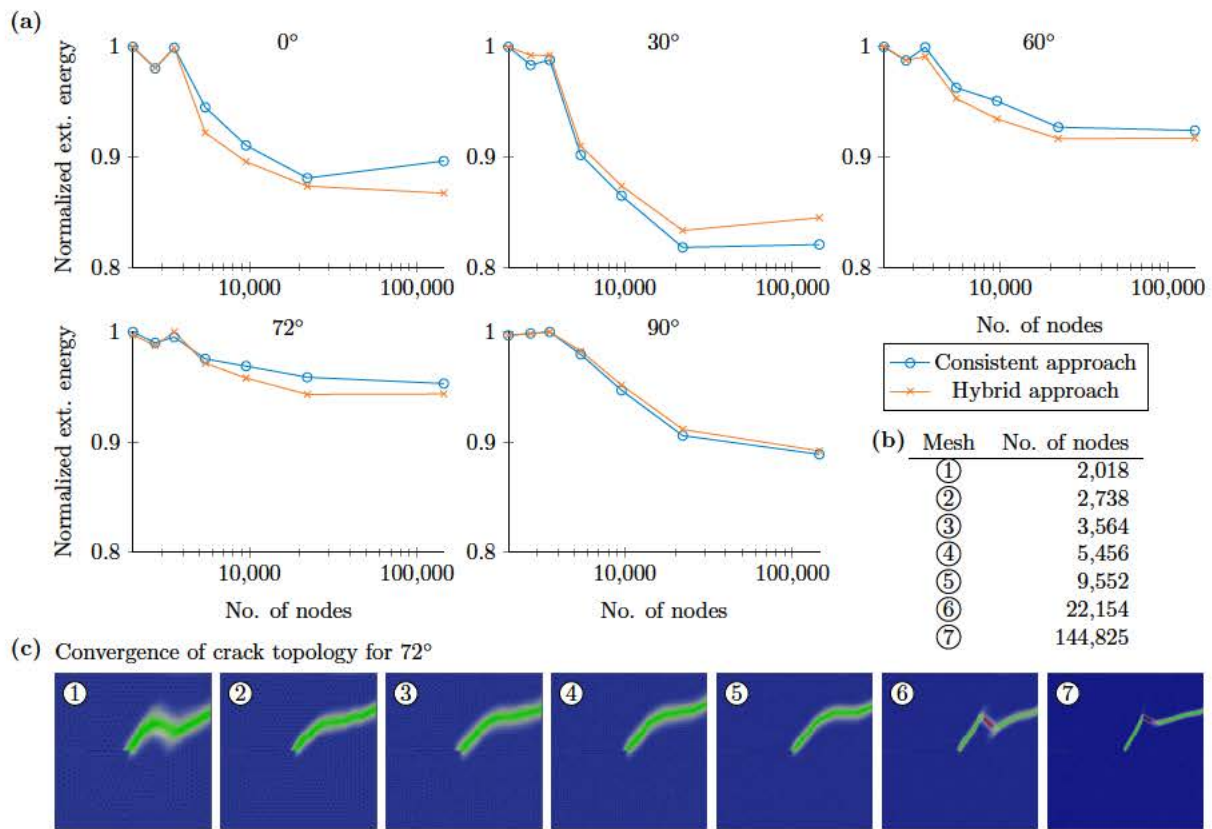
Fig. 3.6: Results of the mesh study (total external energy) for seven different meshes with increasing mesh density, for 5 different fiber angles and for both the consistent and the hybrid approach. Additionally, the crack topology for a fiber angle of 72° for the hybrid approach is depicted for each of the meshes.

As already pointed out, a main question of this work is to evaluate whether the proposed model is capable of considering effects resulting from the material structure appropriately. With respect to wood, it is of particular interest, whether the commonly observed zig-zag failure pattern (as shown in Figure 4.3), arising from cracks that jump between growth layers, can be modeled. In order to show this effect, various fiber angles ranging from 0° to 90° are investigated. Figure 3.7 shows the transition of failure modes, obtained with the hybrid approach, for selected characteristic fiber angles in this range, where the mesh and the load are identical. In Figure 3.7, qualitatively similar crack topologies are summarized in a graphic to improve comparability.

The results clearly show that at a certain fiber angle, the failure mode switches from a crack driven by stresses perpendicular to the fiber (d_2) to a crack driven by stresses in fiber direction (d_1). The first and foremost observation from those results is that by using the proposed hybrid approach, it is actually possible to recover the zig-zag fracture pattern, even if a completely homogenous mesh and material definition is used. The main influencing factors are the structural tensor, which forces the geometric phase field evolution to stay on planes perpendicular to the crack normal direction, and considering the driving stresses on the fictitious crack face for each likely crack orientation. This will further be elaborated at the end of this section, where the influence of the hybrid approach on the appearance of this pattern is discussed.

Comparing Figures 3.7 (a) and (c) it becomes obvious that phase field d_2 (green) has a stronger tendency to follow the prescribed fiber orientation than phase field d_1 (red). This result suggests that even without explicitly defining a weak interface in-between fibers, cracks perpendicular to the a_2-direction (Figure 3.5)

are influenced by an effect that has a similar impact as a weak interface. Nevertheless, the cracks do not exactly follow the fiber direction and the stronger the incline is, the stronger the tendency away from this fracture plane. Theoretically, by increasing the structural tensor scale, one could increase the affinity to this plane, however, closer to the edge of the plate, mixed fracture modes, for example for the 72° and the 80° model, cause a rather strong deviation.
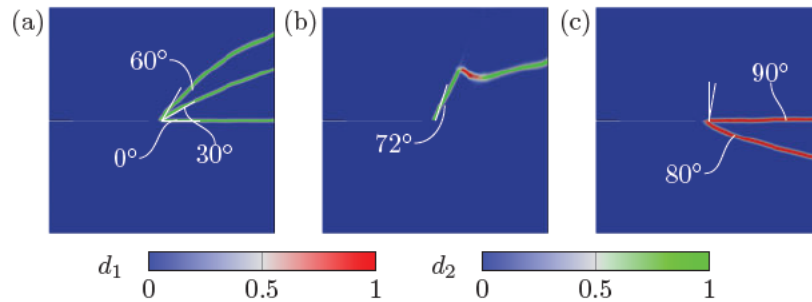

Fig. 3.7: Transition of failure modes with increasing fiber incline. Similar failure mechanisms are plotted above each other, i.e., **(a)** shows three different simulations. **(a)** shows only phase field d_2, i.e., a crack that propagates along the fiber, **(b)** shows the interaction of phase field d_1 and d_2, i.e., cracks that propagates along and perpendicular to the fiber **(c)** shows only phase field d_1, i.e., a crack that propagates perpendicular to the fiber.

For the fiber angles shown in Figure 3.7 (a) and (c), the results of the hybrid approach and the consistent approach agree. The main difference appeared for the 72° case shown in Figure 3.7 (b). In case of the consistent approach, no interaction occurred, meaning that the zig-zag pattern could not be reproduced (see the final state of the phase field in Figure 3.8). The hybrid and the consistent approach differ in how the solid material is degraded, which influences the stress distribution and, thus, the crack driving forces.

To take a close look at these differences, a state prior to the fully developed phase field is compared in Figure 3.8. Of primary interest are the stress components which only contribute to the development of one phase field, either d_1 or d_2, which for this quasi two-dimensional example are the Mode-I stresses, i.e., σ_{LL} for d_1 and σ_{RR} for d_2. As σ_{RR} is degraded in both approaches, the main difference is in σ_{LL}. Looking at the stress plot in Figure 3.8, there is actually a notable difference between the hybrid and the consistent approach. In the consistent approach the longitudinal stresses are not degraded, thus peaking at the geometrical crack tip from the single edge notched plate. For the hybrid approach, with the longitudinal stresses being fully degraded, the stress peak moves with the diffuse phase field crack tip, causing a stress state at this location, which favors the evolution of phase field d_1. This is an important finding, because it clearly shows that the usage of the hybrid approach is required in order to recover a zig-zag pattern.
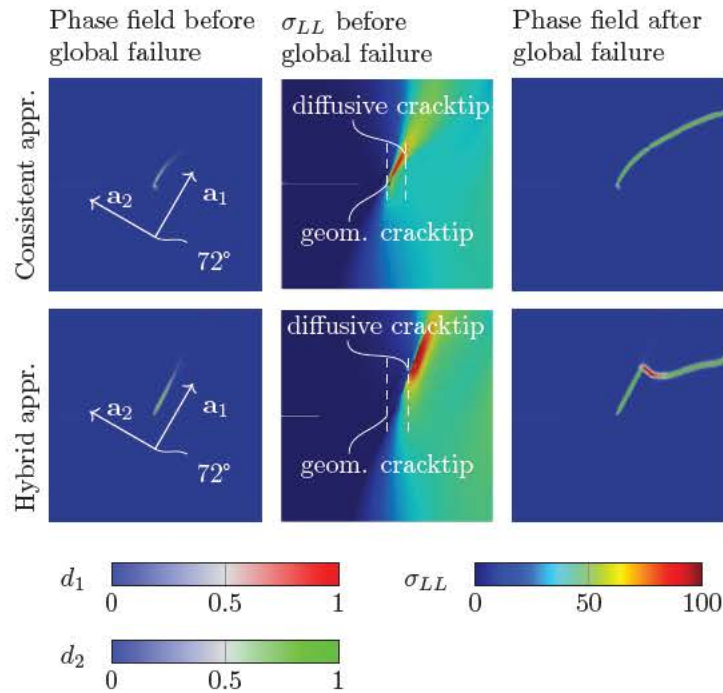
Fig. 3.8: Comparison of the hybrid and the consistent approach for two states, one prior to the fully developed phase field and one for the fully developed field. The figure shows the main difference in the Mode-I stresses for phase field d_1 ($\boldsymbol{\sigma}_{LL}$) which leads to the zig-zag pattern for a 72° fiber incline in case of the hybrid approach. Stresses are given in MPa.

3.3.2 Comparison of the hybrid approach and the consistent approach

While Figure 3.8 gives a strong argument in favor of the hybrid approach, it is still of interest, which of the two approaches is closer to modeling an actual discrete crack. Therefore, results of both methods are compared with the resulting stress distribution and deformation of a model with a discretely modeled predefined crack. The two different approaches, including a crack with a kink of 60°, are shown in Figure 3.9. To properly compare the two cases, a discrete crack is modeled, and the same crack is modeled by solving the phase field problem for a Dirichlet-type boundary condition, prescribing $d_2 = 1$ on the same region. Both cracks follow the fiber incline of 60°. Subsequently, a linear elastic simulation for the model with the discrete crack and a simulation of the deformation problem considering the phase field distribution from Figure 3.9, using the hybrid and the consistent approach, was conducted. For all three models the vertical deformation at the top edge is set to $u_{\mathrm{y}} = 0.1$.
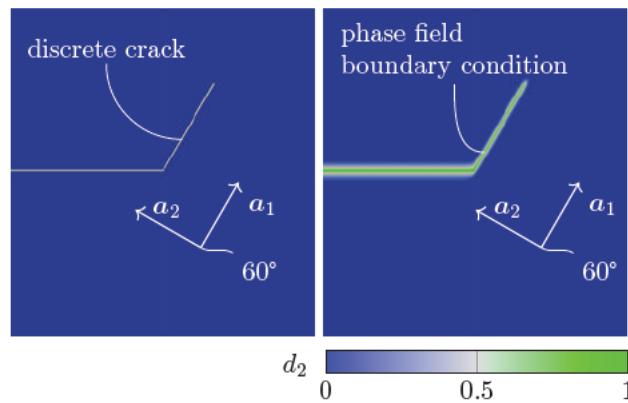
Fig. 3.9: Two different approaches to compare a phase field crack with a geometrically modeled, discrete crack. The phase field crack is computed by prescribing the Dirichlet-type boundary condition $d_2 = 1$ on the same region as the discrete crack is defined.

First, the deformation state of the three models is compared. The results are shown in Figure 3.10, where only the outer edges of each of the notched plates are depicted. Clearly, as the hybrid approach degrades all elastic components, it resembles the solution of the discrete crack model very well. In contrast, in the case of the consistent approach, the remaining stresses related to phase field d_1 result in a quite large deviation from the discrete crack solution.
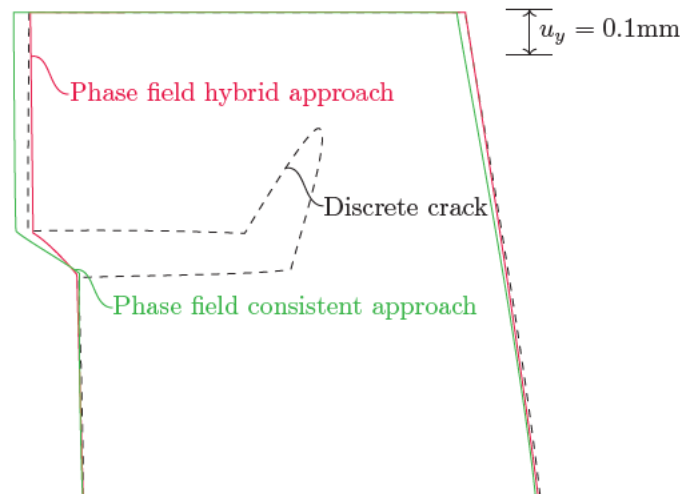
Fig. 3.10: Comparison of the deformation of the outer edges of a model with a discrete crack and two phase field models, using the hybrid approach and the consistent approach.

Figure 3.11 shows a comparison of stress distributions for the – essentially two-dimensional – notched plate. As expected, the main differences between the three models occur for stress components related to the longitudinal direction (σ_{LL} and σ_{LR}), as those are not fully degraded in the consistent approach. Figure 3.11, region ① shows that while the specimen is cracked at the given location, there are still stresses transferred through the crack. Neither the hybrid approach, nor the model with the discrete crack show longitudinal stresses in this region. Furthermore, this behavior also affects regions away from the crack, e.g., in region ②. The influence on the remaining stress components is marginal, as σ_{RR} and σ_{LR} are fully degraded in both cases. Nevertheless, in region ③, the consistent approach shows a peak in shear stresses at the kink which is considerably smaller at the other two models.
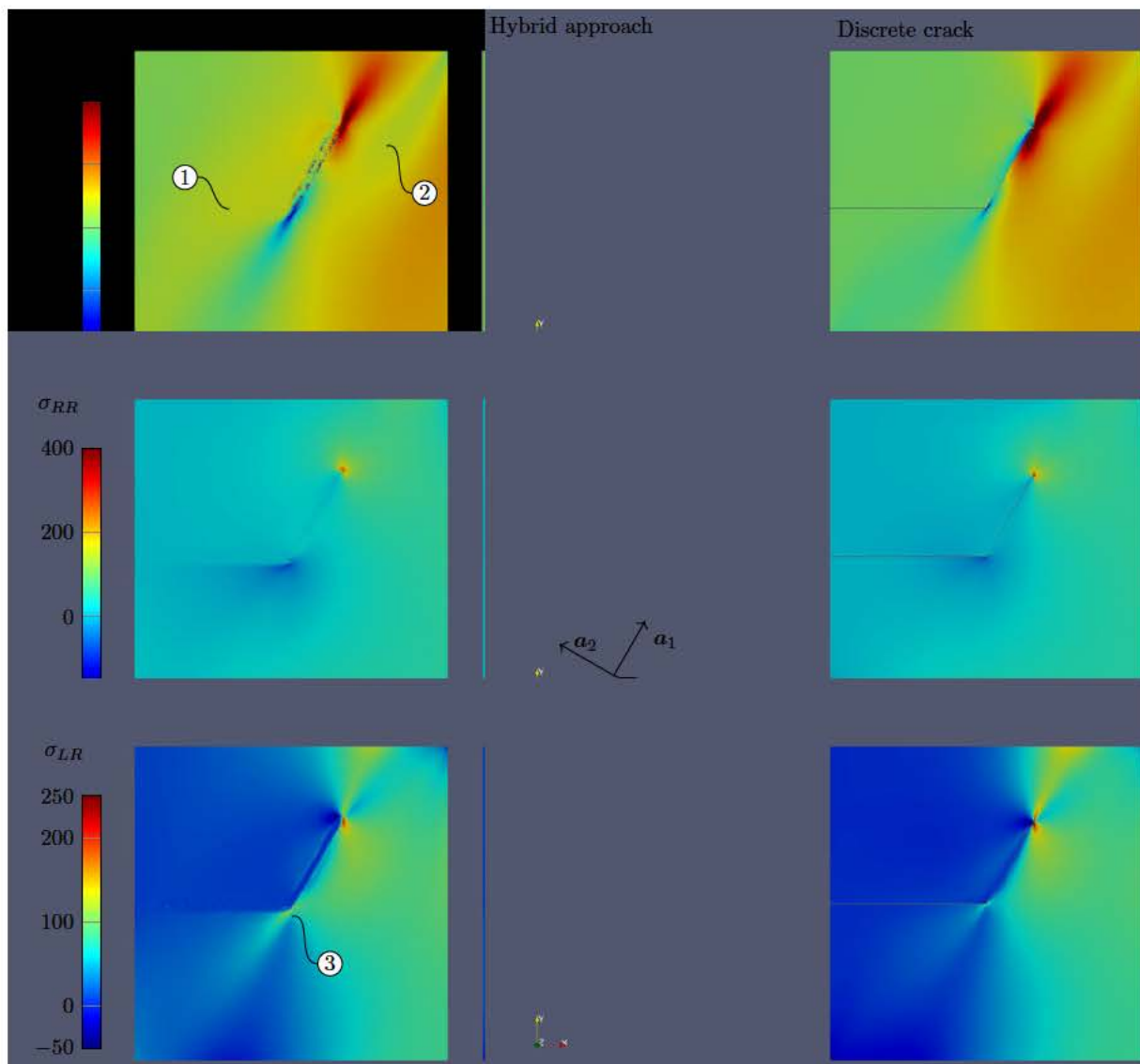
Fig. 3.11: Comparison of three stress distributions between the consistent approach and the hybrid approach using a predefined phase field distribution and a discrete crack model. ① shows that longitudinal stresses are still transferred through the crack when using the consistent approach and ② shows that this does not only affect the region of the crack but also regions further away. ③ shows a peak in shear stresses at the kink, when using the consistent approach. Stresses are given in MPa.

Given the similarities of the stress distributions and deformation states, and the hybrid approach's ability to reproduce the zig-zag failure patter found in wood, the results give clear support for using the hybrid approach over the consistent one, when modeling complex material failure.

3.3.3 Wooden board with a knot

Figure 3.12 shows the geometry of the wooden board with a single knot. The board is supported both at the top and the right face. The load is applied in form of a prescribed deformation along the bottom left edge. In order to control crack initiation, the board has a 10 mm notch through the specimen.

The fiber orientation a_1 (longitudinal), a_2 (radial), a_3 (tangential), is computed for each individual integration point and defines the local material directions. In this work, the model from Lukacevic et al.

[84] is used, where a knot is represented by a rotationally symmetric cone and wood fibers are streamlines flowing around an obstacle, which is the knot. Consequently, the fiber orientation in the LT-plane can be computed using the so-called *Rankine* oval, which describes the fluid flow around an elliptical object. Additionally, as fibers are situated on so-called growth surfaces, which motivate the cylindrical coordinate system commonly used to describe the elastic properties of wood, the third dimension of the fiber direction vector, the so-called dive angle, can be computed by restricting it to be orthogonal to the LT-plane. Figure 3.12 also shows a rendering of the fiber course. The texture is generated based on the previously computed fiber directions on a 0.10mm grid in the mid-plane of the board.

Similar to the notched plate from Section 3.3.1, the mesh size is homogenous in the left part of the specimen, where the crack will open. Restricting phase field evolution just to the left part reduces the number of DOFs and keeping the mesh homogenous reduces the influence of the mesh structure on the crack paths. The characteristic length of the elements in the phase field activated region is set to 0.75mm. Relative to the volume of this region, this matches the mesh density of notched plate model number 6 in Figure 3.6, which is in good agreement with the results from an even smaller characteristic length. The resulting total number of DOFs is $976,200$. As outlined in Section 3.3.2, the hybrid approach is required for properly modeling fracture processes of wood. Therefore, for simulation of this more complex example, only the hybrid approach is used. The parameters controlling the phase field problem are given in Table 3.2.
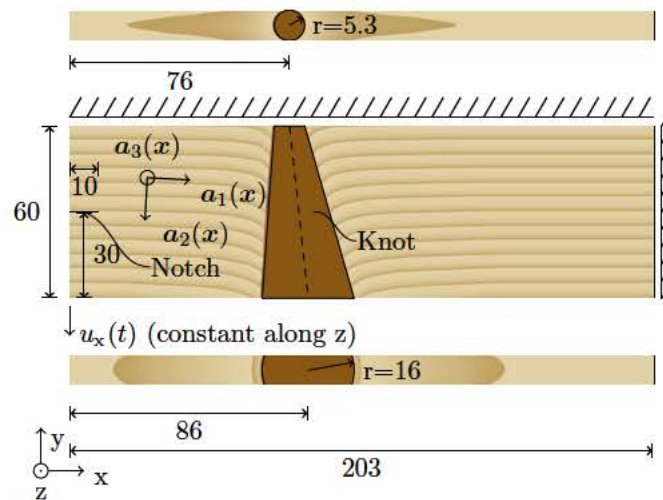

Fig. 3.12: Geometry of the wooden board with a single knot. The fiber orientation a_1 (longitudinal), a_2 (radial), a_3 (tangential) is prescribed in each integration point and is rendered in the mid-plane of the board. A notch is placed in order to control crack initiation. The board is loaded at the bottom left edge by prescribing the deformation. All measurements are in mm.

Tab. 3.2: Defining parameters for the wooden board with a single knot.

d_i	$\beta_i{}^{a}$	$G_{c,i}{}^{b}$	$f_{t,i}{}^{c}$	l_i/l_{eff}
d_1	2.0	2.0	80.0	2.0
d_2	4.0	0.8	5.0	2.0
d_3	2.0	0.1	3.6	2.0

[a] Structural tensor scale in Equation (4.3)   [b] in Nmm/mm^2 [c] in MPa

Figure 3.13 shows the resulting crack path when the specimen is almost fully cracked. Phase field d_2 is visualized using three-dimensional contour lines ranging from $d_2 = 0.0$ to $d_2 = 1.0$ in increments of 0.1. The fiber direction is depicted by plotting $\boldsymbol{a}_1$ on a uniformly spatially distributed subset of integration points. Obviously, the varying fiber directions influence the orientation of the crack face. Figure 3.14 shows the evolution of the phase field variable d_2. The crack initially starts with a slight decline and changes its orientation in the vicinity of the knot, where the fibers become parallel to the knot's surface. When reaching the knot, the crack kinks and follows the weak interface. It stops propagating close to the lower edge of the board, as the compressive Mode-I stresses in this region do not result in crack driving forces, due to the additive decomposition of the strain energy density term.
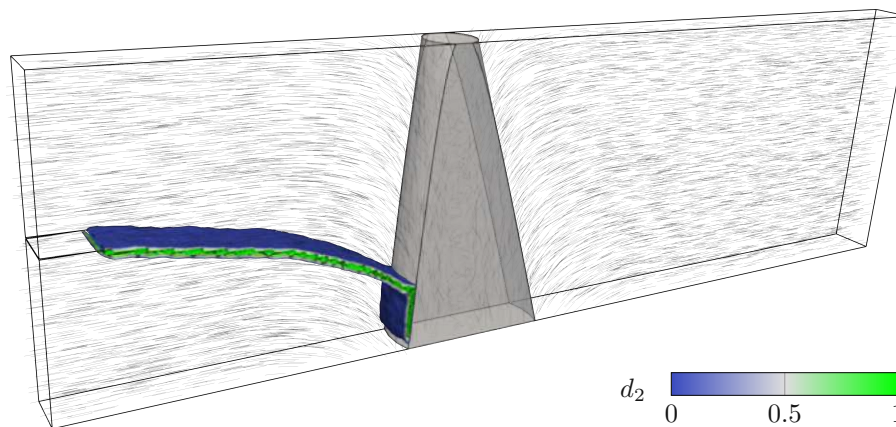

Fig. 3.13: Fully cracked wooden board. The fiber orientation vector $\boldsymbol{a}_1$ is plotted on a uniformly spatially distributed subset of the integration points. The crack mostly follows the fiber direction, starting horizontally, tilts and subsequently propagates along the interface region between the clear wood area and the knot.

Figure 3.14 shows the load-deflection plot of the simulation, measured at the lower left edge of the board. The horizontal axis is split into two differently scaled parts, as the change in the reaction force from 0 mm to 3 mm is quite large compared to the change from 10 mm to 30 mm. Past the initial opening of the crack, the load-deflection plot shows a cohesive behavior during further crack propagation. The softening effect can be controlled by properly setting $f_{t,i}$ and $G_{c,i}$ in Equation (4.7). The reaction force is heavily reduced while the crack propagates along the fiber towards the knot. With the crack further progressing, tensile and compressive stresses, similar to the bending stresses at the clamped end of a cantilever beam, concentrate at the lower left edge of the knot. This shift in the stress distribution results in a less stiff response of the system, therefore, larger deformations are required for further crack growth along the weak interface between the clear wood area and the knot.
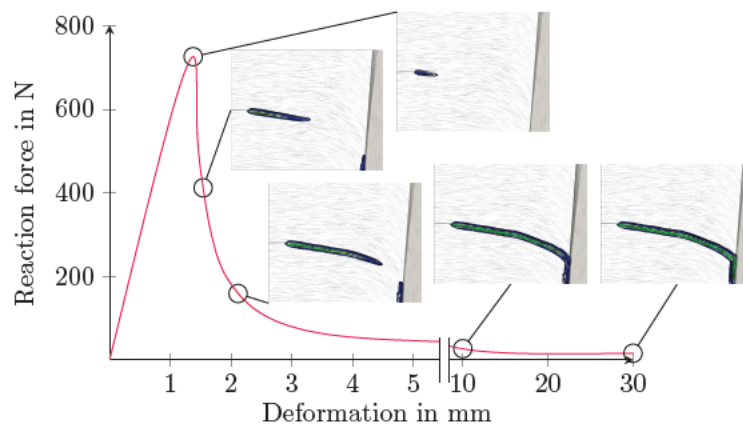
Fig. 3.14: Load-deflection plot measured at the lower left edge of the board. Additionally, the evolution of the phase field variable d_2 is shown for multiple locations along the path.

The simulation of a more complex model considering a realistic fiber course showed that the discussed phase field model is capable of considering the effects resulting from fiber deviations and that sudden changes in the crack face orientation, e.g., the kink when the crack reaches the knot, can be modeled. Furthermore, using the unified phase field theory, adapted to a linear softening law, allows for a cohesive behavior during crack propagation.

3.4 Conclusion and Outlook

The present work addresses the formulation of a phase field model for orthotropic non-brittle materials, able to reproduce multiple, very different failure mechanisms. In order to extend the phase field method for fracture to support cohesive behavior, the so-called unified phase field theory is applied and tuned to a linear softening law, resembling a cohesive zones model. Subsequently, a stress-based split for anisotropic materials is derived, which is based on considering Mode-I, Mode-II and Mode-III crack driving stresses on a fictitious crack plane. The plane's orientations are defined accordingly to material specific fracture planes, in this case for wood: a crack plane perpendicular to the longitudinal, the radial and the tangential direction. The orientation in which crack growth results in the largest energy dissipation is the driving failure mechanism.

This formulation is coupled in form of a hybrid approach, by separating the energetic driving force term and the actual degradation of the solid. In this novel hybrid approach, a smooth traction-free crack boundary condition is used, which incorporates a contact constraint and, thus, does not require an additional constraint for preventing interpenetration of crack faces. This concept is then put into a multi-phase field model, which allows defining a different fracture behavior for each phase field variable individually. Therefore, very different failure mechanisms can be modeled and described realistically. In order to consider the effect of the material's structure on the crack paths, a second-order tensor is added to the crack density function, which scales the phase field's gradient on the plane perpendicular to the associated crack orientation vector. Hence, preferable planes for crack propagation can be defined, e.g., a crack perpendicular to the radial direction is likely to propagate along the fiber direction (longitudinal) and less likely to propagate in the radial direction, due to the weak interface between the fibers and the matrix.

The outlined method is tested using two numerical examples of different complexity, both being wooden specimens. By means of the model of a sinlge edge notched plate, it is shown that changing the fiber orientation leads to different crack topologies, where cracks travel along the fiber when the load direction

is in an obtuse angle relative to the fiber direction. At a certain fiber incline, as expected, the crack kinks and jumps to the next fictitious growth layer, rupturing the fibers in between. At a sharp angle, the failure mode changes to a crack perpendicular to the fiber orientation. The simulations showed that such common phenomena of wood (e.g., the zig-zag pattern) cannot be recovered when a variationally consistent approach is used, thus motivating the use of the hybrid approach with a smooth traction free crack boundary condition. Subsequently, a more complex example of a wooden board with a single knot and a spatially varying fiber orientation was tested. The model shows that the phase field crack actually follows the curvature of the wood fibers and also allows for sudden changes in the crack face orientation, e.g., in the vicinity of the knot where the crack kinks. Furthermore, the influence of the cohesive behavior during crack propagation can be observed.

This allows the conclusion that the phase field method can be used to model wood failure, as crack phenomena like the zig-zag pattern can be modeled, complex crack topologies can be depicted and cohesive behavior can be considered. An apparent limitation of this work lies in the formulation of the energetic driving force, which, while allowing the definition of a different fracture characteristic on the level of each phase field variable, allows no distinction between Mode-I, Mode-II and Mode-III. Thus, always mixed mode failure is assumed. As this study's focus is on the implementation of a phase field model for wood and investigation of commonly found crack patterns, future research on validating the model with experimental data is needed. Furthermore, examining more complex examples like wooden boards with multiple knots is of interest.

Acknowledgement

3.A Comparison of the active set reduced space method and the primal-dual active set method

The only difference between the active set reduced space method from [149], and the primal-dual active set method from Heister et al. [61], is in the selection of the active and the inactive set. Generally speaking, whether a phase field DOF is in the active or the inactive set, is determined by two aspects, the current value of the phase field and the current value of the residual. Adaption to the notation used in this work and rearranging the parts in the primal-dual active set formulation, leads to the following definition of the primal-dual active set:

$$\mathcal{A}(\hat{\boldsymbol{d}}_{n+1}^k) = \left\{ i \in \mathcal{S} \,\middle|\, c\mathbf{B}_{ii}\left(\hat{\boldsymbol{d}}^{k-1} - \hat{\boldsymbol{d}}_{n+1}^k\right)_i + (\hat{\boldsymbol{R}}_{\hat{\boldsymbol{d}},n+1}^k)_i > 0 \right\}, \tag{3.30}$$

where c is a constant larger than 0 and $\mathbf{B}_{ii}$ is the entry of the i-th DOF in the diagonal mass matrix $\mathbf{B}$. Given that both c and the mass are strictly larger than 0, their product is as well. Comparing the two approaches from Equations (3.27) and (3.30) leads to the following observations:

- If both $\left(\hat{\boldsymbol{d}}^{k-1} - \hat{\boldsymbol{d}}_{n+1}^k\right)_i$ and $(\hat{\boldsymbol{R}}_{\hat{\boldsymbol{d}},n+1}^k)_i$ are larger than 0, the i-th DOF is in both formulations considered to be active.

- If both $\left(\hat{\boldsymbol{d}}^{k-1} - \hat{\boldsymbol{d}}_{n+1}^k\right)_i$ and $(\hat{\boldsymbol{R}}_{\hat{\boldsymbol{d}},n+1}^k)_i$ are smaller than 0, the i-th DOF is in both formulations considered to be inactive.

- If the sign of the two terms is different, the i-th DOF is inactive in the method from Yang et al. [149], however, in the method from Heister et al. [61] it depends on the choice of the constant c, which is not further elaborated in their work.

Publication 4

Validation of a hybrid multi-phase field model for cohesive failure in orthotropic materials on experimental studies

Authors   Sebastian Pech, Markus Lukacevic, Josef Füssl

Under review at *Engineering Structures*

Abstract

Fracture mechanics simulations are a crucial component for understanding failure of wood. They are required for explaining numerous effects occurring prior to crack initiation and during crack propagation. The microstructure of wood has a strong influence on its mechanical properties, e.g., an orthotropic constitutive behavior, a quasi-brittle response and favorable crack propagation directions due to weak principal material directions. For properly covering those effects, a careful selection of numerical methods is required. In particular, the occurrence of complex crack topologies poses a challenge, as many modeling approaches rely on predefined crack paths or are subject to inherent geometrical limitations. Therefore, in this work, the phase field method for fracture is applied, which can account for the aforementioned requirements. Particularly, a hybrid multi-phase field model, supporting cohesive failure in orthotropic materials, is used and validated with multiple experimental studies. We show that the model produces results in good agreement with the investigated experiments, both in the response graphs and the occurring cracks. A quantity of particular interest is the scale factor on the structural tensor, which accounts for penalizing unlikely crack propagation directions. It is, certainly, a material specific value, but was never quantified for wood. By matching the formed cracks to the experimental results, it was possible to find, at least, a lower bound for this value. Besides this finding, the determined tensile strengths and fracture energy release rates are withing a reasonable range for wood, and it was possible to transfer model parameters tuned for a specific test to another test, with the results still being in quite good agreement with the experimental study. Those findings allow application of this model to more complex situations like wooden boards with multiple knots and complex fiber courses, and show that the model's input parameters are not purely numerical values but rather material specific parameters which can be, once tuned for a material, applied to different structural designs.

4.1 Introduction

Usage of fracture mechanics modeling approaches is crucial in applied engineering. The ability to realistically describe failure processes of structures and components enables their optimization in terms of design and material consumption while ensuring high-reliability standards. Simulation of failure processes has been the subject of numerous publications over the past decades and remains an area of very intensive research due to the complexity of possible material failure mechanisms.

A building material with especially complex failure mechanisms is wood. During growth, wood is optimized to withstand the harsh conditions a tree is exposed to. The so formed microstructure gives the material excellent load-bearing capabilities while at the same time maintaining a low density. This makes it ideal for high-performance structures. Besides beneficial mechanical properties, its desirable effect on carbon dioxide emissions is an essential driving factor for its increasing popularity. Considering the whole life cycle, it removes carbon dioxide from the atmosphere rather than adding more, which is the case for e.g., concrete or steel. Nevertheless, to be competitive in this industry, sound, resource-efficient, and optimal usage are indispensable. Therefore, a good understanding of the complex material behavior is necessary, which, however, is a challenging task and requires a careful selection of numerical methods. In particular, fracture mechanics modeling is of interest when it comes to simulation of wood failure, as it is necessary for explaining phenomena before crack initiation and during crack propagation [127].

The basis of most studies on brittle fracture processes is the work of Griffith and Taylor [54], which describes fracture in terms of a critical fracture energy release rate required for crack propagation. Irwin [67] introduced the so-called stress intensity factors, based on the work of Griffith, to characterize stress fields around the crack tip as a function of geometry and loading. While these linear elastic fracture mechanics theories can be applied to describe the crack propagation of existing cracks, effects such as crack kinking, branching, coalescence, initiation, and cohesive behavior are not considered. With the widespread establishment of finite element methods for continuum mechanics problems, new methods for simulating fracture processes emerged: Approaches based on remeshing and the use of special crack tip elements [12, 122], the node split method [106], cohesive elements and cohesive zone models [11, 110] and XFEM [92]. These methods allow overcoming some of the previously mentioned limitations of the theories based on Griffith's work; however, each approach has its weaknesses.

One of the most recent and promising methods is the so-called phase field method for fracture. This method was initially proposed by Francfort and Marigo [48] and is also based on Griffith's theory of brittle fracture but is formulated by a variational approach minimizing the total energy of the system. The main advantage is that no predefined crack paths are required and that complex fracture phenomena like branching and coalescence are naturally accounted for. In Bourdin et al. [20] and Bourdin et al. [21], a regularization method was introduced, allowing solving the problem in a numerically efficient way. By introducing an auxiliary field $d(x) \in [0, 1]$ – the so-called crack phase field – the crack discontinuity is modeled by including a smooth transition zone from the intact ($d = 0$) to the cracked ($d = 1$) solid. The length scale parameter controls the width of the regularization zone. When this parameter approaches zero (i.e., recovery of the discontinuous transition from solid to crack), the solution Γ-converges to Griffith's theory.

By expressing cracks in terms of a field variable, the complex crack phenomena arise naturally from the defining system of differential equations. Thus, the phase field method theoretically allows crack topologies of arbitrary complexity, limited only by the mesh size and mesh structure. This motivates the application of the phase field method to materials with a complex micro- or macrostructure, such as wood. For these materials, the micro- and macrostructure strongly influence both the elastic behavior in terms of anisotropic constitutive relationships and the crack topology by introducing favorable fracture planes due to weak principal material directions.

Fracture processes of wood are driven by properties on multiple length scale levels, leading to a quasi-brittle behavior, where most failure phenomena happen after crack initiation. This results in tensile strength as the only criterion for failure, giving, at best, the point of crack initiation but never being sufficient for simulating the whole fracture process. In wood, crack growth starts on the microscopic level from defects in the cell wall material. This induces the often observed decline in linear elastic stiffness visible in the load-deflection graph (i.e., the non-linear behavior before reaching the peak load). Close to the actual peak load, the microscopic cracks localize, and the actual crack and fracture process zone form. After crack initiation, toughening effects at the crack tip set-in which are mostly related to so-called fiber bridging [38, 134]. Those effects in the fracture process zone cannot be captured by linear elastic fracture mechanics (the process zone is assumed to be of size 0); therefore, non-linear fracture mechanic theories are required [13].

The literature on applying the phase field method to wood is very sparse. In Carlsson and Isaksson [23] dynamic crack growth of a wood-composite material with 20% pulp wood fibers and 80% polylactic acid matrix material was researched. Research on fracture processes of natural wood was conducted in Carlsson and Isaksson [24] on the microscopic scale. To the authors' knowledge, no publications exist dealing with fracture processes on the clear-wood scale considering a homogenous body with an orthotropic behavior. Therefore, the herein performed validation of the authors' proposed model [105] for considering orthotropic constitutive behavior, anisotropic crack propagation, and quasi-brittle behavior of wood on a macroscopic scale is an essential contribution to the research of wood fracture mechanics using the phase field method.

This publication is structured as follows: The initially proposed phase field model for wood is briefly explained in Section 4.2 and, additionally, an improvement of the solver is discussed, enabling to perform the computationally costly simulations presented in Section 4.3. The latter sections contain the main contributions of this work, namely, the validation of this phase field model by simulation of experimental investigations of two single edge notched beam (SENB) three-point bending tests, a double cantilever beam (DCB) test, and an end notched beam (ENB) test. The paper closes with a discussion and comparison of the findings and gives an outlook on future applications and further improvements of the proposed algorithm.
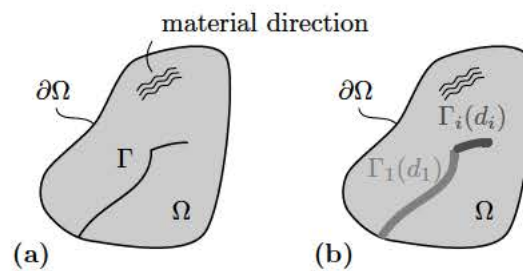
4.2 Fundamentals and Methods

Fig. 4.1: (a) sharp and (b) diffuse representation of a crack topology. Within the diffuse representation, the sharp crack Γ in the body Ω is approximated using multiple diffuse crack fields, which depend on the crack phase fields $\boldsymbol{d}$.

This work uses our phase field model for orthotropic materials with preferable fracture planes. The model is briefly described here, the interested reader is referred to the detailed explanation in Pech et al. [105]. Fundamentally, this model is based on the unified phase field model from Wu and Nguyen [145] and

takes multiple phase field variables [15] into account. Excluding body forces and surface traction, the regularized form of the total energy Π of the system, defined on the domain Ω, thus reads:

$$\Pi(\boldsymbol{u}, \boldsymbol{d}) = \int_\Omega \left[\psi^+(\boldsymbol{u}, \boldsymbol{d}) + \psi^-(\boldsymbol{u}) \right] d\Omega + \sum_i^n G_{c,i} \int_\Omega \gamma_i(d_i) d\Omega, \tag{4.1}$$

where i denotes the i-th phase field, $\boldsymbol{u}$ the displacement field, $\boldsymbol{d}$ the phase field of dimensionality n, $G_{c,i}$ the critical energy release rate and γ_i the regularized crack surface density functional that approximates the sharp crack surface. The strain energy density ψ is herein additively decomposed into a part depending on the phase field $\boldsymbol{d}$ and the deformation field $\boldsymbol{u}$ and one just depending on the deformation field $\boldsymbol{u}$. They are referred to as crack driving strain energy and passive strain energy, respectively. This decomposition is required in order to obtain a realistic fracture behavior, like no interpenetration of crack faces or no crack growth under pure compressive stress states.

For considering structural anisotropy the crack surface density function used in the unified phase field theory is enhanced with a second order tensor $\boldsymbol{A}_i$ [96, 132]:

$$\gamma_i(d_i) = \frac{1}{c_{0,i}} \left[\frac{1}{l_i}\alpha(d_i) + l_i \nabla d_i \boldsymbol{A}_i \nabla d_i \right] \text{ with } c_{0,i} = 4 \int_0^1 \sqrt{\alpha(\zeta)} d\zeta. \tag{4.2}$$

The tensor $\boldsymbol{A}_i$, often referred to as "structural tensor", adds preferable or invalid crack propagation directions by scaling the gradient term of the phase field. In a multi-phase field setting, the definition

$$\boldsymbol{A}_i = \boldsymbol{I} + \beta_i \left(\boldsymbol{I} - \boldsymbol{a}_i \otimes \boldsymbol{a}_i \right) \tag{4.3}$$

from Nguyen et al. [96] can be used, which allows assigning material directions $\boldsymbol{a}_i$ and penalty factors β_i for penalizing planes not orthogonal to the material directions for each phase field variable d_i. For $\beta_i = 0$, the standard isotropic formulation of the crack surface density functional is recovered.

The two functions that mainly influence the fracture process are the degradation function $\omega(d_i)$ and the local part of the dissipated fracture energy $\alpha(d_i)$. A general expression for those two functions is given by Wu [142], in the following way

$$\alpha_i(d_i) = \xi d_i + (1-\xi)d_i^2 \quad \forall d_i \in [0,1] \ \xi \in [0,2] \text{ and} \tag{4.4}$$

$$\omega_i(d_i) = \frac{(1-d_i)^p}{(1-d_i)^p + Q(d_i)} \quad p \geq 2 \tag{4.5}$$

$$Q_i(d_i) = a_{1,i}d_i + a_{1,i}a_{2,i}d_i^2 + a_{1,i}a_{2,i}a_{3,i}d_i^3, \tag{4.6}$$

where $a_{1,i}$, $a_{2,i}$ and $a_{3,i}$ are coefficients that can be calibrated to model a certain cohesive behavior related to the i-th phase field. In this work, the coefficients are tuned to match a linear softening law. Based on the analytical solution of a one-dimensional bar problem, Wu [142] thus gives the following definitions:

$$a_{1,i} = \frac{4}{\pi} \frac{l_{ch,i}}{l_i}, \ a_{2,i} = -\frac{1}{2} \text{ and } a_{3,i} = 0, \tag{4.7}$$

for $\xi = 2$ and $p = 2$, in Equations (4.4) and (4.5), respectively. $l_{ch,i}$ defines *Irwin*'s characteristic length, given as $l_{ch,i} = {}^{E_{0,i}G_{c,i}}/f_{t,i}^2$, for the i-th phase field, and l_i is the length scale parameter for the i-th phase field, which is chosen to be larger than the effective element size l_{eff}.
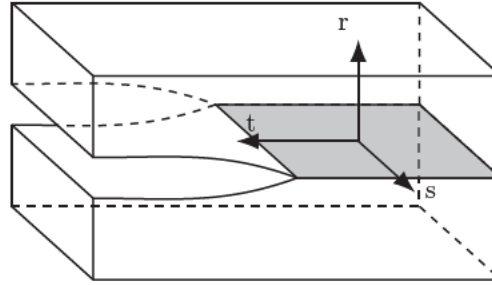
4.2.1 Strain energy decomposition

Fig. 4.2: Crack coordinate system of a fictitious crack surface, required to identify Mode-I, Mode-II and Mode-III crack driving forces.

As outlined above, the decomposition of the strain energy is required for assuring a realistic fracture behavior. In this work, we rely on a stress-based decomposition [132], that considers Mode-I, Mode-II and Mode-III crack driving forces in a crack coordinate system defined on a fictitious crack surface (Figure 4.2). The original isotropic decomposition was enhanced in Pech et al. [105] to cover orthotropic materials. Fundamentally, in a stress-based split, only the stress field is additively decomposed, such that the total strain energy density reads:

$$\psi = \frac{1}{2}(\underbrace{\boldsymbol{\sigma}^+ : \varepsilon}_{\psi^+} + \underbrace{\boldsymbol{\sigma}^- : \varepsilon}_{\psi^-}). \tag{4.8}$$

The crack driving stresses $\boldsymbol{\sigma}^+$ and the passive stresses $\boldsymbol{\sigma}^-$ are identified by first projecting the stress tensor into the crack coordinate system, leading to stress field components $\sigma_{ij} = \boldsymbol{\sigma} : (i \otimes j)$ for $(i, j) \in \{(r, s, t) \times (r, s, t)\}$, where r, s and t are the base vectors of the crack coordinate system (Figure 4.2). The projected stress field components can now be separated according to the classic fracture mechanics Modes-I, II and II. For an orthotropic constitutive law, the driving and passive stress tensors read:

$$\boldsymbol{\sigma}^+ = \langle \sigma_{rr} \rangle_+ (r \otimes r) + \sigma_{rt} + \sigma_{tr} + \sigma_{rs} + \sigma_{sr} + \frac{\langle \sigma_{rr} \rangle_+}{C_{rrrr}} \big[C_{ssrr}(s \otimes s) +$$
$$+ C_{ttrr}(t \otimes t) + C_{rtrr}(r \otimes t) + C_{rsrr}(r \otimes s) + C_{trrr}(t \otimes r) + C_{srrr}(s \otimes r) + \tag{4.9}$$
$$+ C_{tsrr}(t \otimes s) + C_{strr}(s \otimes t) \big] \text{ and }$$

$$\boldsymbol{\sigma}^- = \langle \sigma_{rr} \rangle_- (r \otimes r) + \sigma_{tt} + \sigma_{ss} + \sigma_{ts} + \sigma_{st} - \frac{\langle \sigma_{rr} \rangle_+}{C_{rrrr}} \big[C_{ssrr}(s \otimes s) +$$
$$+ C_{ttrr}(t \otimes t) + C_{rtrr}(r \otimes t) + C_{rsrr}(r \otimes s) + C_{trrr}(t \otimes r) + C_{srrr}(s \otimes r) + \tag{4.10}$$
$$+ C_{tsrr}(t \otimes s) + C_{strr}(s \otimes t) \big],$$

where $\langle \bullet \rangle_+ = (\bullet + |\bullet|)/2$ and $\langle \bullet \rangle_- = (\bullet - |\bullet|)/2$ are *Macaulay* brackets, $\sigma_{ij} = \sigma_{ij}(i \otimes j)$ is the contribution to the stress tensor related to the i and j direction in the crack coordinate system and C_{ijkl} are the respective components of the elasticity tensor. Details on the motivation of Equations (4.9) and (4.10) are given in Pech et al. [105] and Teichtmeister et al. [132].

4.2.2 Crack boundary condition-based hybrid approach

The above outlined method can be used in a variationally consistent manner, where the strain energy decomposition not only defines the crack driving forces, but also the degradation of the solid. However, the observations in Pech et al. [105] clearly show that using the variationally consistent approach is not sufficient for recovering zig-zag patterns as shown in Figure 4.3. Instead, degradation is performed based on a traction-free, smooth crack boundary condition [66]. This is similar to the stress-based split outlined in Section 4.2.1, however, only normal compressive contact stresses are kept undegraded in order to prevent interpenetration of crack faces. Thus, fundamentally, the strain energy decomposition is considered as a contact problem, leading to the following decomposition of the stress tensor:

$$\boldsymbol{\sigma}^+ = \langle \sigma_{rr} \rangle_+ (\boldsymbol{r} \otimes \boldsymbol{r}) + \boldsymbol{\sigma}_{rt} + \boldsymbol{\sigma}_{tr} + \boldsymbol{\sigma}_{rs} + \boldsymbol{\sigma}_{sr} + \boldsymbol{\sigma}_{tt} + \boldsymbol{\sigma}_{ss} + \boldsymbol{\sigma}_{ts} + \boldsymbol{\sigma}_{st} \text{ and} \tag{4.11}$$

$$\boldsymbol{\sigma}^- = \langle \sigma_{rr} \rangle_- (\boldsymbol{r} \otimes \boldsymbol{r}), \tag{4.12}$$

where $\boldsymbol{r}$ is the crack face's normal vector (Figure 4.2).

4.2.3 Crack coordinate system for wood

Macroscopic crack propagation and crack initiation in wood is strongly influenced by the underlying microstructure of the material. Wood fibers, which were produced at the same time, lie on a so-called growth surfaces. Such growth surfaces give structure to the material and thus define the local material directions in a cylindrical coordinate system, where the longitudinal direction (L) points into the fiber direction, the radial direction (R) is normal to the growth surface and the tangential direction (T) is the vector perpendicular to both L and R.

As described by Smith et al. [127], there are two driving mechanisms observable in wood fracture:

- Cracks following the direction of least resistance, defined by the microstructure of the material.

- Cracks opening perpendicular to the largest principal stress, thus, leading to a maximum reduction of the total energy.

This results in the often observed zig-zag pattern, where cracks follow the path of maximum total energy reduction, until reaching a growth ring. At the growth ring, which is essentially a weak interface, the crack direction changes to the direction of least resistance, which for wood is always parallel to its fiber direction. So cracks are likely to follow the material's structure, i.e., for wood the LRT-coordinate system.
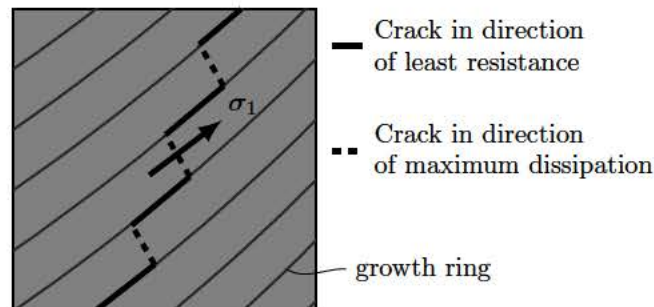

Fig. 4.3: Typical crack pattern observed for wood. A crack switches from following the direction of least resistance along the fiber, to the direction of maximum total energy reduction perpendicular to the largest principal stress. It changes its orientation again, when it hits the next growth ring. [127].

This effect imposes a strong limitation on occurring crack face orientations, thus considering predefined crack coordinate systems is plausible. Given the LRT-coordinate system, one can identify six different fracture orientations, relative to the wood growth axis: LR, LT, RL, RT, TL and RT, where the first letter specifies the crack face's normal vector and the second letter specifies the direction of crack extension. In practice, however, considering RL and TL is mostly sufficient [33] as cracks align with the natural cleavage planes along the fiber [127]. Nevertheless, herein, fiber rupture is also considered, resulting in three different crack coordinate systems ($\boldsymbol{r}_i$, $\boldsymbol{s}_i$, $\boldsymbol{t}_i$), for cracks opening perpendicular to the longitudinal ($i = 1$), the radial ($i = 2$) and the tangential direction ($i = 3$).

As the material's fracture toughness and strength for those three orientations also depend on the material's microstructure, the defining material parameters are very different. Therefore, each direction is considered as a separate phase field $\boldsymbol{d}_i$ in Equation (4.1). To further improve the efficiency of the algorithm, only one phase field is active at a time. The main driving failure mechanism (longitudinal, radial or tangential) is determined according to the principle of maximum dissipation i.e., the failure mode with the highest energy release is the main cause of failure. Thus, the strain energy terms $\psi^+(\boldsymbol{u}, \boldsymbol{d})$ and $\psi^-(\boldsymbol{u}, \boldsymbol{d})$ in Equation (4.1), are replaced by

$$\psi_i^+(\boldsymbol{u}, \boldsymbol{d}) = \omega_i(d_i)\psi_i^+(\boldsymbol{u}) \text{ and } \psi_i^-(\boldsymbol{u}) = \psi_i(\boldsymbol{u}) - \psi_i^+(\boldsymbol{u}), \tag{4.13}$$

respectively, where i is the index of the defining failure mode.
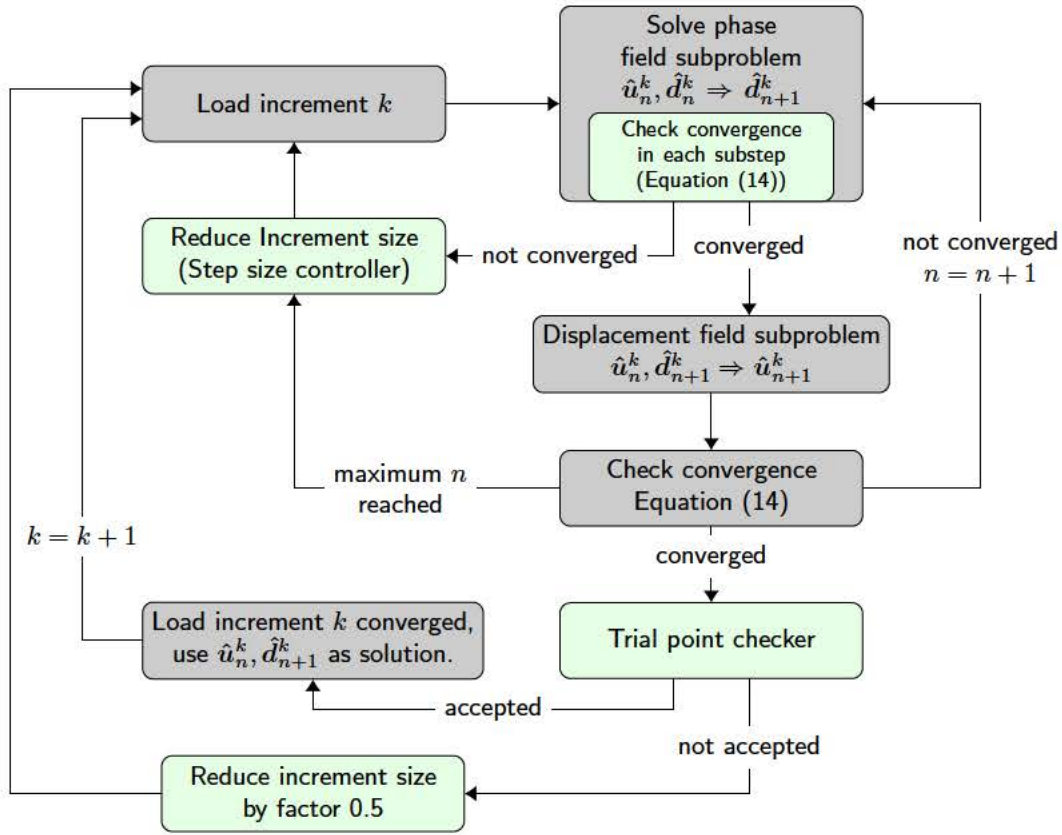
4.2.4 Solver

Fig. 4.4: Staggered solution process for a single load increment. Convergence is assured by imposing a limit on the size of the state variable's increment. In addition, each converged solution is validated by the trial point checker, which searches for sudden changes in the response graph and enforces increment size reductions.

A commonly used approach for solving the energy minimization problem involved in the phase field method for fracture is application of the so-called staggered approach or alternate minimization scheme [20, 89]. Herein, two separate problems, the deformation subproblem and the phase field subproblem are considered. In an alternating manner, one problem is solved, while the previously obtained solution for the other field is kept constant. The key advantage of this approach is that the subproblems are convex, which improves the robustness of the solution process [6]. The algorithmic scheme applied in this work is based on Pech et al. [105], however, due to the computational effort involved in simulating the investigated experimental studies, the method is enhanced to improve the solver's performance. The overall algorithm is depicted in Figure 4.4, where additions to the originally proposed method are highlighted in green. Convergence in an increment k is verified by

$$\frac{\left\|\hat{d}_{n+1}^k - \hat{d}_n^k\right\|}{\left\|\hat{d}_{n+1}^k\right\|} \leq \epsilon \text{ and } \frac{\left\|\hat{u}_{n+1}^k - \hat{u}_n^k\right\|}{\left\|\hat{u}_{n+1}^k\right\|} \leq \epsilon, \tag{4.14}$$

where $\|\bullet\|$ is the L^2-norm, $\hat{d}$ and $\hat{u}$ are the nodal values of the phase field and the deformation field, respectively, and ϵ is the error tolerance.

To ensure thermodynamical consistency, an irreversibility constraint on the phase field variable is required. As this work relies on the unified phase field theory [145], a box constrained solver is required on the phase field, limiting each nodal value to within the lower bound 0 and the upper bound 1. The constraint is applied on a global level using the so-called active set reduced space method [149]. In this method, two subsets of $\hat{\boldsymbol{d}}$ are identified separating the DOFs in to an active set and an inactive set. The constraint is enforced on the active set by application of Dirichlet-type boundary conditions.

The additions to the originally proposed algorithmic scheme deal with improvements of convergence and computational performance. The investigated simulations in this work showed that instead of computing a single phase field step, solving the phase field subproblem until convergence allows larger load increments. Furthermore, an auto-adaptive sub-stepping algorithm is used [58]. Here, a step size controller ensures that any reduction of load increments is always only as large as required and the so-called trial point checker guarantees that load increments are sufficiently small close to the peak load of the structure. Both approaches are explained in brief in the following sections, a detailed explanation can be found in the original work by Gupta et al. [58].

4.2.4.1 Trial pointer checker

During crack propagation, very small load increments are required to properly solve the phase field problem using the staggered approach. Contrarily, in an elastic loading phase, large increments are sufficient. While relying on very small load increments throughout the solving progress is computationally inefficient, maintaining a large increment size, results in state variables for which the phase field and the deformation field might converge, however, the results can actually be far off the correct solution. Therefore, in Gupta et al. [58] a so-called trial point checker algorithm is propsed, which performs an additional, however, very small load increment step, after a converged solution (trial state) was found. As this additional step is very small, a single staggered iteration for each of the subproblems is sufficient. Evaluating the slope of the strain energy for the trial state and the additional step allows detecting critical states during the iteration (i.e., before and after strong nonlinearities usually close to local extrema in the response graph):

- For equal slope directions, the trial solution is accepted as no local maxima were detected.

- If the trial solution has a positive slope and the additional step a negative one, it is likely that the load increment is in the vicinity of a strain energy peak. Therefore, to properly resolve this peak, smaller load increments are required. Thus, the trial state is rejected and the load increment size reduced.

- If the trial solution has a negative slope and the additional step a positive one, it is likely that the load increment is after a peak in the strain energy. Therefore, to maintain computational performance, the increment size is increased to the maximum allowed size and the trial state is accepted.

4.2.4.2 Step size controller

The step size controller is similarly motivated as the trial point checker: Maintaining a large time increment size to be performant and reducing the time increment size if necessary, for capturing sudden changes in the material's response. In an adaptive stepping algorithm an error estimator (Equation (4.14)) is computed for each found solution. If a solution has an error below a given threshold, the solution is accepted, otherwise, further iterations are performed or, if the limit on maximum iterations was reached, the time step is reduced. Recent literature contains various methods for adaptive stepping schemes, like changing the time increment size based on the number of Newton Raphson iterations in the previous

increment [103, 119] or reducing the time increment size if the change of the phase field in an integration point is above a given threshold [75]. The step size controller used in this work is a so-called elementary controller [128]. Its purpose is to reduce increments only as much as necessary to meet an error criterion and thus maintaining larger time increments. For each increment $k + 1$, for which no valid solution was obtained, the newly adapted time increment Δt_{k+1} is defined by

$$\Delta t_{k+1} = \sqrt{\frac{\epsilon}{\hat{r}}} \Delta t_k, \tag{4.15}$$

where $\hat{r}$ is the maximum error from Equation (4.14) and ϵ is the error tolerance. The resulting scaling factor is commonly limited by upper and lower bounds to prevent excessive changes in the increment size and, thus, reduce computational cost and circumvent divergence of the solution. Herein, the limits proposed by Gupta et al. [58] are inherited:

$$\rho = \sqrt{\frac{\epsilon}{\hat{r}}} \tag{4.16}$$

$$\hat{\rho} = \begin{cases} 1.0 & \text{if } \rho \geq 1.0 \\ 0.9 & \text{if } 1.0 \geq \rho \geq 0.9 \\ 0.5 & \text{if } 0.5 \geq \rho \\ \rho & \text{otherwise} \end{cases} \tag{4.17}$$

$$\Delta t_{k+1} = \hat{\rho} \Delta t_k, \tag{4.18}$$

4.3 Test setups, Results and Discussion

In the following sections, the phase field model will be validated using the results of tests for various different test setups, a SENB [29, 38], a DCB [33] and an ENB test [111]. The first two are standard tests for determining fracture properties in Mode-I. Both show stable crack propagation in a displacement controlled setting. In general, the DCB is simpler in regard to specimen preparation and deformation measurement, however, due to its dimensions, observations are limited to the TL and RL fracture planes [38, 127]. The ENB test is used for determining fracture properties in Mode-II and shows, in comparison to the other two types, a rather brittle response. For determination of fracture properties of wood it is of interest because of the strong influence of the materials weak fracture planes.

In the used phase field model, the linear elastic stiffness properties, the tensile strength, the fracture energy release rate and the influence of the microstructure in form of a scaling factor of the structural tensor can be altered. Except for the scaling of the structural tensor, initial values can be found in literature, however, they are subject to quite large scatter. Initially, for each test setup, the linear elastic stiffness is determined by using the data from the specific publication. If necessary, the *Young*'s moduli and the shear moduli are scaled to match the linear elastic load path observed in the experiments.

The quantity subject to the most uncertainty is the scaling factor used in the structural tensor, which accounts for the material's weak fracture planes. The crack orientation in the SENB and the DCB test is less influenced by those planes, however, as mentioned, the ENB test is. Therefore, after an initial mesh study on all models, a parameter sweep of the structural tensor's scaling factor is performed, searching for a value suited to recover the expected horizontal crack path (Figure 4.7). Subsequently, using the found value, the remaining quantities, namely the tensile strength and the fracture energy release rate, are determined for each test setup individually.

With more complex, three-dimensional simulations in mind for future application of this model, the validation is carried out using linear tetrahedral elements. For all simulations and all phase fields, the length scale factor to effective finite element size ratio of 5 is used, where the effective element size l_{eff} is computed by taking the average diameter of spheres fitted into the tetrahedral elements withing the h-refined region around the expected crack path. For the DCB and the ENB tests, the expected final crack covers a large part of the beam. Due to the required small mesh size, this would lead to a very large amount of DOFs. Therefore, only a part of the region where the crack is expected to initiate is h-refined. Additionally, as no crack path is prescribed, i.e., crack propagation and initiation is only influenced by the tensile strength, the fracture energy release rate, the structural tensor and the elastic stiffness properties, the h-refined region is expanded perpendicular to the expected crack path in order to cover a wider range of possible cracks. As the results in the following sections show, this is already sufficient for tuning the models. The artificial stiffness parameter in the degradation function is fixed to 10^{-7}.

The entire code is implemented in Julia [14]. For automatically deriving the element stiffness matrices and residual vectors from the energy formulation, the ForwardDiff-Package [115] is used. Pardiso 6.0 [30, 74, 135] is employed as the sparse linear solver.

4.3.1 Test setups and linear elastic stiffness properties

Single edge notched beam

The experimental data for the SENB tests was taken from Daudeville [29] and Dourado et al. [38]. Both contain data of load deflection graphs, measured at the loading point shown in Figure 4.5. The nominal beam dimensions from Daudeville [29] are $w_{pc} = 1\,\text{mm}$, $w_b = 45\,\text{mm}$, $h_b = 45\,\text{mm}$, $h_{pr} = 27\,\text{mm}$, $l_{b,1} = 112.5\,\text{mm}$ and $l_{b,2} = 45\,\text{mm}$, with the middle block once being oriented such that the radial direction and once such that the tangential direction matches the global x-direction. The linear elastic stiffness properties for the spruce specimen were taken from the original publication where values from EN338 [42] were scaled to match the experimental results, leading to: $C_{1111} = 8999.13$, $C_{1122} = 268.29$, $C_{1133} = 174.23$, $C_{2222} = 479.03$, $C_{2233} = 117.18$, $C_{3333} = 267.00$, $C_{1212} = 552.00$, $C_{1313} = 552.00$ and $C_{2323} = 32.00$, where all values are given in MPa. For the beam from Dourado et al. [38], the nominal beam dimensions are: $w_{pc} = 1\,\text{mm}$, $w_b = 40\,\text{mm}$, $h_b = 70\,\text{mm}$, $h_{pr} = 35\,\text{mm}$, $l_{b,1} = 210\,\text{mm}$ and $l_{b,2} = 70\,\text{mm}$, where the middle block is oriented, such that the tangential direction matches the global x-direction. The linear elastic stiffness properties for the Norway spruce specimen were taken from the original publication which uses values from Guitard [56]. The values were scaled to match the experimental results, leading to: $C_{1111} = 7704.43$, $C_{1122} = 386.54$, $C_{1133} = 256.96$, $C_{2222} = 676.433$, $C_{2233} = 213.95$, $C_{3333} = 377.59$, $C_{1212} = 375.00$, $C_{1313} = 475.00$ and $C_{2323} = 16.50$, where all values are given in MPa.
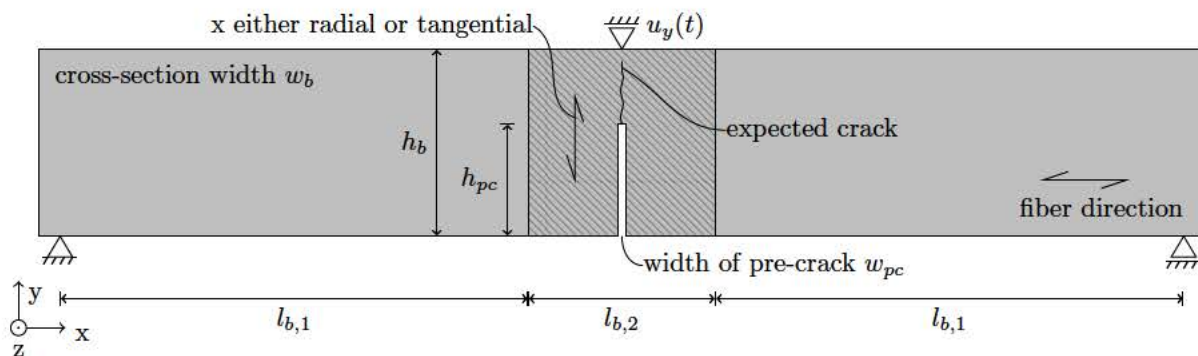

Fig. 4.5: Geometry and dimensions of the examined SENB tests.

Double cantilever beam

The experimental data for the DCB test was taken from de Moura et al. [33], which contains data for multiple different beams, with the same dimensions. Figure 4.6 shows the examined specimen, where $w_{pc} = 1\,\text{mm}$, $w_b = 20\,\text{mm}$, $h_b = 20\,\text{mm}$, $l_{pr} = 100\,\text{mm}$ and $l_b = 280\,\text{mm}$. The load is measured at the upper loading point and the deformation is measured as the change in distance between the two loading points. The elastic stiffness properties for Pinus pinaster where taken from the original publication which uses properties found in Pereira [107] for elastic moduli and *Poisson*'s ratios and shear moduli from WHB [137]: $C_{1111} = 16430.17$, $C_{1122} = 1602.22$, $C_{1133} = 1053.28$, $C_{2222} = 2490.16$, $C_{2233} = 823.95$, $C_{3333} = 1300.40$, $C_{1212} = 1115.00$, $C_{1313} = 1042.00$ and $C_{2323} = 170.50$, where all values are given in MPa. In order to capture the broad range of the experimental results, the simulations where carried out for multiple, differently scaled elastic stiffness properties.
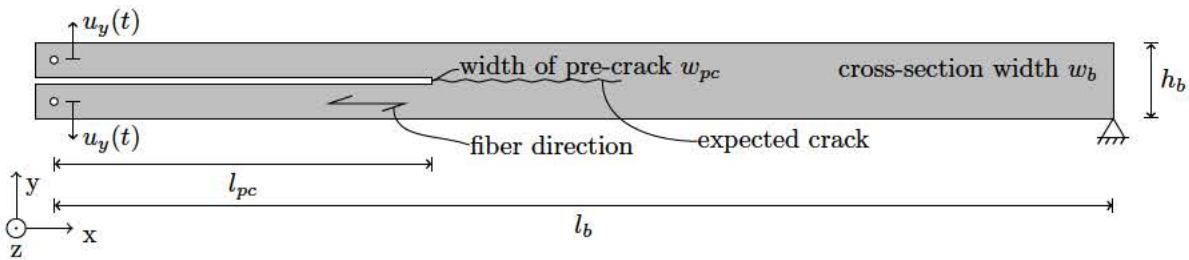

Fig. 4.6: Geometry and dimensions of the examined DCB test.

End notched beam

The experimental data for the ENB test was taken from Rautenstrauch et al. [111], which contains data for multiple different beam, with equal dimensions. Figure 4.7 shows the examined specimen, where $w_b = 80\,\text{mm}$, $h_b = 200\,\text{mm}$ and $l_b = 1600\,\text{mm}$. For the beams of length $l_b = 1600\,\text{mm}$, glued laminated timber with 5 lamellas was used. The load is measured at the left support and the deformation at the center loading point. As described by Rautenstrauch et al. [111], the crack propagated along the weak interface at the growth surface, along the fiber direction. Therefore, as the notch is within the middle board for this test setup, the influence of the lamination is neglectable. Hence, elastic stiffness properties for spruce where taken from [137] and slightly scaled to match the range of the experimental results, leading to: $C_{1111} = 11564.35$, $C_{1122} = 487.41$, $C_{1133} = 349.11$, $C_{2222} = 997.63$, $C_{2233} = 249.03$, $C_{3333} = 549.19$, $C_{1212} = 718.08$, $C_{1313} = 684.42$ and $C_{2323} = 33.66$, where all values are given in MPa.
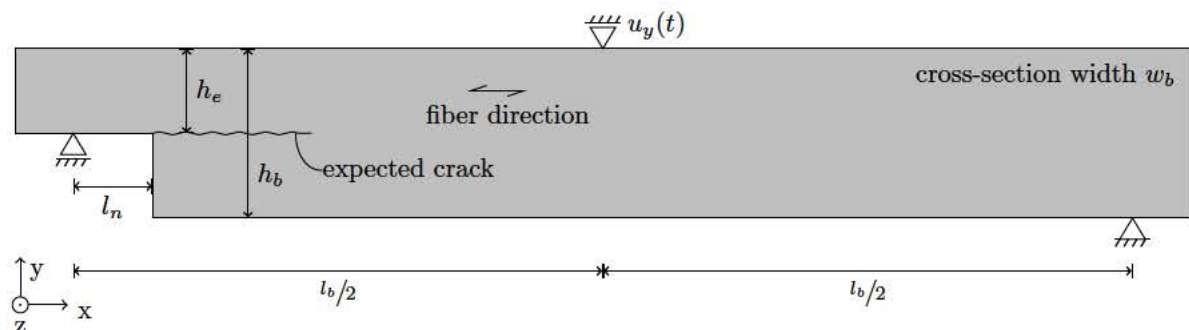

Fig. 4.7: Geometry and dimensions of the examined ENB test.

4.3.2 Mesh study

In order to assure spatial convergence, an initial mesh study was conducted. Due to lack of knowledge of the ultimate load from a close form solution, the finest mesh was used as a reference. For all mesh studies, the graph on the left in Figure 4.8 shows the error of the ultimate load relative to the reference solution. The graph on the right shows the same quantities in a double-log manner (excluding the reference solution, as the relative error is zero), thus allowing assessment of the convergence rate and order. A sufficiently accurate mesh for the given setting is selected based on a relative error smaller than 0.1, if the convergence order is, at least, above linear. Therefore, the meshes circled in red are used in all further computations. For the assumed spatially converged meshes, the simulation times ranged from two to six days using 12 *AMD EPYC 7402* processors.
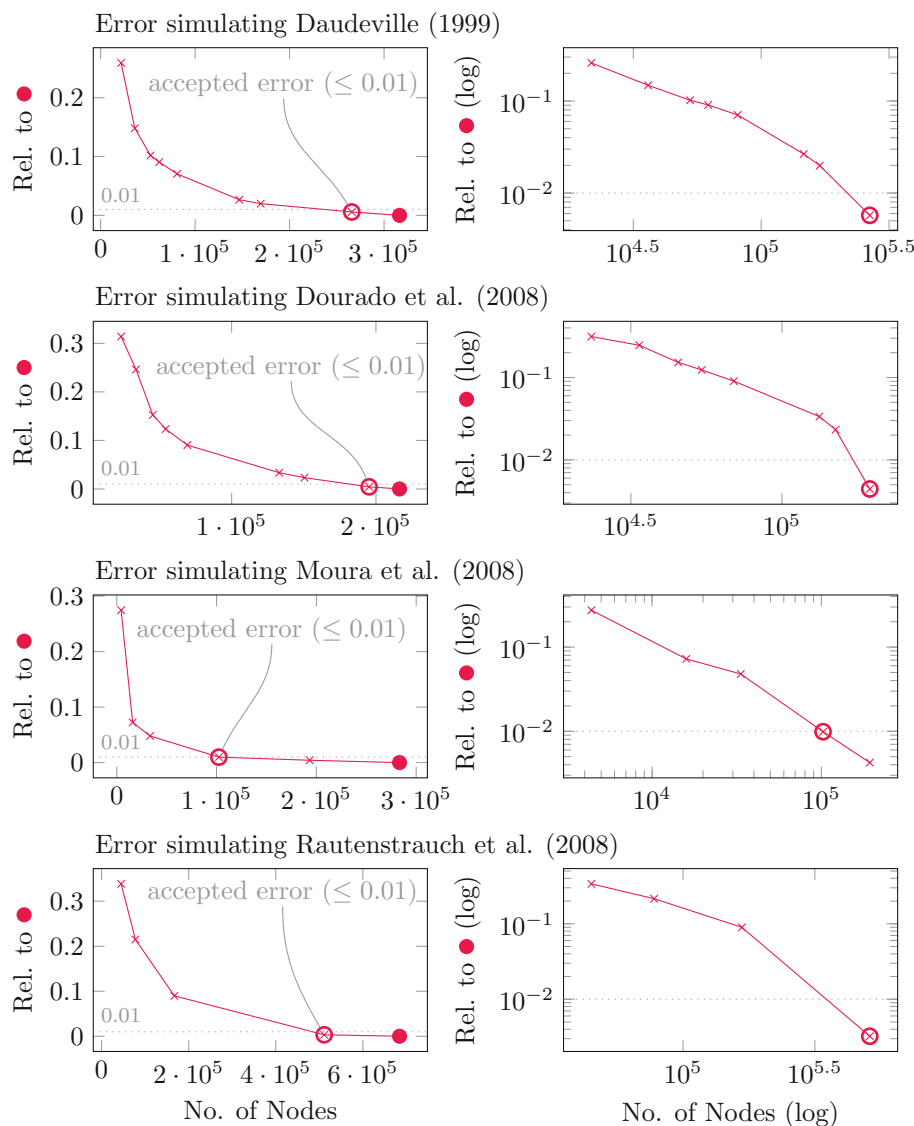

Fig. 4.8: Mesh study of the examined specimens. The graphs show the relative error of the ultimate load for each mesh in relation to the finest simulated mesh (●). The converged mesh (○) has an error below the selected threshold, and all double log graphs show at least a convergence of linear order.

4.3.3 Structural tensor scale

The ENB test from Rautenstrauch et al. [111] is the test most influenced by the micro- and macrostructure of wood. Therefore, it is used for estimating the required size of the structural tensor's scale factor. A parameter sweep of the scale factor is performed from 0 to 90 in increments of 10. Figure 4.9 shows the resulting crack phase fields on the left and the ultimate loads with the crack angles on the right. Increasing ultimate loads for larger scale factors, also reported by Teichtmeister et al. [132], are visible. Interestingly, also for similar crack orientations, the ultimate load increases. For reproducing the experimentally observed crack path, a value of $\beta_2 = \beta_3 = 70$ is sufficient. Higher values only marginally reduce the incline of the phase field crack. Therefore, all further simulations use this value.
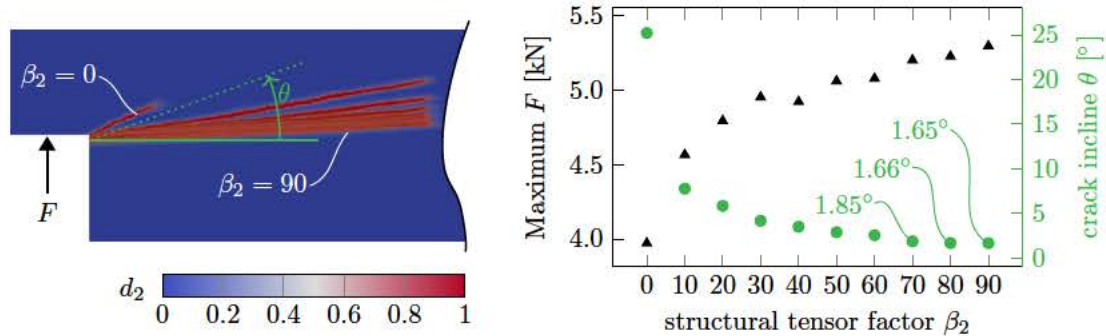

Fig. 4.9: Comparison of different structural tensor scale factors for the ENB test. From $\beta_2 = 70$ onwards, the change in θ is marginal, whereas F is increasing more pronounced.

4.3.4 Simulation results

Single edge notched beam

The SENB tests by Daudeville [29] were carried out for two different orientations of the middle block, once R in the x-direction and once T in the x-direction. This approach allows the assessment of fracture behavior in both the RL- and TL-plane. Figure 4.10 shows the fully evolved crack phase field for the test in the RL-plane. Figure 4.11 shows that the elastic load path for both orientations and the respective experimental data. The parameters defining the phase field evolution, the tensile strength, and the fracture energy release rate were separately obtained for R and T. As a crack perpendicular to L is not expected in this kind of simulation, only phase fields d_2 (for R) and d_3 (for T), from Section 4.2.3 are considered. With this two-phase field model, using $f_{t,2} = 3.83\,\mathrm{MPa}$ and $G_{c,2} = 0.089\,\mathrm{N/mm}$, and $f_{t,3} = 2.03\,\mathrm{MPa}$ and $G_{c,3} = 0.053\,\mathrm{N/mm}$, in Equations (4.1) and (4.7), results in an excellent fit of the experimental data.

In Daudeville [29] both the fracture energy and the fracture energy release rate were computed, though only the latter is of interest for comparison with the quantities found in this work. The fracture energy release rate was obtained using linear elastic fracture mechanics by application of the crack closure technique [117]. For a fixed tensile strength of $f_t = 4.5\,\mathrm{MPa}$ for both R and T, values of $G_{c,2} = 0.144\,\mathrm{N/mm}$ and $G_{c,3} = 0.077\,\mathrm{N/mm}$ are reported. All values are higher than the ones from the phase field model. Given the usage of the structural tensor for considering the material's principal direction, this is reasonable (see Section 4.3.3). In addition, the phase field model also considers toughening effects, and the assumption of equal tensile strengths for R and T is questionable. Research in Lukacevic et al. [85] showed that the tensile strength for spruce under Mode-I loading in T direction is about $2.00\,\mathrm{MPa}$ and about $4.50\,\mathrm{MPa}$ for R. The applied phase field model captures those differences very well.
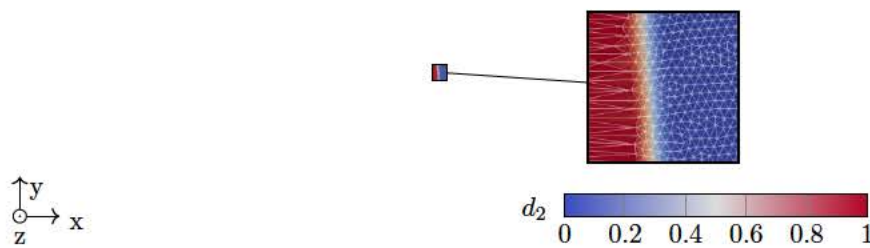
Fig. 4.10: Final phase field d_2 and mesh for the SENB test from Daudeville [29] for the RL-pane.
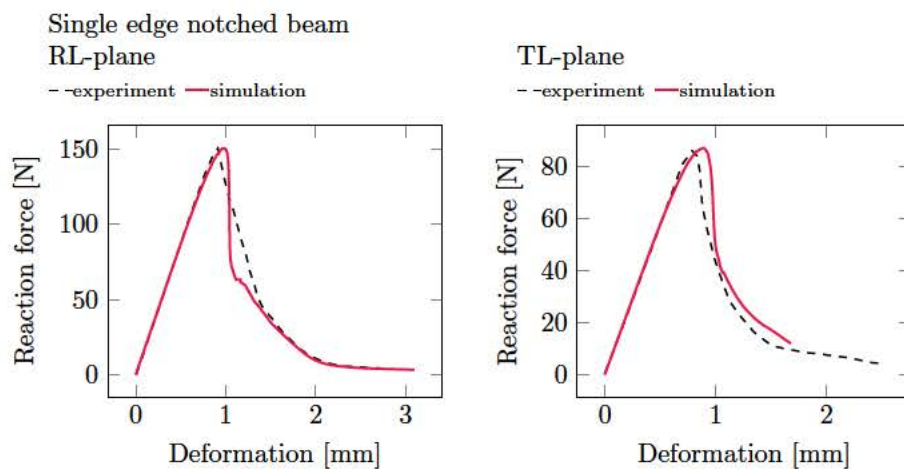

Fig. 4.11: Load deformation graph for the SENB test from Daudeville [29].

In addition to these SENB tests, the configuration from Dourado et al. [38] with different nominal dimensions was examined. The load deflection path for the simulation and the experimental data is shown in Figure 4.12, where $f_{t,3} = 1.36\,\text{MPa}$ and $G_{c,3} = 0.07\,\text{N/mm}$ are used. The simulation agrees with experimental data very well. Furthermore, the low tensile strength of the tangential direction matches the observations from the SENB test from Daudeville [29]. Comparison with the model in Dourado et al. [38] is of limited meaning due to different approaches taken. Failure processes are determined on different stages of specimen failure with stage-specific parameters: Crack initiation is only determined by the tensile strength. After a crack is formed, a bilinear softening law, and the fracture energy release rate define crack propagation. In the proposed phase field model, the tensile strength, the fracture energy release rate, and a linear softening law influence crack initiation and propagation. Nevertheless, the tensile strength of $f_t = 1.66\,\text{MPa}$ with a standard deviation of $0.13\,\text{MPa}$, obtain with the model in Dourado et al. [38], is close to the value found for the phase field model. However, the total fracture energy release rate (micro-cracking and fiber bridging) of $G_c = 0.144\,\text{N/mm}$ with a standard deviation of $0.018\,\text{N/mm}$, is very different, likely due to the different softening law. Figure 4.13 shows the resulting, fully evolved crack phase field.
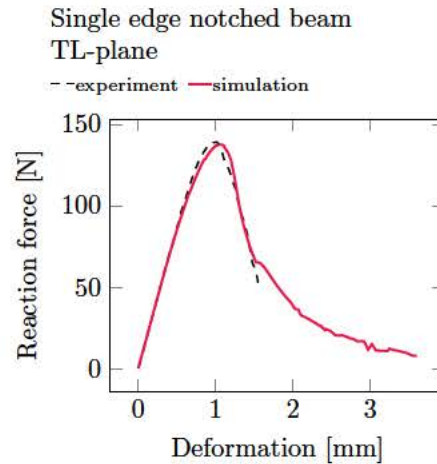
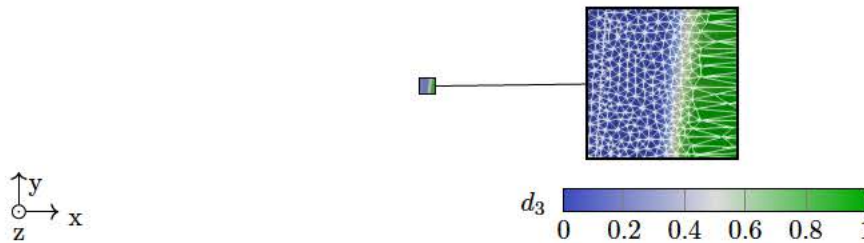**Fig. 4.12:** Load deformation graph for the SENB test from Dourado et al. [38].

Fig. 4.13: Final phase field d_3 and mesh for the SENB test from Dourado et al. [38].

Double cantilever beam

Considering the scatter in the experimental data for the DCB tests shown in Figure 4.14, the linear elastic stiffness values given in Section 4.3.1 are additionally scaled from 0.6 to 1.0 in steps of 0.1. Figure 4.14 shows that this way, keeping the tensile strength at $f_{t,2} = 3.34$ MPa and the fracture energy release rate at $G_{c,2} = 0.13$ N/mm, the entire range of the experimental data is recovered. In de Moura et al. [33] the same model used in Dourado et al. [38] was applied to obtain material parameters. Therefore, comparability with the phase field model is limited. They reported an average tensile strength of $f_t = 5.34$ MPa with a standard deviation of 1.00 MPa and a total fracture energy release rate (micro-cracking and fiber bridging) of $G_c = 0.261$ N/mm with a standard deviation of 0.063 N/mm. The found values overestimate the ones from the phase field model.

The finale crack phase field of the DCB test is depicted in Figure 4.15. Interestingly, the results show damaged zones ($0.3 \leq d_2 \leq 0.5$) above and below the main crack. The induced shear stresses are a known effect in the DCB test and may also account for the differences between the phase field model and the model proposed by de Moura et al. [33]. In de Moura et al. [33], the Mode-I crack path is predefined, so no shear cracks can form. Against the initial assumption that the crack path in the DCB test is not affected by the size of the structural tensor's scale factor, using the isotropic formulation (scale factor equal to zero) leads to a deviation from the expected crack path (Figure 4.16). Thus, again, highlighting the requirement for the structural tensor to properly model wood fracture and strengthening that the used scale factor of $\beta_2 = \beta_3 = 70$ is sufficient for reproducing the experimentally observed cracks.
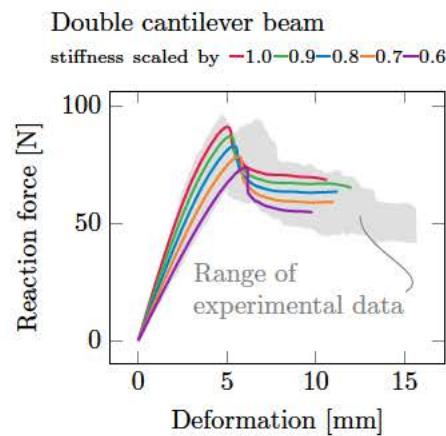
Fig. 4.14: Load deformation graph for the DCB test from de Moura et al. [33]. The simulation is performed for elastic stiffness values scaled from 0.6–1.0 and shows that all simulations are well within the range of the experimental results.
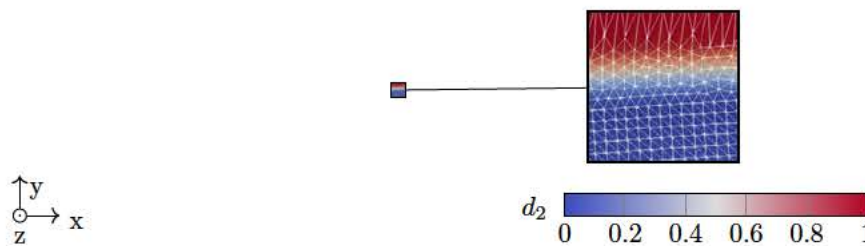

Fig. 4.15: Final phase field d_2 and mesh for the DCB test from de Moura et al. [33].
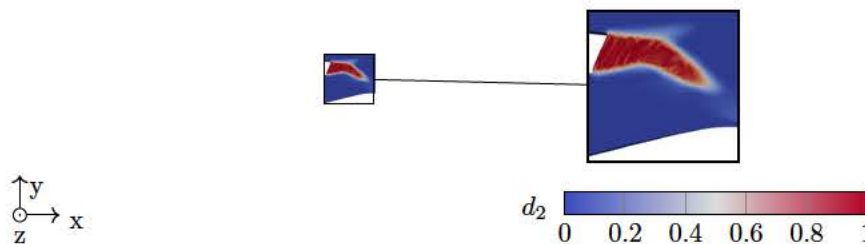

Fig. 4.16: Final phase field d_2 without the structural tensor for the DCB test from de Moura et al. [33].

End notched beam

Figure 4.17 shows the resulting load deflection path of the tests carried out by Rautenstrauch et al. [111]. For $f_{t,2} = 1.4\,\text{MPa}$ and $G_{c,2} = 0.09\,\text{N/mm}$, the response matches most of the experimental results well (red path in Figure 4.17). Figure 4.18 shows that the crack follows the expected, horizontal crack direction. In Rautenstrauch et al. [111], it was assumed that the critical fracture energy release rate equals the sum of the specific fracture energies in Mode-I and Mode-II. Therefore, a value of $G_c = 0.21\,\text{N/mm}$ with a shear strength of $f_\nu = 2.5\,\text{MPa}$ was used, which overestimates the results of the phase field model. The experiments are reproduced applying cohesive contact elements. Similar to the other discussed tests, due to substantial differences in the modeling, comparison of the obtained values is limited.

As the tensile strength and the fracture energy release rate resulting from the phase field model might be influenced by the specimens geometry and load, the found values from the SENB test from Daudeville [29] for spruce failure in the RL-plane are used for the ENB test as well. With $f_{t,2} = 3.83\,\text{MPa}$ and $G_{c,2} = 0.089\,\text{N/mm}$, the experimental range can still be covered (green path in Figure 4.17). Therefore, supporting that both parameters are material specific and thus represent physical quantities instead of being purely numerical values which need to be tuned for every test configuration.
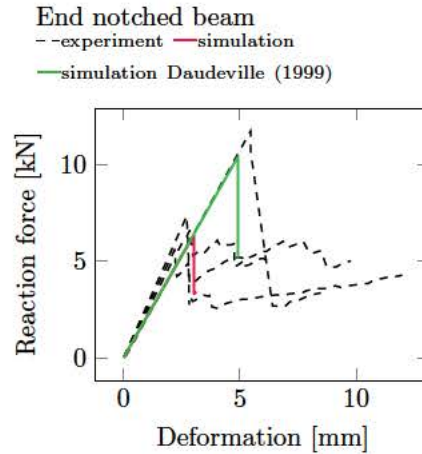

Fig. 4.17: Load deformation graph for the ENB test from Rautenstrauch et al. [111]. The simulation parameters are once tuned to match the experimental results at the lower reaction force regions and once using the simulation parameters the SENB test from Daudeville [29]. Both show good agreement with the reported range of the experimental data.
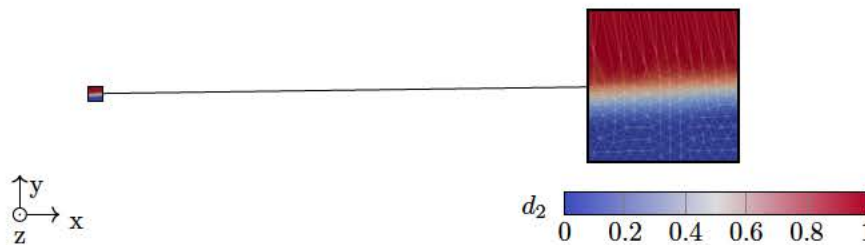

Fig. 4.18: Final phase field d_2 and mesh for the ENB test from Rautenstrauch et al. [111].

All simulations clearly show that the structural tensor is necessary for simulating wood fracture, where the material's structure strongly influences crack propagation. Especially in the ENB tests, it is of central importance to recover the expected horizontal crack path. The found lower bound value for the structural tensor's scale factor allows reproducing the crack paths of all considered experiments.

Compared to the models used in the cited experimental studies, a primary advantage of the phase field model is that crack paths are not predefined. Cracks form based on local crack driving energies and non-local effects due to the microstructure of wood. Therefore, the model is more versatile and applicable in complex situations where the crack path a priori unknown.

The phase field model excellently reproduces the experimental results, with tensile strengths and fracture energy release rates within the expected range for wood. Significantly, the differences in the radial and tangential direction are captured. Those findings strengthen the requirement for a multi-phase field model to distinguish different failure mechanisms.

To show that the input parameters are not specific to a single test setup, the tensile strength and the fracture energy release rate resulting from simulating the SENB test from Daudeville [29], were also used for simulating the ENB tests from Rautenstrauch et al. [111]. The results show that the response is also within the reported experimental range, thus confirming that the tensile strength, the fracture energy release rate, and the structural tensor are not model-specific parameters but material constants.

4.4 Conclusion and Outlook

The present work involves validating a phase field model for orthotropic non-brittle fracture of materials with favorable fracture planes and multiple, different failure mechanisms. Initially, the phase field model proposed in Pech et al. [105] is summarized, and an improvement of the solver is discussed, required for simulating the considered experimental studies. This addition to the solver focuses on maintaining large load increment steps in regions where no crack growth appears and reducing the load increment size prior to strong nonlinearities. The peak finder algorithm reduces the increment size close to the ultimate load in the response graph by evaluating a found set of state variables (deformation field and phase field). Looking ahead in time, it rejects a state in case of rapid changes in the stored energy. In addition, the step size controller takes care of changing the load increment size such that a reduction is just as slight as needed. Subsequently, the proposed model was used to simulate four different test setups. In conclusion:

- A generally applicable algorithm for efficiently solving the coupled phase field problem was found, which is very flexible as it requires no alterations of the energy terms like introducing a history or penalty function.

- Using a non-brittle multi-phase field model with a structural tensor allows reproducing experimental results of wood tests, where the tensile strength and the fracture energy release rate are in the expected range for wood.

- A minimum required value for the scale factor of the structural tensor was determined.

- The input parameters for the phase field model are not purely numerical values and can be transferred to other models and considered material constants.

The present work is the first contribution to modeling fracture mechanics of wood on a macroscopic scale using the phase field method for fracture. It opens the field for future research. Of particular interest is the further assessment of the herein found structural tensor's scale factor on tests with similar properties as the shown ENB test to narrow the quantities range.

Wood testing is generally subject to a large scatter of material parameters, even in the linear elastic stiffness. Therefore, detailed models are required incorporating more information about the used material, like the exact fiber courses, for adequately reproducing experiments. This is where the phase field model can outperform other modeling approaches like XFEM. The proposed approach can already model cracks of arbitrary complexity, allowing fracture mechanic simulations of wooden boards with multiple knots and complex fiber courses. Such simulations are the basis for a subsequent homogenization step similar to the one outlined in Lukacevic et al. [84], where after the reconstruction of the knot geometry [69], bending stiffness profiles are computed. The reduction of model parameters enables the application to larger-scale structures for optimization [104] or prediction of failure mechanisms and bending strength of glued laminated timber beams [136]. Such tensile strength or fracture energy release rate profiles allow proper consideration of fracture processes of wood in larger-scale structures where a detailed simulation is not possible.

Acknowledgement

Conclusion and Perspectives

In the following the main findings of Publications 1 to 4 are summarized, and future research is discussed.

Main Findings

Publication 1 deals with the optimization of the load-bearing behavior of GLT beams. The problem is stated as follows: "Given a set of wooden boards, find an arrangement in a group of beams such that the maximum deflection of each beam is as small as possible". A single wooden board or lamella in a GLT beam is characterized by a stiffness profile that accounts for fiber deviations and knots in the material. The task is solving a combinatorial optimization problem, where the objective function depends on computationally expensive finite element calculations. In the work, we show that even simplifying the problem by considering a constant stiffness for each lamella does not allow for a straightforward solution scheme. Therefore, three metaheuristic methods, a genetic algorithm, an iterated local search and a local search, are used to find a near-optimal solution. Though these approaches reduce the computational effort, evaluating the finite element model is still too costly to solve the problem in a reasonable time. Therefore, a metamodel is used to estimate the maximum deflection of a beam, given a specific arrangement of lamellas. The derived metamodel is capable of predicting the finite element simulations very well. The two components together allow solving the posed problem. The iterated local search algorithm can find solutions very quickly. However, it is less robust than the genetic algorithm, which found some of the best solutions independent of the initial guess. Local search was clearly outperformed. A common practice for optimizing GLT beams is combining different wood grading classes and placing higher graded boards in the outer layers of the beam. Using this set of boards of mixed grading classes, the optimization algorithm is capable of improving conventional assembly by 15 % to 20 %. Furthermore, the stronger the variability in the stiffness of the boards i.e., the more knots and defects a board has, the more the optimization algorithm can improve the assembly.

Publication 2 addresses the implementation of an improved general multi-surface return-mapping algorithm for simulating plasticity in orthotropic materials. The algorithm is implemented as a user subroutine in the commercial finite element software Abaqus. To properly model wood failure in both plasticity and fracture, so-called failure surfaces are used. The surfaces are described in a Tsai-Wu failure criterion. Different failure mechanisms are linked to individual surfaces, which are then combined to form a multi-surface failure criterion, intersecting in a non-smooth manner. As an improvement, a three-stage procedure is proposed, which allows for overcoming convergence issues of the original algorithm. In the first stage, an optimized version of the return-mapping algorithm is used, where the constraint on the so-called consistency parameter is checked in each *Newton-Raphson* iteration. Surfaces violating this constraint are assumed to be inactive and are further excluded. This allows finding the ultimate set of active surfaces faster. However, as intermediate solutions are not converged, this can lead to premature exclusion. Therefore, if no solution was found in the first stage, in the second stage, an exact version of the algorithm is used, where constraints are assessed after the *Newton-Raphson* procedure converged. If no solution was found in the second stage, the algorithm is restarted, checking every possible combination of surfaces. This improved scheme was tested on multiple real-life examples and was found to be very

robust. The additional computation overhead of the multi-stage approach is minimal compared to the computational effort of solving non-linear finite element problems. Furthermore, it allows for larger load increments as stages two and three can also find solutions to strain states for which the original algorithm did not converge. This is illustrated using three specific initial configurations, which require stages two or three to obtain solutions.

Publication 3 deals with wood fracture mechanics and presents a phase field formulation for orthotropic non-brittle materials with significantly different failure mechanisms and favorable fracture planes. Cohesive behavior is modeled employing the unified phase field theory with a linear softening law. We introduce a stress-based split for orthotropic materials, which accounts for crack driving stresses in the classical fracture mechanics failure modes I, II and III on a fictitious crack surface. Crack surfaces are considered following observations of fracture processes in wood. In a multi-phase field model, a crack orientation for cracks perpendicular to the longitudinal, the radial and the tangential direction is applied. This allows consideration of the very different failure mechanisms occurring in wood. Additionally, a second-order structural tensor is used to scale the gradient of the phase field, accounting for preferable crack propagation directions, which for wood, are mainly along the wood fiber. The crack driving part of the phase field is coupled with the degradation part following a hybrid approach. Herein, a novel method is proposed where degradation is performed based on a smooth traction-free crack boundary condition, including a contact constraint. The model is validated regarding its capability to model common crack patterns found in wood. Initially, a single edge notched specimen with different fiber orientations is examined. By changing the fiber angle, the crack pattern changes as well. Cracks follow the fiber direction until they reach a certain extent at which the failure mode changes to a crack normal to the fiber. This leads to the commonly observed zig-zag pattern found in wood. The simulations clearly show that the applied hybrid approach is required for reproducing this pattern. In a more complex simulation of a wooden board with a single knot and spatially varying fiber orientations, we show that the model can reproduce expected crack patterns and account for cohesive behavior.

Publication 4 contains the validation of the model proposed in Publication 3 regarding the reproduction of wood tests from literature. Additionally, improvements to the solver are proposed to allow the simulation of larger models. This is achieved by enhancing the adaptive load increment algorithm. A peak-finder algorithm is applied, which evaluates converged solutions found for the coupled phase field-displacement problem. By performing an additional small step, the algorithm looks ahead in time and rejects solutions close to rapid changes in the stored energy. This allows refining load steps in regions close to peaks in the response graph and enables precise determination of the ultimate load of a structure. Furthermore, load increments are reduced by a step size controller, which ensures that increments are only reduced as much as necessary. In combination with the active set reduced space method taking care of the irreversibility constraint on a global level of the phase field model – instead of enforcing it by altering the energy term –, this solver is very flexible and robust. The model is validated against two different single edge notched beam tests for Mode-I failure in the radial and the tangential plane, a double cantilever beam for Mode-I failure in the radial plane and an end-notched beam test for Mode-II failure in the radial plane. The crack paths from the experiment were reproduced very well, despite no initial prescription of a crack path being given, and the simulated load-deflection paths were well within the experimental range. The found tensile strengths and energy release rates are in a reasonable range for wood, and especially the differences in the radial and tangential directions were captured. Additionally, a lower bound for the scale factor of the structural tensor was found, which was previously never determined for wood. The publication shows that the phase field method can simulate the complex fracture phenomena occurring in wood.

Perspectives and Future Research

The development of the phase field model for wood fracture in Publications 3 and 4 is the foundation for future simulations of more complex wood tests. In particular, the simulation of knot groups where complex crack patterns occur and cracks branch and merge. Being able to predict the failure of knot groups correctly allows finding strength and fracture energy profiles – similar to the stiffness profiles used in Publication 1 – and thus allows optimization of larger-scale models like an entire GLT beam. Steps involved in obtaining such profiles, given that enough experimental data of knot groups is available, could be:

1. Determine the fracture energy release rate and ultimate strength of board sections (including knot groups) using a subset of test specimen, by means of the phase field model from Publications 3 and 4.

2. Validate the obtained simulation results using the remaining subset of test specimen.

3. Generate arbitrary virtual knot group configurations which cover most of the cases found in wooden boards.

4. Simulate the generated knot groups using the phase field model.

5. Based on the results, derive a metamodel that correlates knot group parameters with simulation results, like the ultimate load or the effective fracture energy.

6. Validate the accuracy of the metamodel against the experimental data.

7. For a given actual board, reconstruct the fiber courses and knot geometry and use the metamodel to compute strength or effective fracture energy profiles.

For most parts of the steps mentioned above, solutions already exist. The algorithms for knot reconstruction [69] and computation of fiber courses [84] can be applied in Steps 3 and 7 for obtaining spatial fiber courses for random knot configurations and for reconstructing wooden boards. For Step 5, the metamodel can be found similar to the approach proposed in Publication 1, or by relying on more advanced approaches like artificial neural networks. However, it should be pointed out that the main limiting factor in the above list is the huge computational effort involved in the phase field simulations. This can limit the number of knot group configurations in Step 3, which influences the quality of the metamodel.

The models in Publications 2 to 4 discuss plasticity and fracture mechanics separately. Combining those models to support both failure mechanisms is not far-fetched. There are numerous recent publications on phase field models for elasto-plastic solids. Particularly, the coupling of fracture and plasticity poses a challenge. Most proposed models are based on decomposing the stored energy into an elastic and a plastic part. One of the first contributions in this field was made by [40]. The phase field formulation is not altered there, and plastic damage is accounted for in a function of the accumulated plastic strain. [6] proposed a variational model for plasticity where the plastic strain is considered in the phase field's degradation function. This allows phase field evolution with the plastic strain. Further models are proposed by [18, 44], who incorporate return-mapping procedures. The latter work also covers multi-surface plasticity. This allows application of the failure criterion used in Publication 2.

Bibliography

[1] EN-14080. *Timber Structures – Glued Laminated Timber and Glued Solid Timber – Requirements.* Aug. 1, 2013. URL: https://lesesaal.austrian-standards.at/effect/OnStandardsReader.action?show=&searchTerm=%2B%22En+14080%22&docLang=de&doc=481038.

[2] EN-1912. *Structural Timber – Strength Classes – Assignment of Visual Grades and Species.* Oct. 15, 2013. URL: https://lesesaal.austrian-standards.at/effect/OnStandardsReader.action?show=&searchTerm=%2B%22EN+1912%22&docLang=de&doc=506844.

[3] A. Abbo and S. Sloan. "A Smooth Hyperbolic Approximation to the Mohr-Coulomb Yield Criterion". In: *Computers & structures* 54.3 (1995), pp. 427–441.

[4] D. P. Adhikary, C. T. Jayasundara, R. K. Podgorney, and A. H. Wilkins. "A Robust Return-Map Algorithm for General Multisurface Plasticity: A Robust Return-Map Algorithm for General Multisurface Plasticity". In: *Int. J. Numer. Meth. Engng* 109.2 (Jan. 13, 2017), pp. 218–234. ISSN: 00295981. DOI: 10.1002/nme.5284. URL: http://doi.wiley.com/10.1002/nme.5284 (visited on 05/29/2020).

[5] H. K. Akpama, M. B. Bettaieb, and F. Abed-Meraim. "Numerical Integration of Rate-Independent BCC Single Crystal Plasticity Models: Comparative Study of Two Classes of Numerical Algorithms". In: *International Journal for Numerical Methods in Engineering* 108.5 (2016), pp. 363–422. ISSN: 1097-0207. DOI: 10.1002/nme.5215. URL: https://onlinelibrary.wiley.com/doi/abs/10.1002/nme.5215 (visited on 09/23/2020).

[6] M. Ambati, T. Gerasimov, and L. D. Lorenzis. "Phase-Field Modeling of Ductile Fracture". In: *Computational Mechanics* 55.5 (Apr. 2015), pp. 1017–1040. DOI: 10.1007/s00466-015-1151-4.

[7] M. Ambati, T. Gerasimov, and L. D. Lorenzis. "A Review on Phase-Field Models of Brittle Fracture and a New Fast Hybrid Formulation". In: *Comput. Mech.* 55.2 (Dec. 2014), pp. 383–405. DOI: 10.1007/s00466-014-1109-y.

[8] L. Ambrosio and V. M. Tortorelli. "Approximation of Functional Depending on Jumps by Elliptic Functional via T-Convergence". In: *Communications on Pure and Applied Mathematics* 43.8 (1990), pp. 999–1036. ISSN: 1097-0312. DOI: 10.1002/cpa.3160430805. URL: https://onlinelibrary.wiley.com/doi/abs/10.1002/cpa.3160430805 (visited on 09/03/2020).

[9] H. Amor, J.-J. Marigo, and C. Maurini. "Regularized Formulation of the Variational Brittle Fracture with Unilateral Contact: Numerical Experiments". In: *Journal of the Mechanics and Physics of Solids* 57.8 (Aug. 2009), pp. 1209–1229. DOI: 10.1016/j.jmps.2009.04.011.

[10] J. E. Baker. "Reducing Bias and Inefficiency in the Selection Algorithm". In: *Proceedings of the Second International Conference on Genetic Algorithms.* 1987, pp. 14–21.

[11] G. Barenblatt. "The Mathematical Theory of Equilibrium Cracks in Brittle Fracture". In: *Advances in Applied Mechanics.* Elsevier, 1962, pp. 55–129. DOI: 10.1016/s0065-2156(08)70121-2.

[12]   R. S. Barsoum. "Triangular Quarter-Point Elements as Elastic and Perfectly-Plastic Crack Tip Elements". In: *International Journal for Numerical Methods in Engineering* 11.1 (1977), pp. 85–98. ISSN: 1097-0207. DOI: 10.1002/nme.1620110109. URL: https://onlinelibrary.wiley.com/doi/abs/10.1002/nme.1620110109 (visited on 07/28/2020).

[13]   Z. P. Bažant and L. Cedolin. *Stability of Structures: Elastic, Inelastic, Fracture and Damage Theories.* World Scientific ed. Hackensack, NJ ; London: World Scientific Pub, 2010. 1011 pp. ISBN: 978-981-4317-02-3 978-981-4317-03-0.

[14]   J. Bezanson, A. Edelman, S. Karpinski, and V. B. Shah. "Julia: A Fresh Approach to Numerical Computing". In: *SIAM Rev.* 59.1 (2017), pp. 65–98. DOI: 10.1137/141000671.

[15]   J. Bleyer and R. Alessi. "Phase-Field Modeling of Anisotropic Brittle Fracture Including Several Damage Mechanisms". In: *Comput. Methods Appl. Mech. Eng.* 336 (2018), pp. 213–236. ISSN: 0045-7825. DOI: 10.1016/j.cma.2018.03.012. URL: http://www.sciencedirect.com/science/article/pii/S0045782518301373.

[16]   T. Blickle and L. Thiele. "A Comparison of Selection Schemes Used in Evolutionary Algorithms". In: *Evolutionary Computation.* 1997.

[17]   C. Blum and A. Roli. "Metaheuristics in Combinatorial Optimization: Overview and Conceptual Comparison". In: *ACM Comput. Surv.* 35.3 (2003), pp. 268–308.

[18]   M. J. Borden, T. J. R. Hughes, C. M. Landis, A. Anvari, and I. J. Lee. "A Phase-Field Formulation for Fracture in Ductile Materials: Finite Deformation Balance Law Derivation, Plastic Degradation, and Stress Triaxiality Effects". In: *Computer Methods in Applied Mechanics and Engineering.* Phase Field Approaches to Fracture 312 (Dec. 1, 2016), pp. 130–166. ISSN: 0045-7825. DOI: 10.1016/j.cma.2016.09.005. URL: https://www.sciencedirect.com/science/article/pii/S0045782516311069 (visited on 05/09/2022).

[19]   L. Bottou. "Large-Scale Machine Learning with Stochastic Gradient Descent". In: *Proceedings of COMPSTAT 2010* (2010), pp. 177–186.

[20]   B. Bourdin, G. Francfort, and J.-J. Marigo. "Numerical Experiments in Revisited Brittle Fracture". In: *Journal of the Mechanics and Physics of Solids* 48.4 (Apr. 2000), pp. 797–826. DOI: 10.1016/s0022-5096(99)00028-9.

[21]   B. Bourdin, G. A. Francfort, and J.-J. Marigo. *The Variational Approach to Fracture.* Springer-Verlag GmbH, Apr. 19, 2008. URL: https://www.ebook.de/de/product/11433060/blaise_bourdin_gilles_a_francfort_jean_jacques_marigo_the_variational_approach_to_fracture.html.

[22]   T. Q. Bui and X. Hu. "A Review of Phase-Field Models, Fundamentals and Their Applications to Composite Laminates". In: *Engineering Fracture Mechanics* 248 (May 1, 2021), p. 107705. ISSN: 0013-7944. DOI: 10.1016/j.engfracmech.2021.107705. URL: https://www.sciencedirect.com/science/article/pii/S0013794421001582 (visited on 04/27/2022).

[23]   J. Carlsson and P. Isaksson. "Dynamic Crack Propagation in Wood Fibre Composites Analysed by High Speed Photography and a Dynamic Phase Field Model". In: *International Journal of Solids and Structures* (July 1, 2018), pp. 78–85. DOI: 10.1016/j.ijsolstr.2018.04.015.

[24]   J. Carlsson and P. Isaksson. "Simulating Fracture in a Wood Microstructure Using a High-Resolution Dynamic Phase Field Model". In: *Engineering Fracture Mechanics* 232 (June 1, 2020), p. 107030. DOI: 10.1016/j.engfracmech.2020.107030.

[25]   M. Cervera, G. B. Barbat, M. Chiumenti, and J.-Y. Wu. "A Comparative Review of XFEM, Mixed FEM and Phase-Field Models for Quasi-brittle Cracking". In: *Arch Computat Methods Eng* 29.2 (Mar. 2022), pp. 1009–1083. ISSN: 1134-3060, 1886-1784. DOI: 10.1007/s11831-021-09604-8. URL: https://link.springer.com/10.1007/s11831-021-09604-8 (visited on 04/27/2022).

[26]   J. Clausen, L. Damkilde, and L. Andersen. "Efficient Return Algorithms for Associated Plasticity with Multiple Yield Planes". In: *Int. J. Numer. Methods Eng.* 66.6 (2006), pp. 1036–1059.

[27]   J. D. Clayton and J. Knap. "A Geometrically Nonlinear Phase Field Theory of Brittle Fracture". In: *Int J Fract* 189.2 (Oct. 1, 2014), pp. 139–148. ISSN: 1573-2673. DOI: 10.1007/s10704-014-9965-1. URL: https://doi.org/10.1007/s10704-014-9965-1 (visited on 05/03/2022).

[28]   R. F. Coelho, M. Herrera, M. Xiao, and W. Zhang. "On-Line Metamodel-Assisted Optimization with Mixed Variables". In: *Evolutionary Algorithms and Metaheuristics in Civil Engineering and Construction Management*. Computational Methods in Applied Sciences. Springer, 2015, pp. 1–15. DOI: 10.1007/978-3-319-20406-2_1.

[29]   L. Daudeville. "Fracture in Spruce: Experiment and Numerical Analysis by Linear and Non Linear Fracture Mechanics". In: *Holz als Roh-und Werkstoff* 57.6 (1999), pp. 425–432. DOI: 10.1007/s001070050068.

[30]   A. De Coninck, B. De Baets, D. Kourounis, F. Verbosio, O. Schenk, S. Maenhout, and J. Fostier. "Needles: Toward Large-Scale Genomic Prediction with Marker-by-Environment Interaction". In: *Genetics* 203.1 (May 1, 2016), pp. 543–555. ISSN: 1943-2631. DOI: 10.1534/genetics.115.179887. URL: https://academic.oup.com/genetics/article/203/1/543/5930303 (visited on 08/13/2021).

[31]   K. De Jong. "Parameter Setting in EAs: A 30 Year Perspective". In: *Parameter Setting in Evolutionary Algorithms*. Springer, 2007, pp. 1–18.

[32]   L. De Lorenzis and T. Gerasimov. "Numerical Implementation of Phase-Field Models of Brittle Fracture". In: *Modeling in Engineering Using Innovative Numerical Methods for Solids and Fluids*. CISM International Centre for Mechanical Sciences. Springer International Publishing, 2020, pp. 75–101. DOI: 10.1007/978-3-030-37518-8_3.

[33]   M. de Moura, J. Morais, and N. Dourado. "A New Data Reduction Scheme for Mode I Wood Fracture Characterization Using the Double Cantilever Beam Test". In: *Engineering Fracture Mechanics* 75.13 (Sept. 2008), pp. 3852–3865. DOI: 10.1016/j.engfracmech.2008.02.006.

[34]   J. L. Devore. *Probability and Statistics for Engineering and the Sciences*. Cengage Learning, 2010.

[35]   B. Dhas, M. Masiur Rahaman, K. Akella, D. Roy, and J. N. Reddy. "A Phase-Field Damage Model for Orthotropic Materials and Delamination in Composites". In: *Journal of Applied Mechanics* 85.1 (Nov. 28, 2017). ISSN: 0021-8936. DOI: 10.1115/1.4038506. URL: https://doi.org/10.1115/1.4038506 (visited on 05/04/2022).

[36]   N. P. van Dijk, J. J. Espadas-Escalante, and P. Isaksson. "Strain Energy Density Decompositions in Phase-Field Fracture Theories for Orthotropy and Anisotropy". In: *Int J Solids Struct* 196–197 (July 1, 2020), pp. 140–153. ISSN: 0020-7683. DOI: 10.1016/j.ijsolstr.2020.04.022. URL: http://www.sciencedirect.com/science/article/pii/S0020768320301396 (visited on 06/04/2020).

[37]   DIN-4074-1. *ÖNORM DIN 4074-1: Strength Grading of Wood – Part 1: Coniferous Sawn Timber*. Sept. 1, 2012. URL: https://lesesaal.austrian-standards.at/effect/OnStandardsReader.action?show=&searchTerm=&docLang=de&doc=443673.

[38] N. Dourado, S. Morel, M. de Moura, G. Valentin, and J. Morais. "Comparison of Fracture Properties of Two Wood Species through Cohesive Crack Simulations". In: *Composites Part A: Applied Science and Manufacturing* 39.2 (Feb. 2008), pp. 415–427. DOI: 10.1016/j.compositesa.2007.08.025.

[39] M. L. du Bos, F. Balabdaoui, and J. N. Heidenreich. "Modeling Stress-Strain Curves with Neural Networks: A Scalable Alternative to the Return Mapping Algorithm". In: *Computational Materials Science* 178 (June 1, 2020), p. 109629. ISSN: 0927-0256. DOI: 10.1016/j.commatsci.2020.109629. URL: http://www.sciencedirect.com/science/article/pii/S0927025620301208 (visited on 06/22/2020).

[40] F. P. Duda, A. Ciarbonetti, P. J. Sánchez, and A. E. Huespe. "A Phase-Field/Gradient Damage Model for Brittle Fracture in Elastic–Plastic Solids". In: *International Journal of Plasticity* 65 (Feb. 1, 2015), pp. 269–296. ISSN: 0749-6419. DOI: 10.1016/j.ijplas.2014.09.005. URL: https://www.sciencedirect.com/science/article/pii/S0749641914001892 (visited on 05/09/2022).

[41] J. Ehlbeck and F. Colling. "Die Biegefestigkeit von Brettschichtholzträgern in Abhängigkeit von Den Eigenschaften Der Brettlamellen". In: *Bau. mit Holz* 89.10 (1987), pp. 646–655.

[42] EN338. *Structural Timber–Strength Classes*. EN338. Comité Européen de Normalisation CEN, 1995.

[43] J. J. Espadas-Escalante, N. P. van Dijk, and P. Isaksson. "A Phase-Field Model for Strength and Fracture Analyses of Fiber-Reinforced Composites". In: *Composites Science and Technology* 174 (Apr. 12, 2019), pp. 58–67. ISSN: 0266-3538. DOI: 10.1016/j.compscitech.2018.10.031. URL: https://www.sciencedirect.com/science/article/pii/S0266353818315082 (visited on 05/04/2022).

[44] J. Fang, C. Wu, J. Li, Q. Liu, C. Wu, G. Sun, and Q. Li. "Phase Field Fracture in Elasto-Plastic Solids: Variational Formulation for Multi-Surface Plasticity and Effects of Plastic Yield Surfaces and Hardening". In: *International Journal of Mechanical Sciences* 156 (June 1, 2019), pp. 382–396. ISSN: 0020-7403. DOI: 10.1016/j.ijmecsci.2019.03.012. URL: https://www.sciencedirect.com/science/article/pii/S0020740318335070 (visited on 05/09/2022).

[45] J. Fang, C. Wu, Q. Liu, G. Sun, and Q. Li. "Implicit Integration of the Unified Yield Criterion in the Principal Stress Space". In: *J. Eng. Mech.* 145.7 (July 2019), p. 04019041. ISSN: 0733-9399, 1943-7889. DOI: 10.1061/(ASCE)EM.1943-7889.0001613. URL: http://ascelibrary.org/doi/10.1061/%28ASCE%29EM.1943-7889.0001613 (visited on 09/23/2020).

[46] G. Fink, A. Frangi, and J. Kohler. "Bending Tests on GLT Beams Having Well-Known Local Material Properties". In: *Mater. Struct.* 48.11 (Oct. 2014), pp. 3571–3584.

[47] B. Fox and M. McMahon. "Genetic Operators for Sequencing Problems". In: *Found. of genetic algorithms* 1 (1990), pp. 284–300.

[48] G. Francfort and J.-J. Marigo. "Revisiting Brittle Fracture as an Energy Minimization Problem". In: *Journal of the Mechanics and Physics of Solids* 46.8 (Aug. 1998), pp. 1319–1342. DOI: 10.1016/s0022-5096(98)00034-9.

[49] J. Füssl, M. Li, M. Lukacevic, J. Eberhardsteiner, and C. Martin. "Comparison of Unit Cell-Based Computational Methods for Predicting the Strength of Wood". In: *Engineering Structures* 141 (June 2017), pp. 427–443. DOI: 10.1016/j.engstruct.2017.03.005.

[50] J. Füssl, M. Lukacevic, S. Pillwein, and H. Pottmann. "Computational Mechanical Modelling of Wood—From Microstructural Characteristics over Wood-Based Products to Advanced Timber Structures". In: *Lecture Notes in Civil Engineering*. Springer International Publishing, 2019, pp. 639–673. DOI: `10.1007/978-3-030-03676-8_25`.

[51] M. Gendreau, J.-Y. Potvin, et al. *Handbook of Metaheuristics*. 2nd ed. International Series in Operations Research & Management Science 146. Springer US, 2010. DOI: `10.1007/978-1-4419-1665-5`.

[52] M. Gendreau and J.-Y. Potvin. "Tabu Search". In: *Handbook of Metaheuristics*. Springer, 2010, pp. 41–59.

[53] D. E. Goldberg. *Genetic Algorithms in Search, Optimization & Machine Learning*. Addison-Wesley Publishing Company, Jan. 1989.

[54] A. A. Griffith and G. I. Taylor. "VI. The Phenomena of Rupture and Flow in Solids". In: *Philosophical Transactions of the Royal Society of London. Series A, Containing Papers of a Mathematical or Physical Character* 221.582-593 (1921), pp. 163–198. DOI: `10.1098/rsta.1921.0006`. eprint: `https://royalsocietypublishing.org/doi/pdf/10.1098/rsta.1921.0006`.

[55] P. Guindos and M. Guaita. "A Three-Dimensional Wood Material Model to Simulate the Behavior of Wood with Any Type of Knot at the Macro-Scale". In: *Wood Sci. Technol.* 47.3 (2013), pp. 585–599. DOI: `10.1007/s00226-012-0517-4`.

[56] D. Guitard. *Mécanique Du Matériau Bois et Composites*. Collection Nabla. Toulouse: Cepadues-Editions, 1987. 238 pp. ISBN: 978-2-85428-152-1.

[57] O. Gültekin, H. Dal, and G. A. Holzapfel. "Numerical Aspects of Anisotropic Failure in Soft Biological Tissues Favor Energy-Based Criteria: A Rate-Dependent Anisotropic Crack Phase-Field Model". In: *Comput. Methods Appl. Mech. Eng.* 331 (2018), pp. 23–52. ISSN: 0045-7825. DOI: `10.1016/j.cma.2017.11.008`. URL: `http://www.sciencedirect.com/science/article/pii/S0045782517307132`.

[58] A. Gupta, U. M. Krishnan, R. Chowdhury, and A. Chakrabarti. "An Auto-Adaptive Sub-Stepping Algorithm for Phase-Field Modeling of Brittle Fracture". In: *Theoretical and Applied Fracture Mechanics* 108 (Aug. 1, 2020), p. 102622. ISSN: 0167-8442. DOI: `10.1016/j.tafmec.2020.102622`. URL: `https://www.sciencedirect.com/science/article/pii/S0167844220301981` (visited on 09/29/2021).

[59] C. Hackspiel, K. de Borst, and M. Lukacevic. "A Numerical Simulation Tool for Wood Grading Model Development". In: *Wood Sci. Technol.* 48.3 (2014), pp. 633–649. DOI: `10.1007/s00226-014-0629-0`.

[60] V. Hakim and A. Karma. "Crack Path Prediction in Anisotropic Brittle Materials". In: *Phys. Rev. Lett.* 95.23 (Dec. 2, 2005), p. 235501. DOI: `10.1103/PhysRevLett.95.235501`. URL: `https://link.aps.org/doi/10.1103/PhysRevLett.95.235501` (visited on 04/29/2022).

[61] T. Heister, M. F. Wheeler, and T. Wick. "A Primal-Dual Active Set Method and Predictor-Corrector Mesh Adaptivity for Computing Fracture Propagation Using a Phase-Field Approach". In: *Computer Methods in Applied Mechanics and Engineering* 290 (June 2015), pp. 466–495. DOI: `10.1016/j.cma.2015.03.009`.

[62] K. Hofstetter, C. Hellmich, and J. Eberhardsteiner. "Development and Experimental Validation of a Continuum Micromechanics Model for the Elasticity of Wood". In: *European Journal of Mechanics - A/Solids* 24.6 (Nov. 2005), pp. 1030–1053. ISSN: 09977538. DOI: `10.1016/j.euromechsol.2005.05.006`. URL: `https://linkinghub.elsevier.com/retrieve/pii/S0997753805000963` (visited on 05/29/2020).

[63] K. Hofstetter, C. Hellmich, and J. Eberhardsteiner. "Micromechanical Modeling of Solid-Type and Plate-Type Deformation Patterns within Softwood Materials. A Review and an Improved Approach". In: 61.4 (June 1, 2007), pp. 343–351. ISSN: 1437-434X. DOI: `10.1515/HF.2007.058`. URL: `https://www.degruyter.com/document/doi/10.1515/HF.2007.058/html` (visited on 03/11/2022).

[64] J. H. Holland, C. Langton, and S. W. Wilson. *Adaption in Natural and Artificial Systems: An Introductory Analysis with Applications to Biology, Control and Artificial Intelligence.* MIT Press, 1992.

[65] M. Hu, A. Olsson, M. Johansson, and J. Oscarsson. "Modelling Local Bending Stiffness Based on Fibre Orientation in Sawn Timber". In: *Eur. J. Wood Prod.* 76.6 (Nov. 1, 2018), pp. 1605–1621. ISSN: 1436-736X. DOI: `10.1007/s00107-018-1348-2`. URL: `https://doi.org/10.1007/s00107-018-1348-2` (visited on 03/15/2022).

[66] T. Hu, J. Guilleminot, and J. E. Dolbow. "A Phase-Field Model of Fracture with Frictionless Contact and Random Fracture Properties: Application to Thin-Film Fracture and Soil Desiccation". In: *Computer Methods in Applied Mechanics and Engineering* 368 (Aug. 15, 2020), p. 113106. ISSN: 0045-7825. DOI: `10.1016/j.cma.2020.113106`. URL: `http://www.sciencedirect.com/science/article/pii/S0045782520302905` (visited on 01/15/2021).

[67] G. R. Irwin. "Fracture". In: *Elasticity and Plasticity / Elastizität Und Plastizität.* Springer Berlin Heidelberg, 1958, pp. 551–590. DOI: `10.1007/978-3-642-45887-3_5`.

[68] G. Kandler, J. Füssl, E. Serrano, and J. Eberhardsteiner. "Effective Stiffness Prediction of GLT Beams Based on Stiffness Distributions of Individual Lamellas". In: *Wood Sci. Technol.* 49.6 (July 2015), pp. 1101–1121.

[69] G. Kandler, M. Lukacevic, and J. Füssl. "An Algorithm for the Geometric Reconstruction of Knots within Timber Boards Based on Fibre Angle Measurements". In: *Constr. and Build. Mater.* 124 (2016), pp. 945–960.

[70] G. Kandler, M. Lukacevic, C. Zechmeister, S. Wolff, and J. Füssl. "Stochastic Engineering Framework for Timber Structural Elements and Its Application to Glued Laminated Timber Beams". In: *Construction and Building Materials* 190 (Nov. 2018), pp. 573–592. ISSN: 09500618. DOI: `10.1016/j.conbuildmat.2018.09.129`. URL: `https://linkinghub.elsevier.com/retrieve/pii/S0950061818323080` (visited on 05/29/2020).

[71] F. E. Karaoulanis. "Implicit Numerical Integration of Nonsmooth Multisurface Yield Criteria in the Principal Stress Space". In: *Archives of Computational Methods in Engineering* 20.3 (2013), pp. 263–308.

[72] D. E. Knuth. *The Art of Computer Programming Vol. 2.* Addison–Wesley, 1997.

[73] M. Kociecki and H. Adeli. "Shape Optimization of Free-Form Steel Space-Frame Roof Structures with Complex Geometries Using Evolutionary Computing". In: *Eng. Appl. of Artif. Intell.* 38 (2015), pp. 168–182.

[74]   D. Kourounis, A. Fuchs, and O. Schenk. "Toward the Next Generation of Multiperiod Optimal Power Flow Solvers". In: *IEEE Transactions on Power Systems* 33.4 (July 2018), pp. 4005–4014. ISSN: 1558-0679. DOI: 10.1109/TPWRS.2017.2789187.

[75]   P. K. Kristensen and E. Martínez-Pañeda. "Phase Field Fracture Modelling Using Quasi-Newton Methods and a New Adaptive Step Scheme". In: *Theoretical and Applied Fracture Mechanics* 107 (June 1, 2020), p. 102446. ISSN: 0167-8442. DOI: 10.1016/j.tafmec.2019.102446. URL: https://www.sciencedirect.com/science/article/pii/S0167844219305580 (visited on 09/29/2021).

[76]   C. Kuhn, A. Schlüter, and R. Müller. "On Degradation Functions in Phase Field Fracture Models". In: *Computational Materials Science* 108 (Oct. 2015), pp. 374–384. DOI: 10.1016/j.commatsci.2015.05.034.

[77]   P. Larranaga, C. M. Kuijpers, R. H. Murga, I. Inza, and S. Dizdarevic. "Genetic Algorithms for the Travelling Salesman Problem: A Review of Representations and Operators". In: *Artif. Intell. Rev.* 13.2 (1999), pp. 129–170.

[78]   M. Li, J. Füssl, M. Lukacevic, J. Eberhardsteiner, and C. Martin. "Strength Predictions of Clear Wood at Multiple Scales Using Numerical Limit Analysis Approaches". In: *Computers & Structures* 196 (2018), pp. 200–216.

[79]   M. López-Ibáñez, J. Dubois-Lacoste, L. P. Cáceres, M. Birattari, and T. Stützle. "The Irace Package: Iterated Racing for Automatic Algorithm Configuration". In: *Oper. Res. Perspect.* 3 (2016), pp. 43–58.

[80]   H. R. Lourenço, O. C. Martin, and T. Stützle. "Iterated Local Search: Framework and Applications". In: *Handbook of Metaheuristics.* Springer, 2010, pp. 363–397.

[81]   Y. Lu, T. Helfer, B. Bary, and O. Fandeur. "An Efficient and Robust Staggered Algorithm Applied to the Quasi-Static Description of Brittle Fracture by a Phase-Field Approach". In: *Computer Methods in Applied Mechanics and Engineering* 370 (Oct. 1, 2020), p. 113218. ISSN: 0045-7825. DOI: 10.1016/j.cma.2020.113218. URL: https://www.sciencedirect.com/science/article/pii/S0045782520304035 (visited on 04/27/2022).

[82]   M. Lukacevic and J. Füssl. "Numerical Simulation Tool for Wooden Boards with a Physically Based Approach to Identify Structural Failure". In: *Eur. J. Wood Prod.* 72.4 (July 2014), pp. 497–508. ISSN: 0018-3768, 1436-736X. DOI: 10.1007/s00107-014-0803-y. URL: http://link.springer.com/10.1007/s00107-014-0803-y (visited on 05/29/2020).

[83]   M. Lukacevic, J. Füssl, and R. Lampert. "Failure Mechanisms of Clear Wood Identified at Wood Cell Level by an Approach Based on the Extended Finite Element Method". In: *Eng. Fract. Mech.* 144 (2015), pp. 158–175.

[84]   M. Lukacevic, G. Kandler, M. Hu, A. Olsson, and J. Füssl. "A 3D Model for Knots and Related Fiber Deviations in Sawn Timber for Prediction of Mechanical Properties of Boards". In: *Materials & Design* 166 (Mar. 15, 2019), p. 107617. ISSN: 0264-1275. DOI: 10.1016/j.matdes.2019.107617. URL: https://www.sciencedirect.com/science/article/pii/S0264127519300541 (visited on 04/26/2021).

[85]   M. Lukacevic, W. Lederer, and J. Füssl. "A Microstructure-Based Multisurface Failure Criterion for the Description of Brittle and Ductile Failure Mechanisms of Clear-Wood". In: *Engineering Fracture Mechanics* 176 (2017), pp. 83–99.

[86]   O. Maron and A. W. Moore. "The Racing Algorithm: Model Selection for Lazy Learners". In: *Lazy Learning.* Springer, 1997, pp. 193–225. DOI: 10.1007/978-94-017-2053-3_8.

[87] C. Meng, Z. Tang, M. Chen, and Q. Peng. "Return Mapping Algorithm in Principal Space for General Isotropic Elastoplasticity Involving Multi-Surface Plasticity and Combined Isotropic-Kinematic Hardening within Finite Deformation Framework". In: *Finite Elements in Analysis and Design* 150 (Oct. 1, 2018), pp. 1–19. ISSN: 0168-874X. DOI: 10.1016/j.finel.2018.07.001. URL: http://www.sciencedirect.com/science/article/pii/S0168874X1730923X (visited on 09/23/2020).

[88] C. Miehe, F. Welschinger, and M. Hofacker. "Thermodynamically Consistent Phase-Field Models of Fracture: Variational Principles and Multi-Field FE Implementations". In: *Int. J. Numer. Methods Eng.* 83.10 (2010), pp. 1273–1311. DOI: 10.1002/nme.2861. eprint: https://onlinelibrary. wiley.com/doi/pdf/10.1002/nme.2861.

[89] C. Miehe, M. Hofacker, and F. Welschinger. "A Phase Field Model for Rate-Independent Crack Propagation: Robust Algorithmic Implementation Based on Operator Splits". In: *Comput. Methods Appl. Mech. Eng.* 199.45 (2010), pp. 2765–2778. ISSN: 0045-7825. DOI: 10.1016/j.cma.2010.04.011. URL: http://www.sciencedirect.com/science/article/pii/S0045782510001283.

[90] C. Miehe, L.-M. Schänzel, and H. Ulmer. "Phase Field Modeling of Fracture in Multi-Physics Problems. Part I. Balance of Crack Surface and Failure Criteria for Brittle Crack Propagation in Thermo-Elastic Solids". In: *Comput. Methods Appl. Mech. Eng.* 294 (2015), pp. 449–485. ISSN: 0045-7825. DOI: 10.1016/j.cma.2014.11.016. URL: http://www.sciencedirect.com/science/article/pii/S0045782514004423.

[91] R. Moazenzadeh, B. Mohammadi, S. Shamshirband, and K.-w. Chau. "Coupling a Firefly Algorithm with Support Vector Regression to Predict Evaporation in Northern Iran". In: *Eng. Appl. of Comput. Fluid Mech.* 12.1 (2018), pp. 584–597. DOI: 10.1080/19942060.2018.1482476.

[92] N. Moës and T. Belytschko. "Extended Finite Element Method for Cohesive Crack Growth". In: *Engineering Fracture Mechanics* 69.7 (May 2002), pp. 813–833. ISSN: 00137944. DOI: 10. 1016/S0013-7944(01)00128-X. URL: https://linkinghub.elsevier.com/retrieve/pii/ S001379440100128X (visited on 07/28/2020).

[93] P. Moscato and C. Cotta. "A Modern Introduction to Memetic Algorithms". In: *Handbook of Metaheuristics*. Springer, 2010, pp. 141–183.

[94] M. A. Msekh, N. H. Cuong, G. Zi, P. Areias, X. Zhuang, and T. Rabczuk. "Fracture Properties Prediction of Clay/Epoxy Nanocomposites with Interphase Zones Using a Phase Field Model". In: *Engineering Fracture Mechanics* 188 (Feb. 1, 2018), pp. 287–299. ISSN: 0013-7944. DOI: 10.1016/ j.engfracmech.2017.08.002. URL: https://www.sciencedirect.com/science/article/pii/ S0013794417308020 (visited on 05/04/2022).

[95] M. A. Msekh, M. Silani, M. Jamshidian, P. Areias, X. Zhuang, G. Zi, P. He, and T. Rabczuk. "Predictions of J Integral and Tensile Strength of Clay/Epoxy Nanocomposites Material Using Phase Field Model". In: *Composites Part B: Engineering* 93 (May 15, 2016), pp. 97–114. ISSN: 1359-8368. DOI: 10.1016/j.compositesb.2016.02.022. URL: https://www.sciencedirect. com/science/article/pii/S1359836816001293 (visited on 05/04/2022).

[96] T. T. Nguyen, J. Réthoré, and M.-C. Baietto. "Phase Field Modelling of Anisotropic Crack Propagation". In: *Eur. J. of Mech. - A/Solids* 65 (2017), pp. 279–288. ISSN: 0997-7538. DOI: 10.1016/j.euromechsol.2017.05.002. URL: http://www.sciencedirect.com/science/ article/pii/S0997753816303321.

[97] V. P. Nguyen and J.-Y. Wu. "Modeling Dynamic Fracture of Solids with a Phase-Field Regularized Cohesive Zone Model". In: *Computer Methods in Applied Mechanics and Engineering* 340 (Oct. 1, 2018), pp. 1000–1022. ISSN: 0045-7825. DOI: 10.1016/j.cma.2018.06.015. URL: https://www.sciencedirect.com/science/article/pii/S004578251830313X (visited on 04/27/2022).

[98] J. Nocedal and S. J. Wright. *Numerical Optimization*. New York: Springer, 2006. ISBN: 978-0-387-40065-5. URL: http://proxy2.hec.ca/login?url=http://dx.doi.org/10.1007/978-0-387-40065-5 (visited on 05/29/2020).

[99] J. Nyström. "Automatic Measurement of Fiber Orientation in Softwoods by Using the Tracheid Effect". In: *Comp. and Electron. in Agric.* 41.1 (2003), pp. 91–99. ISSN: 0168-1699. DOI: 10.1016/S0168-1699(03)00045-0. URL: http://www.sciencedirect.com/science/article/pii/S0168169903000450.

[100] A. Olsson and J. Oscarsson. "Three Dimensional Fibre Orientation Models for Wood Based on Laser Scanning Utilizing the Tracheid Effect". In: *WCTE 2014, World Conference on Timber Engineering, Quebec City, Canada, August 10-14, 2014*. 2014.

[101] A. Olsson, J. Oscarsson, E. Serrano, B. Källsner, M. Johansson, and B. Enquist. "Prediction of Timber Bending Strength and In-Member Cross-Sectional Stiffness Variation on the Basis of Local Wood Fibre Orientation". In: *Eur. J. Wood Prod.* 71.3 (May 2013), pp. 319–333. ISSN: 0018-3768, 1436-736X. DOI: 10.1007/s00107-013-0684-5. URL: http://link.springer.com/10.1007/s00107-013-0684-5 (visited on 05/29/2020).

[102] J. Oscarsson, E. Serrano, A. Olsson, and B. Enquist. "Identification of Weak Sections in Glulam Beams Using Calculated Stiffness Profiles Based on Lamination Surface Scanning". In: *WCTE 2014, World Conference on Timber Engineering, Quebec City, Canada, August 10-14, 2014*. Université Laval. 2014.

[103] K. Paul, C. Zimmermann, K. K. Mandadapu, T. J. R. Hughes, C. M. Landis, and R. A. Sauer. "An Adaptive Space-Time Phase Field Formulation for Dynamic Fracture of Brittle Shells Based on LR NURBS". In: *Comput Mech* 65.4 (Apr. 1, 2020), pp. 1039–1062. ISSN: 1432-0924. DOI: 10.1007/s00466-019-01807-y. URL: https://doi.org/10.1007/s00466-019-01807-y (visited on 09/29/2021).

[104] S. Pech, G. Kandler, M. Lukacevic, and J. Füssl. "Metamodel Assisted Optimization of Glued Laminated Timber Beams by Using Metaheuristic Algorithms". In: *Eng. Appl. Artif. Intell.* 79 (2019), pp. 129–141. ISSN: 0952-1976. DOI: 10.1016/j.engappai.2018.12.010. URL: http://www.sciencedirect.com/science/article/pii/S0952197618302690.

[105] S. Pech, M. Lukacevic, and J. Füssl. "A Hybrid Multi-Phase Field Model to Describe Cohesive Failure in Orthotropic Materials, Assessed by Modeling Failure Mechanisms in Wood". Version 1. In: (2022). DOI: 10.48550/ARXIV.2203.12291. URL: https://arxiv.org/abs/2203.12291 (visited on 03/24/2022).

[106] G. L. Peng and Y. H. Wang. "A Node Split Method for Crack Growth Problem". In: *AMM* 182–183 (June 2012), pp. 1524–1528. ISSN: 1662-7482. DOI: 10.4028/www.scientific.net/AMM.182-183.1524. URL: https://www.scientific.net/AMM.182-183.1524 (visited on 07/28/2020).

[107] J. L. Pereira. "Mechanical Behaviour of Wood Pinus Pinaster Ait. in Traction on the Material Directions". PhD thesis. MSc Thesis, University of Trás-os-Montes e Alto Douro, Vila Real, Portugal, 2004.

[108] H. Petersson. "Use of Optical and Laser Scanning Techniques as Tools for Obtaining Improved FE-input Data for Strength and Shape Stability Analysis of Wood and Timber". In: *IV European Conference on Computational Mechanics, Paris, France.* 2010.

[109] K. Pham, H. Amor, J.-J. Marigo, and C. Maurini. "Gradient Damage Models and Their Use to Approximate Brittle Fracture". In: *International Journal of Damage Mechanics* 20.4 (Nov. 2010), pp. 618–652. DOI: 10.1177/1056789510386852.

[110] S. A. Ponnusami, S. Turteltaub, and S. van der Zwaag. "Cohesive-Zone Modelling of Crack Nucleation and Propagation in Particulate Composites". In: *Engineering Fracture Mechanics* 149 (Nov. 2015), pp. 170–190. ISSN: 00137944. DOI: 10.1016/j.engfracmech.2015.09.050. URL: https://linkinghub.elsevier.com/retrieve/pii/S0013794415005780 (visited on 07/28/2020).

[111] K. Rautenstrauch, B. Franke, S. Franke, and K. Schober. "A New Design Approach for End-Notched Beams: View in Code". In: *Paper No. CIB-W18/41-6-2, Proc., Meeting.* Vol. 41. 2008.

[112] C. R. Reeves. "Genetic Algorithms". In: *Handbook of Metaheuristics.* Springer, 2010, pp. 109–139.

[113] C. R. Reeves. "Genetic Algorithms for the Operations Researcher". In: *INFORMS J. on Comp.* 9.3 (1997), pp. 231–250.

[114] C. R. Reeves. "Using Genetic Algorithms with Small Populations." In: *ICGA.* Vol. 590. 1993.

[115] J. Revels, M. Lubin, and T. Papamarkou. "Forward-Mode Automatic Differentiation in Julia". July 26, 2016. arXiv: 1607.07892 [cs]. URL: http://arxiv.org/abs/1607.07892 (visited on 08/13/2021).

[116] P. Roy, S. P. Deepu, A. Pathrikar, D. Roy, and J. N. Reddy. "Phase Field Based Peridynamics Damage Model for Delamination of Composite Structures". In: *Composite Structures* 180 (Nov. 15, 2017), pp. 972–993. ISSN: 0263-8223. DOI: 10.1016/j.compstruct.2017.08.071. URL: https://www.sciencedirect.com/science/article/pii/S026382231731601X (visited on 05/04/2022).

[117] E. F. Rybicki and M. F. Kanninen. "A Finite Element Calculation of Stress Intensity Factors by a Modified Crack Closure Integral". In: *Engineering Fracture Mechanics* 9.4 (Jan. 1, 1977), pp. 931–938. ISSN: 0013-7944. DOI: 10.1016/0013-7944(77)90013-3. URL: https://www.sciencedirect.com/science/article/pii/0013794477900133 (visited on 03/17/2022).

[118] W. M. Scherzinger. "A Return Mapping Algorithm for Isotropic and Anisotropic Plasticity Models Using a Line Search Method". In: *Computer Methods in Applied Mechanics and Engineering* 317 (2017), pp. 526–553.

[119] A. Schlüter, A. Willenbücher, C. Kuhn, and R. Müller. "Phase Field Approximation of Dynamic Brittle Fracture". In: *Comput. Mech.* 54.5 (Nov. 1, 2014), pp. 1141–1161. ISSN: 1432-0924. DOI: 10.1007/s00466-014-1045-x.

[120] J. Schmidt and M. Kaliske. "Zur dreidimensionalen Materialmodellierung von Fichtenholz mittels eines Mehrflächen-Plastizitätsmodells". In: *Holz Roh Werkst* 64.5 (Oct. 2006), pp. 393–402. ISSN: 0018-3768, 1436-736X. DOI: 10.1007/s00107-006-0102-3. URL: http://link.springer.com/10.1007/s00107-006-0102-3 (visited on 05/29/2020).

[121] E. Serrano and B. Enquist. *Mechwood II Glulam Tests.* Linnaeus University Växjö Sweden, 2014.

[122] A. R. Shahani and M. R. Amini Fasakhodi. "Finite Element Analysis of Dynamic Crack Propagation Using Remeshing Technique". In: *Materials & Design* 30.4 (Apr. 1, 2009), pp. 1032–1041. ISSN: 0261-3069. DOI: 10.1016/j.matdes.2008.06.049. URL: http://www.sciencedirect.com/science/article/pii/S0261306908003208 (visited on 07/28/2020).

[123] J. Simo and T. Hughes. *Computational Inelasticity*. Springer, New York, 1998.

[124] J. Simo, J. Kennedy, and S. Govindjee. "Non-Smooth Multisurface Plasticity and Viscoplasticity. Loading/Unloading Conditions and Numerical Algorithms". In: *International Journal for Numerical Methods in Engineering* 26.10 (1988), pp. 2161–2185.

[125] S.-P. Simonaho, J. Palviainen, Y. Tolonen, and R. Silvennoinen. "Determination of Wood Grain Direction from Laser Light Scattering Pattern". In: *Optics and Lasers in Engineering* 41.1 (Jan. 2004), pp. 95–103. ISSN: 01438166. DOI: 10.1016/S0143-8166(02)00144-6. URL: https://linkinghub.elsevier.com/retrieve/pii/S0143816602001446 (visited on 05/29/2020).

[126] A. Singh and S. Pal. "Multi-Phase Field Modeling for Various Fracture Mechanisms in Composites". In: *Engineering Fracture Mechanics* 241 (Jan. 2021), p. 107348. ISSN: 00137944. DOI: 10.1016/j.engfracmech.2020.107348. URL: https://linkinghub.elsevier.com/retrieve/pii/S0013794420309292 (visited on 01/13/2021).

[127] I. Smith, E. Landis, and M. Gong. *Fracture and Fatigue in Wood*. Chichester, West Sussex, England ; Hoboken, NJ: J. Wiley, 2003. 234 pp. ISBN: 978-0-471-48708-1.

[128] G. Söderlind and L. Wang. "Adaptive Time-Stepping and Computational Stability". In: *Journal of Computational and Applied Mathematics*. Special Issue: International Workshop on the Technological Aspects of Mathematics 185.2 (Jan. 15, 2006), pp. 225–243. ISSN: 0377-0427. DOI: 10.1016/j.cam.2005.03.008. URL: https://www.sciencedirect.com/science/article/pii/S0377042705001123 (visited on 09/30/2021).

[129] C. Steinke and M. Kaliske. "A Phase-Field Crack Model Based on Directional Stress Decomposition". In: *Comput. Mech.* (2018), pp. 1019–1046.

[130] M. Strobl and T. Seelig. "A Novel Treatment of Crack Boundary Conditions in Phase Field Models of Fracture". In: *PAMM* 15.1 (2015), pp. 155–156. ISSN: 1617-7061. DOI: 10.1002/pamm.201510068. URL: https://onlinelibrary.wiley.com/doi/abs/10.1002/pamm.201510068 (visited on 02/02/2021).

[131] E.-G. Talbi. *Metaheuristics: From Design to Implementation*. Vol. 74. John Wiley & Sons, 2009.

[132] S. Teichtmeister, D. Kienle, F. Aldakheel, and M.-A. Keip. "Phase Field Modeling of Fracture in Anisotropic Brittle Solids". In: *Int. J. Non Linear Mech.* 97 (2017), pp. 1–21. ISSN: 0020-7462. DOI: 10.1016/j.ijnonlinmec.2017.06.018. URL: http://www.sciencedirect.com/science/article/pii/S0020746217301944.

[133] S. W. Tsai and E. M. Wu. "A General Theory of Strength for Anisotropic Materials". In: *J. Compos. Mater.* 5.1 (1971), pp. 58–80.

[134] S. Vasic, I. Smith, and E. Landis. "Fracture Zone Characterization - Micro-mechanical Study". In: *Wood and Fiber Science* 34 (Jan. 2002), pp. 42–56.

[135] F. Verbosio, A. De Coninck, D. Kourounis, and O. Schenk. "Enhancing the Scalability of Selected Inversion Factorization Algorithms in Genomic Prediction". In: *Journal of Computational Science* 22 (Sept. 1, 2017), pp. 99–108. ISSN: 1877-7503. DOI: 10.1016/j.jocs.2017.08.013. URL: https://www.sciencedirect.com/science/article/pii/S1877750317301473 (visited on 08/13/2021).

[136] C. Vida, M. Lukacevic, J. Eberhardsteiner, and J. Füssl. "Modeling Approach to Estimate the Bending Strength and Failure Mechanisms of Glued Laminated Timber Beams". In: *Engineering Structures* 255 (Mar. 15, 2022), p. 113862. ISSN: 0141-0296. DOI: 10.1016/j.engstruct.2022.113862. URL: https://www.sciencedirect.com/science/article/pii/S0141029622000220 (visited on 03/26/2022).

[137]   WHB. *Wood Handbook: Wood as an Engineering Material*. Madison, USA: Forest Products Laboratory, 2010. URL: https://books.google.at/books?id=gwcUAAAAYAAJ&dq=+%22Wood+handbook:+Wood+as+an+engineering+material%22+Forest+Products+Laboratory+US&lr=&hl=de&source=gbs_navlinks_s.

[138]   D. Whitley. "An Overview of Evolutionary Algorithms: Practical Issues and Common Pitfalls". In: *Inf. and softw. technol.* 43.14 (2001), pp. 817–831.

[139]   A. Wilkins, B. W. Spencer, A. Jain, and B. Gencturk. "A Method for Smoothing Multiple Yield Functions". In: *International Journal for Numerical Methods in Engineering* 121.3 (2020), pp. 434–449.

[140]   M. L. Wilkins. "Calculation of Elastic-Plastic Flow". In: *Methods in Computational Physics, Volume 3: Fundamental Methods in Hydrodynamics*. Academic Press, New York, 1964.

[141]   C. Wu and K.-W. Chau. "Rainfall–Runoff Modeling Using Artificial Neural Network Coupled with Singular Spectrum Analysis". In: *J. of Hydrol.* 399.3 (2011), pp. 394–409. ISSN: 0022-1694. DOI: 10.1016/j.jhydrol.2011.01.017. URL: http://www.sciencedirect.com/science/article/pii/S0022169411000424.

[142]   J.-Y. Wu. "A Unified Phase-Field Theory for the Mechanics of Damage and Quasi-Brittle Failure". In: *J. Mech. Phys. Solids* 103 (June 2017), pp. 72–99. DOI: 10.1016/j.jmps.2017.03.015.

[143]   J.-Y. Wu. "Robust Numerical Implementation of Non-Standard Phase-Field Damage Models for Failure in Solids". In: *Comput. Methods Appl. Mech. Eng.* 340 (2018), pp. 767–797.

[144]   J.-Y. Wu, Y. Huang, and V. P. Nguyen. "On the BFGS Monolithic Algorithm for the Unified Phase Field Damage Theory". In: *Computer Methods in Applied Mechanics and Engineering* 360 (Mar. 1, 2020), p. 112704. ISSN: 0045-7825. DOI: 10.1016/j.cma.2019.112704. URL: https://www.sciencedirect.com/science/article/pii/S0045782519305924 (visited on 04/27/2022).

[145]   J.-Y. Wu and V. P. Nguyen. "A Length Scale Insensitive Phase-Field Damage Model for Brittle Fracture". In: *J. Mech. Phys. Solids* 119 (Oct. 2018), pp. 20–42. DOI: 10.1016/j.jmps.2018.06.006.

[146]   J.-Y. Wu, V. P. Nguyen, C. T. Nguyen, D. Sutula, S. Sinaie, and S. P. Bordas. "Phase-Field Modeling of Fracture". In: *Advances in Applied Mechanics*. Vol. 53. Elsevier, 2020, pp. 1–183. ISBN: 978-0-12-820989-9. DOI: 10.1016/bs.aams.2019.08.001. URL: https://linkinghub.elsevier.com/retrieve/pii/S0065215619300134 (visited on 04/27/2022).

[147]   J.-Y. Wu, V. P. Nguyen, H. Zhou, and Y. Huang. "A Variationally Consistent Phase-Field Anisotropic Damage Model for Fracture". In: *Comput. Methods Appl. Mech. Eng.* 358 (2020), p. 112629.

[148]   J.-Y. Wu, J.-F. Qiu, V. P. Nguyen, T. K. Mandal, and L.-J. Zhuang. "Computational Modeling of Localized Failure in Solids: XFEM vs PF-CZM". In: *Computer Methods in Applied Mechanics and Engineering* 345 (Mar. 2019), pp. 618–643. ISSN: 00457825. DOI: 10.1016/j.cma.2018.10.044. URL: https://linkinghub.elsevier.com/retrieve/pii/S0045782518305486 (visited on 04/27/2022).

[149]   H. Yang, C. Yang, and S. Sun. "Active-Set Reduced-Space Methods with Nonlinear Elimination for Two-Phase Flow Problems in Porous Media". In: *SIAM J. Sci. Comput.* 38.4 (2016), B593–B618.

[150]   Z.-J. Yang, B.-B. Li, and J.-Y. Wu. "X-Ray Computed Tomography Images Based Phase-Field Modeling of Mesoscopic Failure in Concrete". In: *Engineering Fracture Mechanics* 208 (Mar. 2019), pp. 151–170. DOI: 10.1016/j.engfracmech.2019.01.005.

[151] P. Zhang, X. Hu, T. Q. Bui, and W. Yao. "Phase Field Modeling of Fracture in Fiber Reinforced Composite Laminate". In: *International Journal of Mechanical Sciences* 161–162 (Oct. 1, 2019), p. 105008. ISSN: 0020-7403. DOI: 10.1016/j.ijmecsci.2019.07.007. URL: https://www.sciencedirect.com/science/article/pii/S0020740318341729 (visited on 04/25/2022).

[152] P. Zhang, X. Hu, S. Yang, and W. Yao. "Modelling Progressive Failure in Multi-Phase Materials Using a Phase Field Method". In: *Engineering Fracture Mechanics* 209 (Mar. 15, 2019), pp. 105–124. ISSN: 0013-7944. DOI: 10.1016/j.engfracmech.2019.01.021. URL: https://www.sciencedirect.com/science/article/pii/S0013794418311184 (visited on 05/04/2022).

[153] P. Zhang, W. Yao, X. Hu, and T. Q. Bui. "3D Micromechanical Progressive Failure Simulation for Fiber-Reinforced Composites". In: *Composite Structures* 249 (Oct. 1, 2020), p. 112534. ISSN: 0263-8223. DOI: 10.1016/j.compstruct.2020.112534. URL: http://www.sciencedirect.com/science/article/pii/S0263822319348421 (visited on 07/01/2020).

[154] S. Zhang and K.-W. Chau. "Dimension Reduction Using Semi-Supervised Locally Linear Embedding for Plant Leaf Classification". In: *Emerging Intelligent Computing Technology and Applications*. Ed. by D.-S. Huang, K.-H. Jo, H.-H. Lee, H.-J. Kang, and V. Bevilacqua. Berlin, Heidelberg: Springer Berlin Heidelberg, 2009, pp. 948–955. ISBN: 978-3-642-04070-2.

[155] S. Zhang, D.-U. Kim, W. Jiang, and M. R. Tonk. "A Phase Field Model of Crack Propagation in Anisotropic Brittle Materials with Preferred Fracture Planes". In: *Computational Materials Science* 193 (June 2021), p. 110400. ISSN: 09270256. DOI: 10.1016/j.commatsci.2021.110400. URL: https://linkinghub.elsevier.com/retrieve/pii/S0927025621001257 (visited on 03/16/2021).

[156] J. Zhou and J. Shen. "Ellipse Detection and Phase Demodulation for Wood Grain Orientation Measurement Based on the Tracheid Effect". In: *Opt. and Lasers in Eng.* 39.1 (2003), pp. 73–89. ISSN: 0143-8166. DOI: 10.1016/S0143-8166(02)00041-6. URL: http://www.sciencedirect.com/science/article/pii/S0143816602000416.

Publications and Conference Contributions

Books

Ch. Schranz, R. Suda, S. Pech:
LaTeX, Excel, Word – Werkzeuge für den ingenieurwissenschaftlichen Hochschul-Einsatz
TU Verlag, Wien, 2018, ISBN: 978-3-903024-66-3; 408 S.

Ch. Schranz, R. Suda, S. Pech:
LaTeX, Excel, Word – Werkzeuge für den ingenieurwissenschaftlichen Hochschul-Einsatz (2., korrigierte und erweiterte Auflage)
TU Verlag, Wien, 2019, ISBN: 978-3-903024-90-8; 432 S.

Ch. Schranz, R. Suda, S. Pech:
LaTeX, Excel, Word – Werkzeuge für den ingenieurwissenschaftlichen Hochschul-Einsatz (3., korrigierte und erweiterte Auflage)
TU Verlag, Wien, 2021, ISBN: 978-3-903311-22-0; 432 S.

Publications

G. Datseris, J. Isensee, S. Pech, T. Gal:
DrWatson: the Perfect Sidekick for your Scientific Inquiries
The Journal of Open Source Software, 5(54) (2020), 2673; 6 S.

S. Pech, G. Kandler, M. Lukacevic, J. Füssl:
Metamodel Assisted Optimization of Glued Laminated Timber Beams by Using Metaheuristic Algorithms
Engineering Applications of Artificial Intelligence, 79 (2019), S. 129–141.

S. Pech, M. Lukacevic, J. Füssl:
A Robust Multisurface Return-Mapping Algorithm and Its Implementation in Abaqus
Finite Elements in Analysis and Design, 190 (2021), 103531; S. 1–9.

Conference Proceedings

M. Autengruber, M. Lukacevic, C. Vida, S. Pech, J. Füssl:
Computergestützte Modellierung im Holzbau - Herausforderungen und Möglichkeiten
Vortrag: 25. Dresdner Baustatik-Seminar "Realität - Modellierung - Tragwerksplanung", Dresden (Deutschland); 15.10.2021; in: *25. Dresdner Baustatik-Seminar: Realität – Modellierung – Tragwerksplanung*, TU-Dresden (Hrg.); (2021), ISSN: 1615-9705; S. 131–160.

M. Lukacevic, J. Füssl, S. Pech, C. Vida, J. Eberhardsteiner:
Computational Mechanics Concepts for Wood-Based Products and Timber Structural Elements

Vortrag: World Conference on Timber Engineering (WCTE2021), Santiago, Chile; 09.08.2021 – 12.08.2021; in: *Proceedings of WCTE 2021 – World Conference on Timber Engineering*, Santiago, Chile (2021).

S. Pech, G. Kandler, J. Füssl:
Metamodel Assisted Optimization of GLT Systems by Reordering Laminations Using Metaheuristic Algorithms
in: *Proceedings of the 6th European Conference on Computational Mechanics (ECCM6-ECFD7)*, International Center for Numerical Methods in Engineering (CIMNE), 2018.

S. Pech, G. Kandler, M. Lukacevic, J. Füssl:
Metamodel Assisted Optimization of Glued Laminated Timber Beams by Using Metaheuristic Algorithms
in: *Book of Abstracts of the 90th Annual Meeting of the International Association of Applied Mathematics and Mechanics (GAMM 2019)*, J. Eberhardsteiner, J. Schöberl (Hrg.); TU Verlag, 2019, ISBN: 978-3-903024-84-7, S. 438.

S. Pech, M. Lukacevic, J. Füssl:
Phase Field Method-Based Modeling of Fracture in Wood
in: *Programme & Proceedings of the China-Austria Forum for Postgraduates of Civil Engineering*, J. Zhang, B. Pichler (Hrg.); Vienna University of Technology, 2019, S. 98–101.

S. Pech, M. Lukacevic, J. Füssl:
Phase Field Method-Based Modeling of Fracture in Wood
in: *Book of Abstracts of the International Conference on Computational Methods in Wood Mechanics – from Material Properties to Timber Structures (CompWood 2019)*, Linnaeus University, 2019, ISBN: 978-91-88898-64-7, S. 17.

Conference Presentations

S. Pech:
Metamodel Assisted Optimization of GLT Systems by Reordering Laminations Using Metaheuristic Algorithms
Vortrag: 6th European Conference on Computational Fluid Dynamics (ECCM – ECFD 2018), Glasgow, United Kingdom; 11.06.2018–15.06.2018.

S. Pech:
Metamodel Assisted Optimization of Glued Laminated Timber Beams by Using Metaheuristic Algorithms
Vortrag: 90th Annual Meeting of the International Association of Applied Mathematics and Mechanics (GAMM 2019), Vienna, Austria; 18.02.2019–22.02.2019.

S. Pech:
Phase Field Method-Based Modeling of Fracture in Wood
Vortrag: China-Austria Forum for Postgraduates of Civil Engineering, Vienna, Austria; 07.10.2019–08.10.2019.

S. Pech:

Phase Field Method-Based Modeling of Fracture in Wood

Vortrag: XV. International Conference on Computational Plasticity – Fundamentals and Applications (COMPLAS 2019), Barcelona, Spain; 03.09.2019–05.09.2019.

S. Pech:

Phase Field Method-Based Modeling of Fracture in Wood

Vortrag: International Conference on Computational Methods in Wood Mechanics – From Material Properties to Timber Structures (CompWood 2019), Växjo, Sweden; 17.06.2019–19.06.2019.

S. Pech:

Phase Field Method-Based Modeling of Fracture in Wood

Vortrag: 14th World Congress in Computational Mechanics (WCCM) & ECCOMAS Congress 2020, virtual Congress; 11.01.2021–15.01.2021.

S. Pech:

Phase Field Method-Based Modeling of Fracture in Wood

Vortrag: Engineering Mechanics Institute Conference and Probabilistic Mechanics & Reliability Conference (virtual Event), Reston, VA, USA; 25.05.2021–28.05.2021.

S. Pech, M. Lukacevic, J. Füssl:

Phase field method-based modeling of fracture in wood

Vortrag: 16. International Conference on Computational Plasticity, Fundamentals and Applications, Barcelona, Spain; 07.09.2021–09.09.2021.

Master's Thesis (own and supervised)

S. Pech:

Metamodel Assisted Optimisation of Glued Laminated Timber Systems by Reordering Laminations Using Metaheuristic Algorithms

Betreuer/in(nen): G. Kandler, J. Füssl, J. Eberhardsteiner; Institut für Mechanik der Werkstoffe und Strukturen, 2017; Abschlussprüfung: 20.10.2017.

C. Vida:

Computergestützter Modellierungsansatz zur Bestimmung der Biegefestigkeit von Brettschichtholzträgern unter Berücksichtigung von Astgruppen und quasi-sprödem Materialversagen

Betreuer/in(nen): M. Lukacevic, S. Pech, J. Füssl; Institut für Mechanik der Werkstoffe un Strukturen, 2020; Abschlussprüfung: 25.09.2020.

Curriculum Vitae

Personal Data

Name:	Sebastian Pech
Date of Birth:	■■■■■■
Place of Birth:	Vienna, Austria
Nationality:	Austria
Current Address:	■■■■■■■■■■■■

Education

since 2017:	Doctoral program in Civil Engineering at TU Wien, Austria
2015–2017:	Master program in Civil Engineering at TU Wien, Austria
2011–2016:	Bachelor program in Civil Engineering and Management Infrastructure at TU Wien, Austria
2005–2010:	Höhere technische Bundeslehranstalt, HTL3 Rennweg, Vienna, Austria, Upper Secondary School, Information Technology, Focus on Internet and Media Technology

Work experience

since 2017:	University assistant at the Institute for Mechanics of Materials and Structures, TU Wien, Austria
2011–2017:	Technical employee at Dr. PECH Ziviltechniker GmbH, Vienna, Austria
2014–2017:	Student assistant / Tutor at the Civil Engineering Computer Laboratory, TU Wien, Austria